Ion-pair Imaging: Apparatus design and its application to a complete characterization of photodissociation processes

Von der Fakultät für Lebenswissenschaften

der Technischen Universität Carolo-Wilhelmina

zu Braunschweig

zur Erlangung des Grades

eines Doktors der Naturwissenschaften

(Dr. rer. nat.)

genehmigte

Dissertation

von Mikhail Sergeevic Poretskiy
aus Sankt Petersburg / Russland

1. Referent: Professor Dr. Karl-Heinz Gericke
2. Referent: Privatdozent Dr. Christof Maul
eingereicht am: 05.11.2014
mündliche Prüfung (Disputation) am: 16.12.2014

Druckjahr 2015

Vorveröffentlichungen der Dissertation

Teilergebnisse aus dieser Arbeit wurden mit Genehmigung der Fakultät für Lebenswissenschaften, vertreten durch den Mentor der Arbeit, in folgenden Beiträgen vorab veröffentlicht:

Publikationen

Poretskiy, M., Chichinin, A.I., Maul, C. & Gericke, K.-H. Simultaneous imaging of both product ions: Exploring gateway states for HCl as a benchmark molecule. PCCP 16: 19741-19746 (2014).

Tagungsbeiträge

[1] Poretskiy, M., Chichinin, A.I., Maul, C. & Gericke, K.-H.: Probabilities for 2-and 3-photon absorption, ion pair channel (H^++Cl^-) in REMPI of HCl, and emission from metal surface of e^-, H^-, and HCl^- ions under the bombardment by H^+, Cl^+, and HCl^+ ions. (Vortrag) 29. STEREODYNAMICS 2014, St. Petersburg (2014).

[2] Poretskiy, M., Chichinin, A.I., Maul, C. & Gericke, K.-H.: Two- and three-photon absorption cross section measurement in case of HCl photoionization and photodissociation by means of 3D-imaging method. (Poster) 78. STEREODYNAMICS 2014, St. Petersburg (2014).

[3] Poretskiy, M., Chichinin, A.I., Maul, C. & Gericke, K.-H.: Surface scattering of H^- and HCl^- ions, resulting from the recharge of H^+ and HCl^+. (Poster) 78. STEREODYNAMICS 2014, St. Petersburg (2014).

[4] Maul, C., Poretskiy, M., Chichinin, A. & Gericke, K.-H.: H^+ + $Cl^−$: Photoion pair production in HCl studied by bipolar three-dimensional (3D) photoion pair imaging. (Poster) 184. DPG-Frühjahrstagung, Berlin (2014).

[5] Poretskiy, M., Chichinin, A., Maul, C. & Gericke, K.-H.: Negative ion imaging resulting from HCl photodissociation. (Poster). DPG-Frühjahrstagung, Hannover (2013).

[6] Poretskiy, M., Veckenstedt, M., Maul, C. & Gericke, K.-H.: HBr photodissociation analysis as the calibration of two-color 3D velocity map imaging setup. (Poster) 152. “MOLECULAR PHOTONICS” dedicated to academician A.N. Terenin, Repino (2012).

[7] Poretskiy, M., Veckenstedt, M., Maul, C. & Gericke, K.-H.: Experimental calibration of a 3D velocity map imaging setup using HBr photodissociation. (Poster) 24. Summer School of metrology 2012, Burg Warberg (2012).

[8] Veckenstedt, M., Poretskiy, M., Maul, C. & Gericke, K.-H.: 3D velocity mapping of the Hydrogen atom formation from the 193 nm photodissociation of borazine via (2+1)-REMPI. (Poster) 139. DPG-Frühjahrstagung, Stuttgart (2012).

[9] Poretskiy, M., Veckenstedt, M., Maul, C. & Gericke, K.-H.: Experimental calibration of a 3D Velocity map imaging setup using HBr photodissociation. (Poster) 139. DPG-Frühjahrstagung, Stuttgart (2012).

[10] Veckenstedt M., Rakhymzhan, A., Poretskiy, M., Kauczok, S., Chichinin A.I., Goedecke, N., Maul C. & Gericke, K.-H.: 3D Velocity Map Imaging: Apparatus Details and Application. (Poster). ICONIC Training School, Freiburg (2010.)

Content

1 Introduction

1.1 Preface

As soon as man began to reflect upon the nature of the world around, he paid attention to the structure of the material objects. The idea that any material object in nature consists of chemically indivisible particles was born in the Ancient Greece in the 5th century BC as natural philosophy. Using the five senses as the first experimental set-up, Leucippus and his follower Democritus proposed the earliest views on the shapes and connectivity of atoms. Impressed by their teaching Epicurus reasoned that the solidness of the material corresponded to the shape of the involved atoms. Growing and evaluating, these ideas have found the reflection in the works of Newton and Boyle. Newton suggested, that particles attract one another by some force, which "in immediate contact is extremely strong, at small distances performs the chemical operations, and reaches not far from particle with any sensible effect." In his turn Robert Boyle presented his famous treatise "The skeptical Chymist", in that he said that the matter is composed of clusters of particles ("corpuscles") and that chemical change results from rearrangement of the clusters. In the 18th century Boyle's conception has been developed by Étienne François Geoffroy (1718, the table of "affinities") and by William Higgins (1789, combination of "ultimate" particles). In 1811 Amedeo Avogadro in the famous paper "Essay on Determining the Relative Masses of the Elementary Molecules of Bodies" states:

> "The smallest particles of gases are not necessarily simple atoms, but are made up of a certain number of these atoms united by attraction to form a single molecule."

The basis of human knowledge grew and the understanding of the molecule's nature opened new facts. For example the concept of the electron-pair bond (1916, Lewis), in which two atoms may share one or six electrons, thus forming the single electron bond, a single bond, a double bond, or a triple bond. Using quantum mechanics, Linus Pauling calculated properties and structure of molecules (angles between bonds) and published the results in his ground-breaking article "The Nature of the Chemical bonds" [1]. Basing on this work Pauling developed hybridization theory, for which he was honored by the Nobel Prize in Chemistry in 1954.

The point of view on the question, how the atoms form a molecule, can be changed. One can ask, how a molecule splits in a set of atoms or other molecular fragments. This setting of the problem opens a new area in the molecular science, the area of fragmentation or dissociation of the molecule. In 1898, Ludwig Boltzmann, in his *Lectures on Gas Theory*, used the theory of valence to explain the phenomenon of gas phase molecular dissociation. Boltzmann proposed as well an explanation of existence of the molecules composed of two atoms. According to this explanation, the force acting between the two atoms attracts one to another. Boltzmann formulated his statements on the basis of the experimental fact that molecular iodine vapor dissociates into atom at higher temperatures.

High temperature is one of the factors, which can start the dissociation of the molecules. Another factor, surrounding the people most of the time and influencing the atmosphere of our planet, is the light of the Sun. This type of dissociation, occurring under the action of the photons, is called photodissociation. The study in this area is of a big importance in the investigations of the outer space and of the photoprocesses in the atmosphere of Earth and other planets, can help in solving the problems of removing of anthropogenic pollutions from the atmosphere and in the problems of conversion and of storage of the light energy. However, in case of each application the question is only about the primary processes of photodissociation. In other words the intramolecular processes leading to the photodissociation occur after absorption of light by a molecule, which does not collide or interact with the other molecules or any obstacle. The experimental techniques, ideally fulfilling these purposes, for many years were a dream for the experimentalists.

The first studies of photodissociation took place in the first half of 20th century and were concentrated on the identification of the primary products. In 1960s due to the appearance of the first lasers, which gave the possibility to develop more sophisticated spectroscopic techniques, the number of detectable substances via spectroscopy has increased enormously and the characteristic electronic states of many molecules were assigned. This opened the way to the detailed description of the dynamics of photodissociation processes, where detailed knowledge of the states of reactants is needed.

The earliest photofragment spectrometers measured either the recoil velocity distribution [2,3] or the internal energy of the fragments [4,5]. The Doppler technique in its turn allowed to obtain the correlation between these properties [6,7,8]. The ion imaging technique invented by David Chandler and coworkers [9,10,11] gave the opportunity to simultaneously determine the angular and speed distribution of photofragments. In this method photofragments are photoionized and then projected onto a two-dimensional detector array. By inversion a complete velocity distribution of the photofragments can be derived. The next step in the direction of ion imaging methods improvement was made by Eppink and Parker [12]. They developed the Velocity Map Imaging, which significantly improved the energy resolution of the imaging technique.

Those velocity map imaging methods gave the two-dimensional projections of three-dimensional product distribution. To analyze 2D “velocity map” images, the Abel algorithm of the forward convolution analysis have been used [13]. This algorithm introduces some limitations in the powerful technique like the demand of cylindrical symmetry of the initial 3D distribution or the demand of electric vector of dissociative radiation orientation perpendicular to the spectrometer axis. It can be computationally expensive and does not lead to unique solution.

The 3D Imaging technique used in the current study has several advantages in comparison to the 2D variant. The most important aspect consists in the straightforward way of analysis. No integration method like the Abel inversion algorithm is needed. It is more universal: allows to work with any polarization of the radiation and does not assume any symmetry of initial fragment distribution. Technically it includes the simultaneous measurement of all the three coordinates of a particle which are defined by the spatial position in the two-dimensional plane of the position sensitive detector and by the time of arrival at the detector (third dimension) of the ionized product of photodissociation. The transverse components (v_x, v_y) of the initial velocity of a negative ion are obtained on the basis of impact coordinates on the detector surface, while the longitudinal component (v_z) is calculated using time of arrival. Direct determination of the 3D velocity distribution of a product in a specific quantum level provides complete information about the photodissociation process. Different features of used 3D imaging set-up and its many applications were in detail described by my predecessor in their dissertations [14,15,16].

1.2 The contribution of this work

Until now 3D Ion Imaging techniques has been used only for the detection of positive ions, and the analysis of the photodissociation was limited to this information. However, in the majority of cases the product of one type are produced at the same wavelength via several channels of photodissociation. The consequent processes of resonance enhanced multiphoton ionization (REMPI) transform them in the positive ions. As a result the ions produced in the different ways are simultaneously detected. And neither time-of-flight (TOF) measurement nor spectroscopic knowledge allows to discriminate between them. 3D Velocity Map Imaging gives the possibility to see the existing channels in the speed distribution. But even this powerful method does not open a way to study one channel exclusively.

In contrast to positive, the negative ions result only from the ion-pair channel of photodissociation, and, thus, the detection of negative ions gives the opportunity to perform a selective analysis of the photodissociation channel with ion-pair origin. The results of such detailed analysis can be used in the study of a whole set of photodissociation channels. The first application of 2D imaging to detect negative ions, produced via the photodissociation of the molecules, has been done by Suits et al [17,18]. To realize the possibility of negative ions 3D Imaging detection the existing experimental set-up has been enhanced by the installation of a second TOF mass-spectrometer and a second 3D detector unit. That allows to do the complete 3D measurement of momentum vector of a negative ion simultaneous with the analogous measurement for positive ion resulting from the same ion-pair channel of photodissociation.

Before discussing the ion-pair channels of photodissociation, an overview of the capabilities of the spectrometer is given (chapter 3) by means of an example of the one-photon photodissociation of the borazine molecule. This investigation is abundant by the methods involved in it and uses the whole power of the 3D imaging method. It needs the use of two different lasers: an excimer laser to initiate the dissociation and a dye laser for detecting the products. This two-color experiment includes the calibration HBr photodissociation analysis, leading to spatial overlap of the beams of dissociative and detection laser. The overlap allows to do the measurement of momentum vector by means of the 3D Velocity Map Imaging configuration of the set-up. The obtained speed distribution and the speed-dependent parameter of anisotropy allow to discriminate between the two channels of borazine fragmentation: predissociation and direct dissociation. The phase space theory has been applied to evaluate the predissociation process. The results will demonstrate that the 3D imaging method is significantly more sensitive than former techniques [19].

The second spectrometer introduced in the set-up geometrically is the mirror reflection of the first one. Both spectrometers can work separately, providing the information either about positive or about negative ions, or in combination. In the last case it is logically to present the set-up not like a construction of two spectrometers, but like one indivisible structure called “double-arm spectrometer”. The chapter 4 of the present dissertation reports the first application of this novel set-up to the study of HCl multiphoton photodissociation and REMPI in the spectral range from 230 to 245 nm. This chapter shows the obtained 3D velocity vector distribution and the speed distribution of simultaneously detected negative and positive ions. The measured speed distribution of the ions gives the possibility to draw the conclusion that several channels of HCl photodissociation take place, and among them there is only one with the ion-pair nature. It also demonstrates that each channel of photodissociation occurs after the absorption of three photons. This chapter presents as well the mechanism of the HCl photodissociation or photoionization. All the channels of both processes start from a resonant two-photon absorption to an intermediate state IS_1. A third photon excites a higher state IS_2, which can be the ground state of HCl molecular ion or another excited state of the HCl molecule, from which the system directly dissociates or undergoes a nonadiabatic transition to a lower state and dissociates from it.

The cooperative configuration of the experimental set-up (“double-arm spectrometer”) is similar to the apparatus used in photoelectron photoion coincident spectroscopy (PEPICO) studies of photoionization processes [20,21,22] and opens the perspectives to perform the coincidence studies of photodissociation process as well. However, in case of PEPICO in order to do the correct measurements, the rate of photoelectron-photoion detection has to be very low. In other words one has to produce less than one pair per laser pulse. In case of full photodissociation studies to be able to observe the ion emerging from the weakest channel of fragmentation one need to significantly increase the power of the laser. In consequence the amount of produced particles per laser pulse will be so large that the parasitic processes in the double-arm spectrometer interfere with the ions from the fragmentation channel under question.

How to deal with these processes is discussed in the Chapter 5, where the detailed description of the double-arm spectrometer system is given. All these processes influencing on the spectrometer as well as the ways to minimize their influence are discussed in the Chapter 5. As a test task the photodissociation of HCl molecule is used. The first process is the production of the photoelectrons emerging from photoionization of HCl molecules and product atoms. The produced electrons almost immediately reach the detector of negative ions, saturate it and make impossible the following detection of negative ion. The installation of permanent magnets solves this problem. The next parasitic process consists in the secondary electrons production after the impacts of the positive ions onto parts of the double-arm spectrometer. These electrons are detected by the negative ions detector. Moreover, their time of arrival can occasionally coincide with the time of arrival of the negative ions under study. As a result the electrons can contribute to the measured distribution as false data. The process of the ions impacts leads simultaneously to the neutralization of the positive ions. Thus, the number of detected ions in comparison to the number of produced ions is smaller. To solve these problems a special configuration of the double-arm spectrometer, called “trap” configuration, has been developed.

This configuration allows to perform a test of the system and characterizes the parasitic processes quantitatively.

As it has been mentioned above the absorption of the laser radiation by HCl molecule in the spectral region from 230 to 245 nm results in [2+1] resonance enhanced multi-photon ionization (REMPI) or in three-photon photodissociation via several channels. All the channels include a two-photon absorption and a one-photon absorption step. In chapter 6 the quantitative characterization of the efficiency of the process of two-photon absorption as well as the processes of photoionization and photodissociation is performed. For this purpose the concepts of two-photon and three-photon absorption cross-sections are introduced. A theoretical study of three-photon processes, describing the photoionization and photodissociation, has been performed to obtain the exact expression for the proportionality factor between the number of products and the power (cube or square) of the laser pulse energy. This chapter discusses the experimental dependences of product numbers on the laser radiation power, simultaneously measured for positive and negative ions by means of the double-arm spectrometer in case of the excited intermediate states $V^1\Sigma^+(v=8,9,10,11,12,13,14,15, J=0)$ and $E^1\Sigma^+(v=0,1, J=0)$. The precise value of the number of products is guarantied by the test, done in the “trap” configuration. The values of two-photon and three-photon absorption cross-section exhibit large difference of about one order of magnitude depending on the nature of the intermediate excited state.

References

---

[1] L. Pauling, J. Am. Chem. Soc. **53**, 1367 (1931).

[2] G. E. Busch, R. T. Mahoney, R. I. Morse, and K. R. Wilson, I. Chern. Phys. **51**, 449 (1969).

[3] M. Dzvonik, S. Yang, and R. Berschn, J. Chern. Phys. **61**, 4408 (1974).

[4] W. M. Jackson, J. Chern. Phys. **59**, 960 (1973).

[5] A. P. Baronavski and J. R. McDonald, Chern. Phys. Lett. **45**,172 (1977).

[6] J. L. Kinsey, J. Chern. Phys. **66**, 2560 (1977).

[7] R. Schmiedl, H. Dugan. W. Meier, and K. H. Welge, Z. Phys. A **304**. 137 (1982).

[8] I. Nadler, D. Mahgerefteh, H. Reisler, and C. Wittig, J. Chern. Phys. **82**. 3385 (1985).

[9] D.W. Chandler and P. L. Houston, J. Chem. Phys. **87**, 1445 (1987).

[10] J. W. Thoman, Jr., D. W. Chandler, D. H. Parker, and M. H. M. Janssen, Laser. Chem. **9**, 27 (1988).

[11] D. W. Chandler, J. W. Thoman, Jr., D. H. Parker, and M. H. M. Janssen, Chem. Phys. Lett. **156**, 151 (1989).

[12] A. T. J. Eppink and D. H. Parker, Rev. Sci. Instr. **68**, 3477 (1997).

[13] A. J. R. Heck and D. W. Chandler, Ann. Rev. Phys. Chem. **46**, 335 (1995).

[14] T. Einfeld, Dissertation TU-Braunschweig (2004).

[15] N. Goedecke, Dissertation TU-Braunschweig (2008).

[16] S. Kauczok, Dissertation TU-Braunschweig (2005).

[17] X. Liu, R. L. Gross, A. G. Suits, Science **294**, 2527 (2001).

[18] M. Ahmed, D. S. Peterka, P. Regan, X. H. Liu, A. G. Suits, Chem. Phys. Lett. **339**, 203 (2001).

[19] D. Huang, A. Hidalgo, V. I. Makarov, G. Morell, B. R. Weiner, Chem. Phys. Lett. **509**, 108 (2011).

---

[20] J. H. D. Eland, M. Takahashi, and Y. Hikosaka, Faraday Discuss., **115**, 119 (1999).

[21] M. Takahashi, J. P. Cave, and J. H. D. Eland, Rev. Sci. Instr. **71**, 1337 (2000).

[22] A. Matsuda, M. Fushitani, A. Hishikawa, Journal of Electron Spectroscopy and Related Phenomena **169**, 97 (2009).

2 Theory and methods

2.1 Photodissociation as a process of two-body fragmentation

The concept of photodissociation process is very broad. It can occur according to many different mechanisms. Here only the basic aspects describing the two-body fragmentation taking place in the current study are discussed. The process of photodissociation of a molecule AB includes two steps. In the first step the molecule absorbs one [1] or several photons and makes a transition from the ground to an energetic higher electronic state. The dissociation of the excited complex may occur in two cases: (a) the upper state is not bound with respect to the nuclear motion or (b) after the transition the molecule reaches the vibrational continuum of the upper state. The scheme of the photodissociation is illustrated in Fig. 2.1.1:

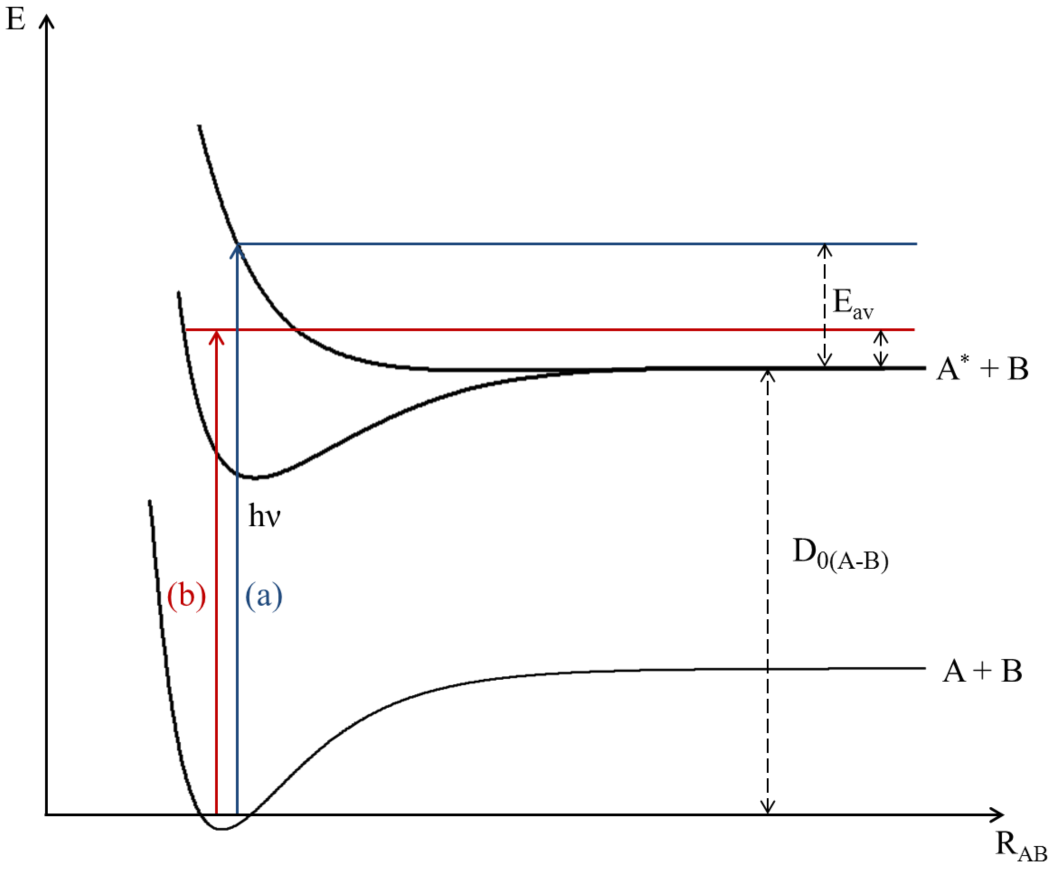

FIG. 2.1.1: Schematic illustration of photodissociation of a molecule AB after a single photon absorption.

$$AB + n * h\nu \rightarrow AB^* \rightarrow A + B \tag{2.1.2}$$

In the process of photodissociation the absorbed light energy is partially consumed to break the AB bond. The remaining energy, called the available energy, is distributed among the degrees of freedom of the products A and B, including translational degrees of freedom (kinetic energy of the fragments) and internal degrees of freedom (vibrational, rotational and electronic energy of fragments):

$$E_{av} = E_{kin,A} + E_{int,A} + E_{kin,B} + E_{int,B} \tag{2.1.3}$$

From the other side the available energy can be calculated as the energy of the light plus the internal energy of the parent molecule reduced by the dissociation energy $D_{0(A\text{-}B)}$:

$$E_{av} = h\upsilon + E_{int,AB} - D_{0(A-B)} \tag{2.1.4}$$

As a result the law of energy conservation results in:

$$h\upsilon + E_{int,AB} - D_{0(A-B)} = E_{kin,A} + E_{int,A} + E_{kin,B} + E_{int,B} \tag{2.1.5}$$

From this equation it is easy to see that the analysis can be simplified, if the internal energy of the parent molecule is negligible in the experiment. Such conditions can be achieved if one uses the techniques of molecular beam (this technique is discussed below in the Chapter 2.2). Finally:

$$h\upsilon - D_{0(A-B)} = E_{kin,A} + E_{int,A} + E_{kin,B} + E_{int,B} \tag{2.1.6}$$

In the center of mass system of the parent molecule AB ($\vec{p}_{AB} = 0$) the conservation of linear momentum results in:

$$\vec{p}_A + \vec{p}_B = \vec{p}_{AB} = 0 \;\Rightarrow\; \vec{p}_A = -\vec{p}_B \;\Rightarrow\; E_{kin,B} = \frac{m_A}{m_B} E_{kin,A} \tag{2.1.7}$$

where p is the linear momentum and m the mass of the atom fragment or molecule. From equation (2.1.6) and (2.1.7) it is easy to conclude that for the complete characterization of the photodissociation the quantum state of a product as well as its three-dimensional momentum vector needs to be determined simultaneously. In order to determine the momentum vector of a product generated in a photodissociation process, this process must be initiated at a well-defined time and the product must not undergo any collision prior to its detection. In order to meet both demands simultaneously, the process is usually initiated be the action of a pulsed laser in the low pressure environment of a vacuum chamber.

This subchapter shows the demands on experiment, describing photodissociation, and as a result defines the content of further discussion in this chapter. First of all one needs to obtain the conditions of the molecular beam (chapter 2.2), where the internal energy of the parent molecule is negligible. Then the nature of electronic states involved in the process of photodissociation has to be understood as well as the way to excite the molecule in higher electronic state (subchapter 2.3) has to be found. Then the principles of momentum components measurement have to be described (chapter 2.4).

2.2 Cold molecules in collision free environment: Molecular beams

As mentioned above, in order to simplify the analysis of photodissociation dynamics special experimental conditions are necessary (transition from equation 2.1.5 to 2.1.6). Under these conditions the internal energy of the parent molecule has to be negligible, or in other words the parent molecules have to be isolated from each other and distributed over a small number of internal states.

These conditions can be obtained due to the expansion of a gas through a nozzle into the vacuum leading to the formation of a molecular beam. The effusive beam technique has been used for over half century in many historical beam experiments to establish the basic principles of Modern Physics. Such accomplishments have been celebrated by the Nobel prizes in Physics. Among these achievements are the verification of the Maxwell-Boltzmann velocity distribution of gaseous atoms (O. Stern, 1911), the discovery of the space quantization (O. Stern and W. Gerlach, 1922) and its important applications in nuclear magnetic resonance (I. Rabi, 1938). The combination of an ammonia beam (NH_3) and an electric field, instead of a magnetic field, provided space quantization and state selection which have led to the invention of the maser and hence the laser (Ch. Townes and also N. Basov and A. Prokhorov, 1950).

The effusive beams are formed in the cases of those nozzle configurations, where the diameter of the nozzle orifice is smaller than the mean free path of the molecules. In other words only one molecule at a time will pass through the nozzle orifice. The energy and the momentum of such molecules are conserved, and the temperature of the gas after the nozzle is not altered.

In the opposite case of a nozzle configuration, where the orifice diameter is larger than the mean free path length, many molecular collisions occur in the nozzle. As a consequence, the molecules form a supersonic jet (local Mach number is greater than 1) propagating along the direction of the aperture of the nozzle. This beam is more collimated ($cos^2(\theta)$) than the effusive one ($cos(\theta)$). Because of the very fast gas flow though the nozzle the energy release to the chamber wall is negligible and the flow can be taken as adiabatic. Due to this adiabatic expansion of the gas from the gas reservoir at high pressure p_0 and temperature T_0 into a vacuum chamber (p, T) the cooling is reached (reference, Hayes). The conservation of the energy can be written as:

$$U_0 + p_0V_0 + \frac{1}{2}mu_0^2 = U + pV + \frac{1}{2}mu^2 \qquad (2.2.1)$$

where U_0 and U are the internal energy in gas reservoir and vacuum chamber, u_0 and u are the collective speeds of molecules in one direction in gas reservoir and vacuum chamber. Since the molecules in the gas reservoir are in an equilibrium, the collective motion in one direction and, thus, the flow energy $\frac{1}{2}mu_0^2$ is zero. Because of the low pressure in the vacuum chamber pV is negligible. The equation (1) is modified to:

$$U_0 + p_0V_0 = U + \frac{1}{2}mu^2 \qquad (2.2.2)$$

One can see that the large flow energies in the vacuum chamber are accompanied by low internal energies and only a few internal degrees of freedom are populated.

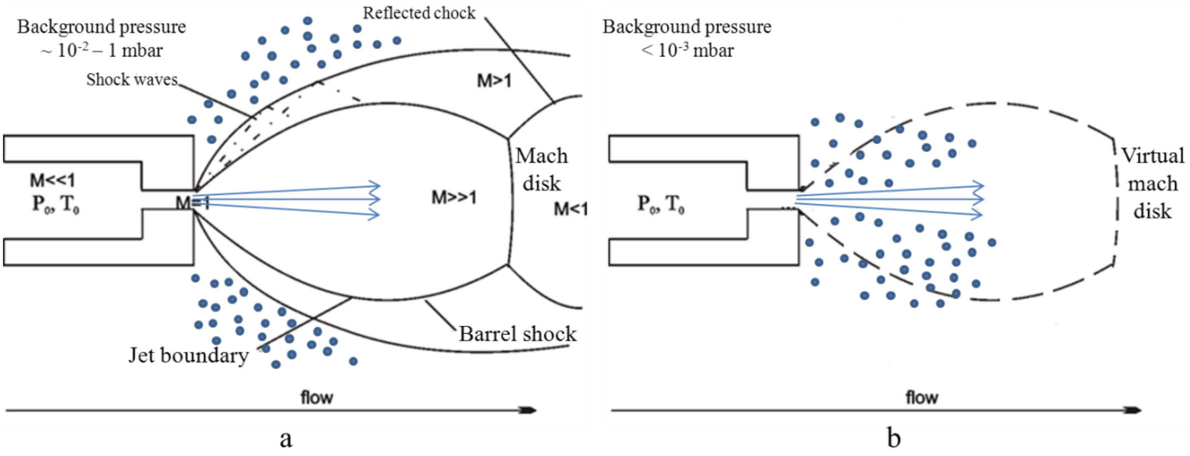

FIG. 2.2.1: Molecular beam structure for a **(a)** Campargue and **(b)** Fenn sources.

Depending on the background pressure in the vacuum chamber, two general types of molecular beam sources can be distinguished. For the moderate pressure in the range 10^{-2} – 1 mbar, the supersonic beam hits the background gas with a higher speed than the background gas can react to the perturbation travelling at the local speed of sound. As a result the developing jet is encased in a shock wave structure (Fig. 2.2.1a). This shock-wave extends from the nozzle orifice to the Mach disk. At typical operating pressures, this shock wave is thick enough and dense enough to prevent penetration of the core of the jet by warm background gas. Therefore, the volume inside the shock wave is called “zone of silence”. This type of beam source is termed a Campargue source.

In contrast to the Campargue-type source of molecular beam is the Fenn-type system [2,3] (Fig. 2.2.1b). It operates in the case of the background pressure in the vacuum chamber 2-3 orders of magnitude lower than in the Campargue-type expansion. In this case the mean free path becomes too large for the shock-wave structure to be significant. In the current study the beam sources are of Fenn-type.

An additional cooling of the beam can be reached in two cases. Firstly, the molecules under study can be diluted in a buffer gas like helium or argon to obtain the mixture with the small percentage of the molecules under consideration. As there are many collisions between the molecules and the buffer gas, the internal energy of the molecules will be transferred to the cold buffer gas. Secondly, by placing a skimmer after a certain distance behind the nozzle the outer part of the beam will be cut off. This deletes all the molecules with large speed in the direction perpendicular to the direction of beam propagation, improving the translational cooling. This method is called geometric cooling. It has not to be used in the current study, because due to nature of multiphoton processes only the inner part of the beam will be analyzed.

2.3 The spectrum of energetic states of the molecule

The mechanism of photodissociation discussed in the chapter 2.1 includes one or several transitions between the energetic states of the molecule. To clarify the changes in the molecule occurring after the transitions the principles of energetic states description are discussed in the current chapter with a particular focus on the electronically excited states of HCl and borazine molecules.

The spectrum of the energetic states of any molecule is defined by the set of the solutions of the time-independent Schrödinger equation:

$$\hat{H}\Psi = \left(\hat{T} + \hat{V}\right)\Psi = E\Psi \tag{2.3.1}$$

where $\hat{T}$ and $\hat{V}$ are the operators of kinetic and potential energy of all the particles, which form the molecule. In a general case the molecule consists of N nuclei and n electrons. The eigenvectors of the equation (2.3.1) (wavefunctions) depend on the coordinates of all particles $\Psi(\vec{r}_i, \vec{r}_\alpha)$. $\vec{r}_i$ (i=1,2,…n) are the coordinates of the electrons, and $\vec{r}_\alpha$ (α=1,2,…N) are the coordinates of the nuclei. The full information about the spectra and electronic structure of diatomic or polyatomic molecules can be found in the fundamental monographies of Herzberg

[4,5]. In the following chapters only the aspects important for HCl and borazine molecules are discussed.

2.3.1 The discrimination of the motion corresponding to different degrees of freedom of the molecule

The Schrödinger equation describes all kinds of motion known in classical mechanics: the translational motion and rotation of molecule as a rigid structure, the displacement of the nuclei and the motion of the electrons. The solution of the equation can be simplified in case of the disjunction of different kinds of motion. Because of the homogeneity of the space an arbitrary coordinate system can be replaced by the coordinate system with the center in the center of mass of molecule (molecular coordinate system). As a result the translational motion can be excluded from the analysis.

In the molecular coordinate system the Hamiltonian of the system can be written as a sum:

$$\hat{H} = \hat{H}_e + \hat{H}_V + \hat{H}_R + \left(\hat{H}_{eR} + \hat{H}_{VR}\right) \tag{2.3.2}$$

The first three operators in the sum are the Hamiltonians, describing one kind of motion (subscript e – motion of electrons, subscript V – vibration, subscript R - rotation). The operators, which include the kinematic interactions of different kinds of motion, are collected in the brackets. The electrostatic interaction of the electrons and nuclei, defining the electron-vibrational coupling, is included in the operator $\hat{H}_e$.

The assumption that the rotational motion can be separated from other kinds of motion allows one to analyze the task of electron-vibrational coupling:

$$\left(\hat{H}_e + \hat{H}_V\right)\Psi(\vec{r}_i, \vec{r}_\alpha) = E\Psi(\vec{r}_i, \vec{r}_\alpha) \tag{2.3.3}$$

The Coulomb forces, influencing the electrons and nuclei, have the same order of magnitude, while the electron mass is much smaller than the mass of the nuclei. That results in a much higher speed of the electrons. During the characteristic time of electron motion, the displacements of the nuclei are approximately negligible, and one can fix the nuclei positions. Due to this the Schrödinger equation can be modified to the form, which describes only the electronic motion:

$$\left[\hat{T}_e + \hat{V}(\vec{r}_i, \vec{r}_{\alpha e})\right]\Psi^e = E^e\Psi^e \tag{2.3.4}$$

For a set of nuclear configurations the solution of the equation (2.3.4) gives the set of wave functions $\Psi_k^e(\vec{r}_i,\vec{r}_{\alpha e})$ and energies $E_k^e(\vec{r}_\alpha)$, where nuclei positions are just a parameter. The set $E_k^e(\vec{r}_\alpha)$ defines the potential surface of the electronic k-state, while the set $\Psi_k^e(\vec{r}_i,\vec{r}_{\alpha e})$ is used as a basis to solve the Schrödinger equation in a form (2.3.3):

$$\Psi(\vec{r}_i,\vec{r}_\alpha) = \sum_k \Psi_k^V(\vec{r}_\alpha)\Psi_k^e(\vec{r}_i,\vec{r}_{\alpha e}) \tag{2.3.5}$$

In case of the negligible nonadiabaticity, the general solution of the electron-vibrational task is defined by the expressions:

$$E_{kV} = E_k^e + E_k^V \tag{2.3.6}$$

$$\Psi_{kV} = \Psi_k^e(\vec{r}_i,\vec{r}_\alpha)\Psi_k^V(\vec{r}_\alpha) \tag{2.3.7}$$

The presented approach characterizes the Born-Oppenheimer approximation.

The contribution of electronic, vibrational and rotational excitation in the internal energy of the molecule can be estimated. In the classic theory of interaction of the radiation with the molecules the absorption and the emission of the light correlate with the vibration of the oscillators. The frequency of the vibration of an electron is defined by the expression $\nu_e = \frac{1}{2\pi}\sqrt{\frac{k}{m}}$, where k is a force constant, which is defined by the field in the molecule, influencing the electron vibration. The similar expression with the replacement of the mass of electron by the reduced mass of the nuclei defines the frequencies of the oscillators, connected with the nuclear vibrations. As it was mentioned above the Coulomb forces, acting on the electrons and on the nucleus, have the same order of magnitude. Since the mass of an electron m is much smaller than the mass of a nuclei M, one can assume $E_k^V/E_k^e \sim \sqrt{m/M}$. To compare the energies of electronic and rotational excitation the Bohr model of an orbital motion of an electron is used. The energy of this motion is $\frac{\vec{L}^2}{2ma^2}$, and the energy of the rotational motion of the molecule with the mass M is proportional to $\frac{\vec{L}_R^2}{2M\rho^2}$. Since $L \sim L_R \sim h/2\pi$ and $a \sim \rho$, $(E_{kV}^R/E_k^e) \sim (m/M)$. From these expressions one can calculate the ratio of electronic, vibrational and rotational excitations, and evaluate their contribution in the internal energy.

To obtain the absolute energy one can use the value of $E_k^e = 5\ eV$ basing on the data of atomic spectroscopy. As a result the energy of vibrational excitation can be estimate in the range 0.1 – 0.5 eV depending on the nuclear mass, and the energy of rotational excitation has to be another two orders of magnitude smaller. As a result the spectrum of molecular states consists of the electronic states spaced by several eV. The electronic states have a fine vibrational structure. The vibronic state in their turn can be characterized by even more fine structure, defined be the rotational degrees of freedom.

Basing on the performed estimations one can conclude, that the transitions between two electronic states are in the visible or ultraviolet region, the transitions between vibrational states of one electronic state are in IR region, the transitions between rotational states of one vibronic state – in the far IR region.

It is important to underline that not only the value of the energy E_k^e defines the electronic state, but the wavefunction Ψ_k^e as well. Several different wavefunctions Ψ_{ks}^e (s=1,2,…,m) can correspond to one value of energy. Such states are called degenerated.

2.3.2 Classification of the electronic states on the examples of Borazine and HCl

One of the most informative classification of molecular states uses the symmetry properties of their wavefunctions. Mulliken introduced the special system of the designation of symmetry types, which characterize the wavefunctions of electronic states. The description of this classification of the electronic states is given for the example of the borazine molecule, discussed in the chapter 3.

Borazine is a molecule of the point symmetry group D_{3h} (Fig. 2.3.1). This group includes five types of elements of symmetry in addition to identity: triad axis C_3, dyad axis C_2, the reflection plane σ_h perpendicular to the symmetry axis of highest order C_3, the reflection plane σ_v including the symmetry axis of highest order C_3 and the axis of improper rotation of third order S_3. For the non-degenerate states the designation A is used. The doubly degenerate states are designated by the letter E. If the wavefunction of an electronic state is symmetric in relation to the reflection in the σ_h plane, this state is marked by the superscript '; if the wavefunction is asymmetric – by the superscript ". In case of the reflection in the plane σ_v, the electronic state with the symmetric wavefunction are marked by the subscript $_1$, with asymmetric wave function – by the subscript $_2$.

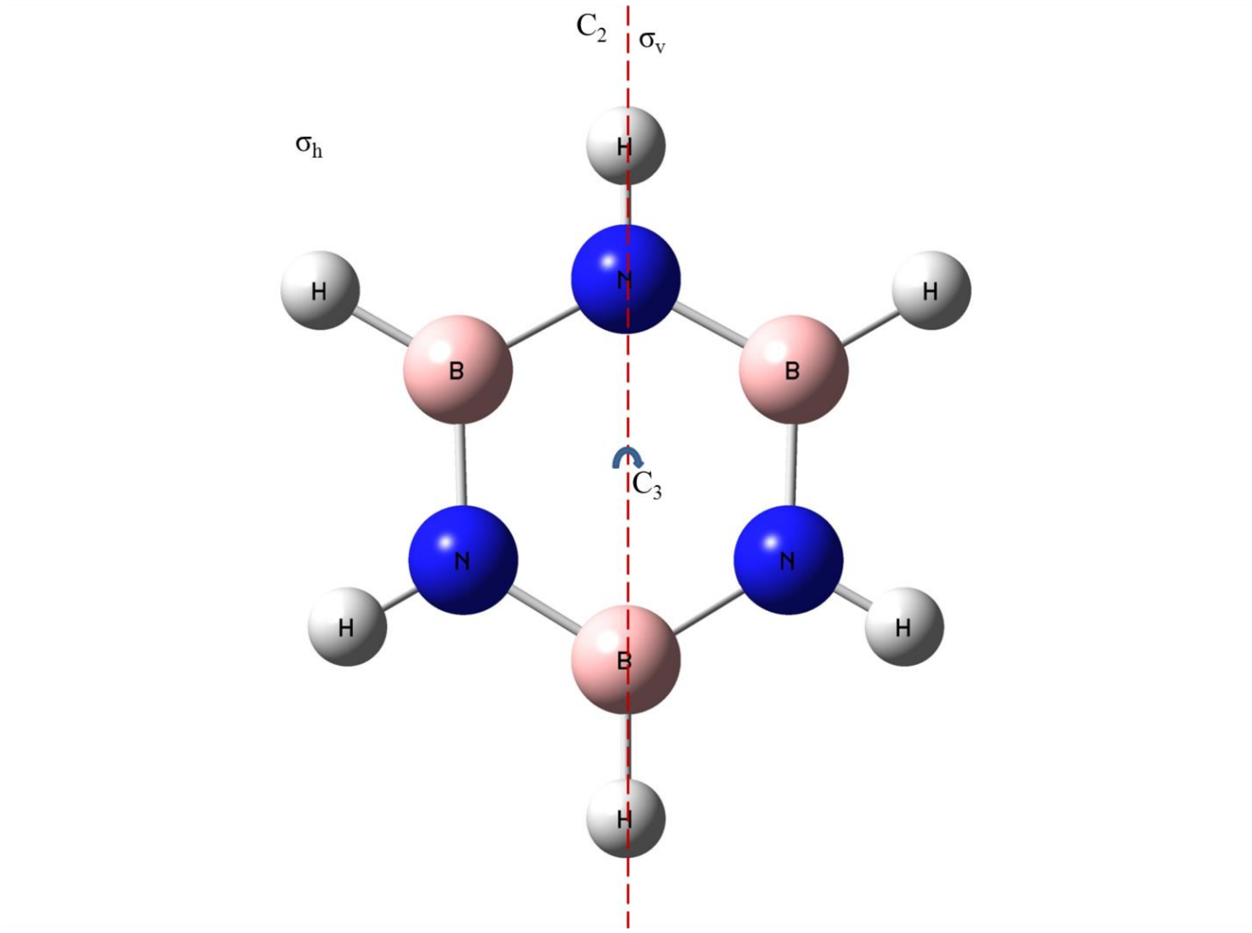

FIG. 2.3.1: Borazine (group of symmetry D_{3h}) molecule and the types of elements of symmetry: C_3 – symmetry axis of the highest order (3), σ_h – reflection plane perpendicular to C_3 axis, σ_V – reflection plane containing C_3 axis, dyad axis C_2 situated in σ_V plane, the axis of improper rotation of third order S_3 is a superposition of the rotation axis C_3 and reflection plane σ_h.

In case of linear molecules like HCl another designation of the electronic states is used. The field of force of the linear molecules has an axial symmetry. In this field exists an additional integral of motion, defining the projection of angular momentum onto the molecular axis. In cylindrical coordinates the wavefunction of one-electron with the potential of axial symmetry has the form: $\Psi = f(\rho, z)exp(i\lambda\varphi)$. This set of wavefunctions defines the set of eigenvectors of the operator of the angular momentum projection onto the axis z ($\hat{l}_z = -i\frac{h}{2\pi}\frac{d}{d\varphi}$), and a quantum number $\lambda = 0, \pm1, \pm2, \pm3, \ldots$ defines the eigenvalues of the angular momentum on the axis. The states of a one-electron system with $|\lambda|=0, 1, 2, 3, \ldots$ are designated as σ, π, δ, φ, … correspondingly. For multi-electron systems the projection of a total angular momentum on the particular direction is conserved and a quantum number $\Lambda = \sum_k \lambda_k$ is introduced. It has integer values as well. The state with $|\Lambda|=0, 1, 2, \ldots$ are designated as Σ, Π, Δ, … . The energy of the states does not depend on the sign Λ(λ), so that the states with $\Lambda \neq 0$ are doubly degenerate. The states Σ are not degenerate and can be characterized by the symmetric wavefunction (Σ^+) and by the asymmetric wavefunction (Σ^-).

The wavefunctions have to take into account the spin moment of the electrons. In case of a weak spin-orbit interaction the projection of the total spin on the linear molecule axis is used as s quantum number. The set of the states corresponding to one value of spin is called a multiplet. To show the spin characteristics of the electronic state an additional index, equal to 2S+1, is used. It is called multiplicity. In such a manner the full designation of the electronic state looks like: ${}^{2S+1}\Gamma_i$.

To be able to distinguish the electronic states of the same symmetry Mulliken suggested to mark the ground state before the sign of symmetry type by the symbol *X*, the excited states of the same multiplicity as the ground one – by the symbols A, B, C, …, the excited states of different multiplicity – by the symbols a, b, c… .

The detailed description of the electronic states of HCl and its molecular ion involved in the process of multiphoton photodissociation and REMPI is given in the previous paper of the group [6,7]. The ground electronic state of HCl is $X^1\Sigma^+$, while the ground and the first excited electronic states of the molecular ion HCl^+ are $X^2\Pi$ and $A^2\Sigma^+$, respectively. Fig. 2.3.2 shows a set of potential energy curves of HCl. The neutral states are presented by solid lines and ionic states by dashed lines.

The ground $X^1\Sigma^+$ and excited $B^1\Sigma^+$ states are shown in black, the ionic $X^2\Pi$ ground state is shown in red and the ionic $A^2\Sigma^+$ excited state is shown in blue. The same color coding has been used for the neutral Rydberg states converging either to the $X^2\Pi$ or to the $A^2\Sigma^+$ state. Asymptotically, the $X^2\Pi$ ground ionic state correlates with neutral ground state atomic hydrogen and a chlorine ion ($H + Cl^+$) as opposed to the $A^2\Sigma^+$ state which asymptotically correlates with an H^+ ion and a neutral ground state chlorine atom ($H^+ + Cl$).

Accordingly, red and blue colored Rydberg states correlate with the corresponding ground and excited neutral atoms ($H + Cl^*$ and $H^* + Cl$). The Rydberg states shown in Fig. 2.3.2 were obtained by shifting the corresponding ionic curve by the ionization energy of the excited state (H^* or Cl^*) atom. Only few of the neutral Rydberg states are shown in Fig. 2.3.2 in order to illustrate the general scheme rather than to obscure it by too many details.

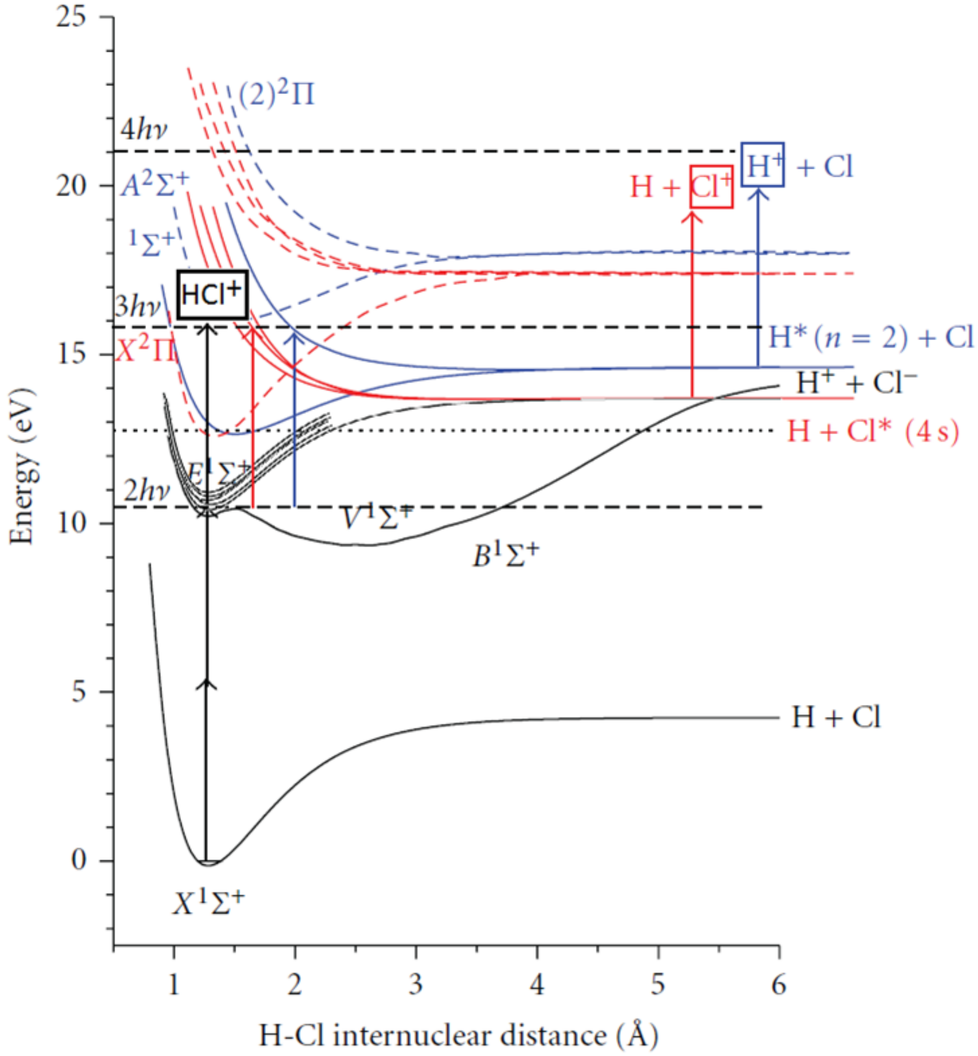

FIG. 2.3.2: Potential energy curves of HCl.

Generally, neutral Rydberg states occur as bound and as repulsive states, just like the corresponding ionic states. In Fig. 2.3.2, the "full" set of bound and repulsive Rydberg states is only shown for the "blue" curves correlating to H*(n = 2) + Cl, while the bound state is omitted for the "red" Rydberg states correlating to H + Cl*. One of those bound Rydberg states is responsible for the inner potential well of the B state (i.e., the E$^1\Sigma^+$ state in 0th order approximation) [8]. The outer potential well of the B state (the V$^1\Sigma^+$ state in 0th order approximation) is due to the ion-pair curve correlating to H$^+$ + Cl$^-$ products [8]. Here, for larger distances the interaction is mainly Coulombic giving rise to the energy minimum at rather large internuclear distances between 2 and 3 Å. It is important to note that the energy of the asymptotic products H$^+$ + Cl$^-$ lies above the energy of the H + Cl*(4s) system (red solid curve), but below the energy of the H*(n = 2) + Cl system (blue solid curve).

2.4 Principles of initial velocity vector definition: Ion Imaging

In the chapter 2.1 it was shown that the knowledge of the momentum vector (or velocity vector) is needed to study the photodissociation dynamics, while in the chapter 1.1 it was mentioned, that 3D imaging method allows to define the components of momentum vector from the coordinates of impact of flying products onto the position sensitive detector and from its time of arrival on the detector. Now the principles of this definition have to be discussed in detail.

The ion imaging methods work not directly with the primary products, but with their ions. The ions are produced by REMPI (resonance enhanced multiphoton ionization). This allows one to direct all the ionized products towards the detector by means of the acceleration field that improves the detection in comparison to simpler method of photofragment translational spectroscopy. In addition to this acceleration region one has to introduce a field free region (drift region) to obtain the ionized products spatial focusing in the spectrometer axis of symmetry. Together the acceleration and drift regions form the time-of-flight (TOF) spectrometer.

In case of the Ion Imaging method a homogeneous electrostatic field oriented along the spectrometer symmetry axis (Z) is applied to the acceleration region. Because of the field configuration the task of the analysis of three-dimensional motion of the ions in the spectrometer can be replaced by the task of separate analysis of one-dimensional motion in the three directions, defined by the laser beam (X), molecular beam (Y) and by the spectrometer symmetry axis. The center of the coordinate system (x=y=z=0) is defined by the position of product generation. Under the action of the electrostatic field the charged particles are accelerated in Z-direction, while in X and Y-directions the molecular motion is not influenced by the electric field.

By means of the time-resolving delay line anode detector the position of ion impact on the detector and the time-of-flight in the spectrometer are measured (Fig 2.4.1). The impact of a hypothetical particle with zero momentum vector $\vec{p} = (0,0,0)$, generated at $t=0$, defines the reference point of the measurement. On the basis of the measured values the X- and Y-components of the initial velocity vector of the produced ion are obtained:

$$v_x = \frac{\Delta x}{t} \tag{2.4.1}$$

$$v_y = \frac{\Delta y}{t} \tag{2.4.2}$$

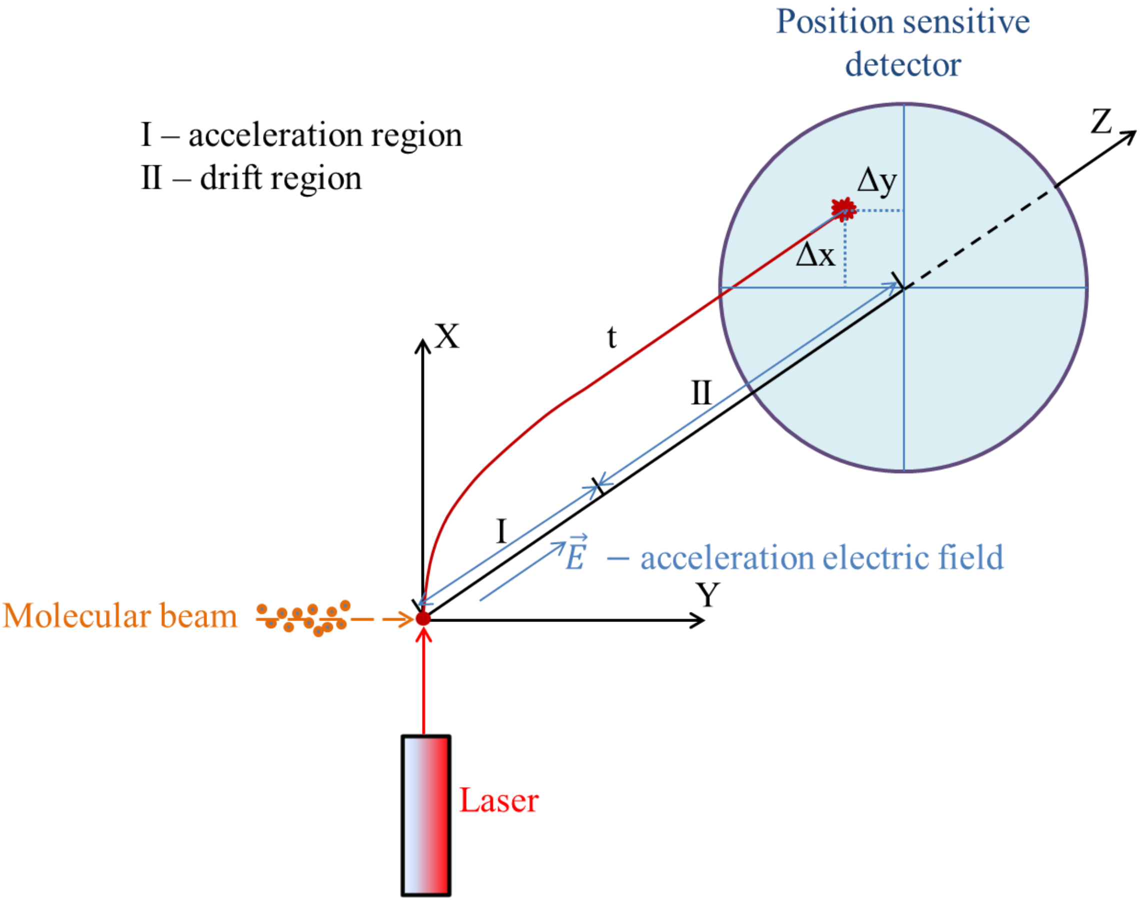

FIG. 2.4.1: Schematic representation of the Ion Imaging method.

To calculate the Z-component of the initial velocity vector it is necessary to examine the motion of the ion in Z-direction: uniformly accelerated in the acceleration region and steady in the drift region.

The uniformly accelerated motion of the ion is characterized by the simple kinematics formulae:

$$z = z_0 + v_{z0}t + \frac{at^2}{2}, \tag{2.4.3}$$

$$v_{za} = v_{z0} + at. \tag{2.4.4}$$

To simplify the formula (2.4.3) the zero of the Z-axis is placed in the point, where the ion has been produced. This makes the value z_0 equal to zero. At the time moment equal to the time-of-flight in the acceleration region with the length *s* the equation (2.4.3) can be written:

$$s = v_{z0}t_a + \frac{at_a^2}{2}\,. \tag{2.4.5}$$

Before further analysis one needs to study the particular case of zero z-component of the initial velocity vector ($v_{z0} = 0$). The formulae (2.4.5) and (2.4.4) are reduced to:

$$s = \frac{at_{a0}^2}{2}\,, \tag{2.4.6}$$

$$v_{za} = at_{a0}\,. \tag{2.4.7}$$

From these formulae z-component of the velocity vector on the boundary between acceleration and drift region is obtained:

$$v_{za}^2 = 2a^2\frac{s}{a} = 2as = v_a^2\,. \tag{2.4.8}$$

The formula (2.4.5) can be rewritten in the form of the squared equation:

$$t_a^2 + \frac{2v_{z0}}{a}t_a - \frac{2s}{a} = 0\,. \tag{2.4.9}$$

The solution, which gives the time-of-flight in the acceleration region in the general case, is:

$$t_a = -\frac{v_{z0}}{a} + \frac{1}{a}\sqrt{v_{z0}^2 + 2sa} = 2s\left(-\frac{v_{z0}}{2sa} + \frac{1}{2sa}\sqrt{v_{z0}^2 + 2sa}\right). \tag{2.4.10}$$

The formula can be modified, using the formula (2.4.8):

$$t_a = \frac{2s}{v_a}\left(-\frac{v_{z0}}{v_a} + \frac{1}{v_a}\sqrt{v_{z0}^2 + v_a^2}\right) = \frac{2s}{v_a}\left(-\frac{v_{z0}}{v_a} + \sqrt{1 + \frac{v_{z0}^2}{v_a^2}}\right). \tag{2.4.11}$$

The fact, that the energy release after photodissociation is about several electronvolts, while the ion is accelerated to the energy of several hundred electronvolts, allows to evaluate the ratio $\frac{v_{z0}}{v_a} << 1$. Due to this evaluation one can write the Taylor series for the square root in the expression (2.4.11) and obtain the final expression for the time-of-flight in the acceleration region:

$$t_a = \frac{2s}{v_a}\left(-\frac{v_{z0}}{v_a} + 1 + \frac{v_{z0}^2}{2v_a^2}\right) \tag{2.4.12}$$

The obtained expression for the time-of-flight in the acceleration region (2.4.11) can be used to calculate the Z-component of the velocity vector on the boundary between the acceleration and the drift regions in the general case:

$$v_{za} = v_{z0} + at_a = v_{z0} + \frac{2sa}{v_a}\left(-\frac{v_{z0}}{v_a} + \sqrt{1 + \frac{v_{z0}^2}{v_a^2}}\right) \tag{2.4.13}$$

The expression can be simplified using the formula (2.4.8):

$$v_{za} = v_a\sqrt{1 + \frac{v_{z0}^2}{v_a^2}} \tag{2.4.14}$$

The ion flies with this speed in the drift region. Because of the steady character of the motion the time-of-flight in the drift region is calculated according to the formula:

$$t_d = \frac{d}{v_{za}}\,, \tag{2.4.15}$$

or:

$$t_d = \frac{d}{v_a}\frac{1}{\sqrt{1 + \frac{v_{z0}^2}{v_a^2}}}\,. \tag{2.4.16}$$

To modify the expression the Taylor series is used once again for the square root in the power minus one. The final expression for the time-of-flight in the drift region is:

$$t_d = \frac{d}{v_a}\left(1 - \frac{v_{z0}^2}{2v_a^2}\right) \tag{2.4.17}$$

The complete time-of-flight in the spectrometer is the sum of both times:

$$t = t_a + t_d\,, \tag{2.4.18}$$

$$t=\frac{2s}{v_a}\left(1-\frac{v_{z0}}{v_a}+\frac{v_{z0}^2}{2v_a^2}\right)+\frac{d}{v_a}\left(1-\frac{v_{z0}^2}{2v_a^2}\right). \tag{2.4.19}$$

After the collecting of similar terms:

$$t=\frac{1}{v_a}(2s+d)-\frac{2s}{v_a}\frac{v_{z0}}{v_a}+\frac{v_{z0}^2}{2v_a^2}\frac{1}{v_a}(2s-d) \tag{2.4.20}$$

To avoid the dependence of the complete time-of-flight on the square of Z-component of the initial velocity vector the parts of the spectrometer are configured so that $2s=d$:

As a result the final expression of the complete time-of-flight is simplified:

$$t=\frac{4s}{v_a}-\frac{2s}{v_a^2}v_{z0}. \tag{2.4.21}$$

The time-of-flight in the particular case of zero Z-component of initial velocity vector is:

$$t_0=\frac{4s}{v_a}. \tag{2.4.22}$$

Replacing the coefficient before Z-component of the initial velocity vector due to the formula (2.4.8):

$$t=t_0-\frac{1}{a}v_{z0}. \tag{2.4.23}$$

The last expression can be rewritten to obtain the general formula for the Z-component of the initial velocity vector:

$$v_{z0}=a(t_0-t) \tag{2.4.24}$$

The value t_0 can be calculated due to the formulae (2.4.8) and (2.4.22) or obtained from the time-of-flight profile measured in the experiment.

The formulae (2.4.1), (2.4.2) and (2.4.23) are correct only for the homogeneous acceleration field. The Velocity Map Imaging method uses an electrostatic lens to focus the trajectories of the ions with the same velocity vector in a single point on the detector. The lens makes the field in the spectrometer inhomogeneous. As a result the motions in X-, Y- and Z-direction are correlated and the task of the velocity vector definition on the basis of coordinates of ion impact on the detector surface demands the use of the numerical methods of trajectory simulation.

Sebastian Kauczok and coauthors have shown how these methods could be applied to obtain the 3D “velocity map” [9].

In the current dissertation mainly the 3D Ion Imaging method is used.

2.5 Anisotropy

The angular distribution of the products of the process of photodissociation, occurring in the consequence of linearly polarized light absorption, can be easily predicted in a classical approach. Linearly polarized light excites preferentially those molecules, whose transition dipole moments $\vec{\mu}$ are parallel to the electric field vector $\vec{E}$. The transition probability $P(\theta_{\mu E})$ is given by the equation (2.4.1):

$$P(\theta_{\mu E}) \sim \left|\vec{E} \cdot \vec{\mu}\right|^2 \sim E^2 \cdot \mu^2 cos^2\theta_{\mu E} \tag{2.5.1}$$

where $\theta_{\mu E}$ is the angle between the vector $\vec{E}$ and the transition dipole moment $\vec{\mu}$. The geometric structure of the molecule defines the relative orientations of transition dipole moment $\vec{\mu}$ and the fragment recoil velocity $\vec{v}$.

Denoting the angle between the fragment recoil velocity $\vec{v}$ and the transition dipole moment $\vec{\mu}$ as $\theta_{v\mu}$, the spatial fragment distribution can be written with the use of anisotropy parameter β [10,11]:

$$f(V, \theta_{vE}) = \frac{1}{4\pi} f(v)[1 + \beta P_2(\cos\theta_{vE})] \tag{2.5.2}$$

where

$$\beta = 2P_2(\cos\theta_{v\mu}) \tag{2.5.3}$$

P_2 is the second Legendre polynomial given by the formula

$$P_2(\cos\theta) = \frac{1}{2} \cdot (3cos^2\theta - 1) \tag{2.5.4}$$

It is easy to note, that the limiting values of anisotropy parameter β are +2 and -1. For the diatomic molecule β parameter equal to -1 corresponds to the case where $\vec{v}$ and $\vec{\mu}$ are perpendicular to each other, while the value of β parameter +2 is obtained if $\vec{v}$ and $\vec{\mu}$ are parallel to each other. For larger molecules the β parameter can vary in the range between +2 and -1 depending on the molecular geometry.

However all these arguments are correct only in case of instantaneous decay, or, in other words if the photodissociation is direct. If the lifetime of the dissociative excited state τ is larger than the rotation period τ_{rot} of the parent molecule, the angular distribution is smeared out and the resulting anisotropy is lowered according to [12,13]:

$$2P_2\left(\cos\theta_{V\mu}\right)\frac{\omega^2\tau^2+1}{4\omega^2\tau^2+1} \tag{2.5.5}$$

where ω is the molecule's angular velocity.

2.6 Dissociating laser beam structure

In the chapter 6 the quantitative characterization of the steps of multiphoton dissociation of HCl is presented. Namely the two-photon absorption cross-section is measured. For this purpose it is very important to know the structure of the laser beam after its diffraction or focusing by different optical elements of the experimental set-up.

2.6.1 The free space modes and their transformation by the lenses

Because of the high directionality of the laser beam it is close to the plane wave. The difference consists in the fact, that the intensity distribution in the plane perpendicular to the propagation direction is not homogeneous, and the phase front differs from the plane. One need to search the solution of the reduced wave equation in the form:

$$\Psi = E(x,y,z)e^{ikz} \tag{2.6.1}$$

where *E(x,y,z)* – is the slowly changing complex function, which defines the properties of the laser beam, distinguishing the beam from the plane wave. The fast oscillation in Z-direction is determined by the presence of the exponential factor in the expression (2.6.1). After the use of the Laplace operator to the function Ψ one receives:

$$\Delta\Psi = \left(\frac{\partial^2 E}{\partial x^2}+\frac{\partial^2 E}{\partial y^2}+\frac{\partial^2 E}{\partial z^2}+2ik\frac{\partial E}{\partial z}-k^2E\right)e^{ikz} \tag{2.6.2}$$

In the expression (2.6.2) one can ignore the second derivative of the function E with respect to z in comparison to the first one:

$$\frac{\partial^2 E}{\partial x^2}+\frac{\partial^2 E}{\partial y^2}+2ik\frac{\partial E}{\partial z}=0 \tag{2.6.3}$$

The obtained expression presents the equation of the parabolic type. It is easy to show, that the so-called Gaussian beam satisfies the equation (2.6.3).

A coherent light beam with the gauss distribution of the field:

$$E = a * exp\left[i\left(p + \frac{k}{2q}r^2\right)\right] \tag{2.6.4}$$

has a fundamental sense in the theory of the wave beams. It is called the ground mode. The parameter p – is a complex phase deviation in case of the light propagation in Z-direction, while q – is a complex parameter of the beam, defining the Gaussian distribution of the field on the distance from the Z-axis. The parameter q describes the curvature of the wave front as well.

To demonstrate the properties of the ground mode in details the complex parameter q has to be expressed in terms of two real beam parameters R and w:

$$\frac{1}{q} = \frac{1}{R} + i\frac{\lambda}{\pi w^2} \tag{2.6.5}$$

The physical meaning of these parameters can be demonstrated after the substitution of the expression (2.6.5) in (2.6.4). One can see, that R is the curvature radius of the wave front, while w characterizes the deviation of the field E in the plane perpendicular to the beam propagation direction. The field distribution in this plane, as it is shown on the Fig. 2.6.1, follows the Gaussian character and w is equal to the distance on which the field amplitude decreases by the factor of e in comparison to the value on Z-axis.

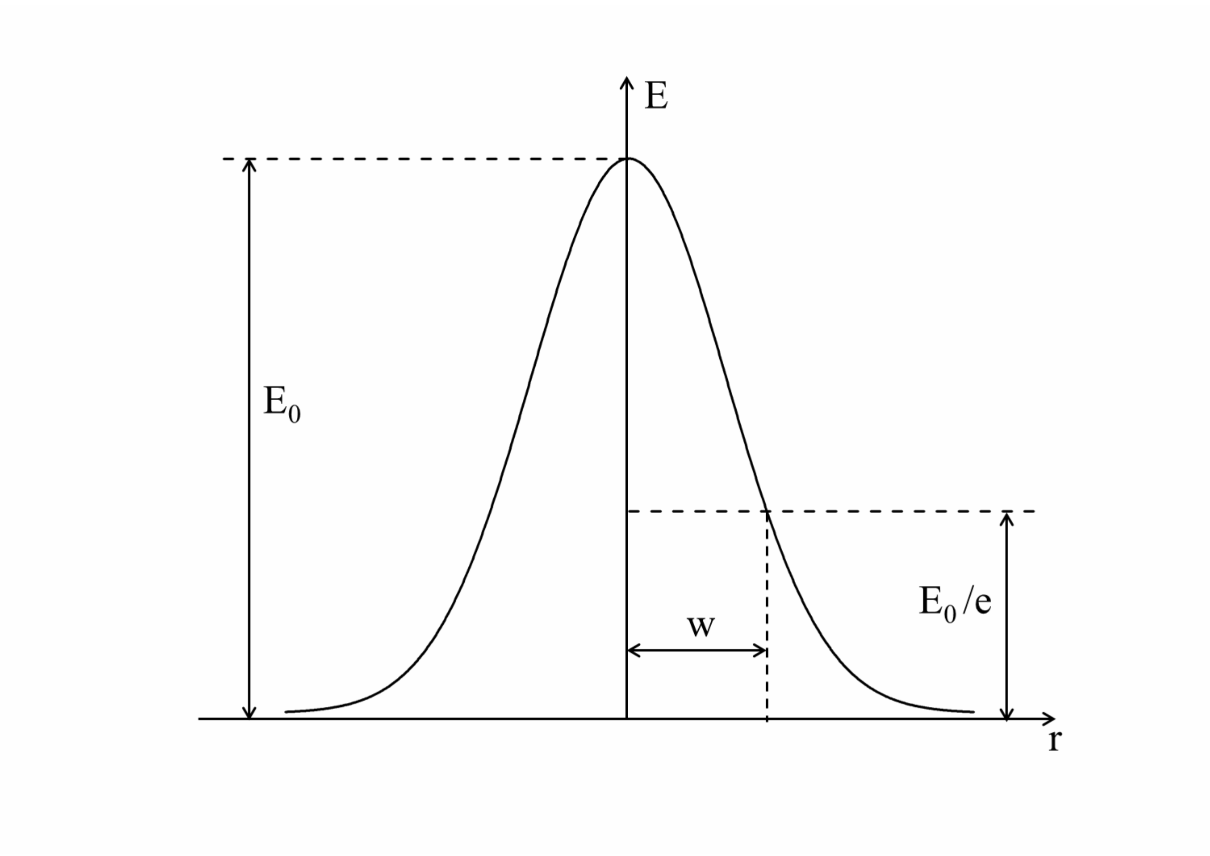

FIG. 2.6.1: Transverse distribution of amplitude of the field for the ground mode.

It is important to underline, that the ground mode has the gauss character of the field distribution with changing width in any plane perpendicular to propagation axis. The parameter w is called the radius of the beam, and *2w* – the diameter of the beam. In the particular plane, known as the beam waist, the gaussian beam has a minimal diameter $2w_0$. The zero of Z-axis is place in this plane, where the phase front is flat. On a distance z from the beam waist the complex parameter of the beam is:

$$q = \frac{\pi w_0^2}{i\lambda} + z \tag{2.6.6}$$

Comparing the expressions (2.6.5) and (2.6.6), it is easy to obtain the important formulae:

$$w^2(z) = w_0^2 \left[1 + \left(\frac{\lambda z}{\pi w_0^2}\right)^2\right] \tag{2.6.7}$$

$$R(z) = z \left[1 + \left(\frac{\pi w_0^2}{\lambda z}\right)^2\right] \tag{2.6.8}$$

Finally the expression describing the ground mode is:

$$\Psi(r,z) = \frac{w_0}{w} exp\left\{i(kz - \Phi) - r^2\left(\frac{1}{w^2} - \frac{ik}{2R}\right)\right\} \tag{2.6.9}$$

where Φ is a differences of phases between the gaussian beam and the plane wave.

Other solutions of the parabolic equation (2.6.3) give the higher modes of the free space and can be presented in cylindrical coordinate system:

$$\Psi(r,\varphi) = \frac{w_0}{w}\left(\sqrt{2}\frac{r}{w}\right)^l L_p^l\left(2\frac{r^2}{w^2}\right) exp\left\{i(kz - \Phi) - r^2\left(\frac{1}{w^2} - \frac{ik}{2R}\right)\right\}\begin{Bmatrix}\cos l\varphi \\ \sin l\varphi\end{Bmatrix} \tag{2.6.10}$$

where L – is a Laguerre polynomial.

An ideal lens conserves the ground mode of the beam. The modes of higher orders are converted into the modes of the same orders. However the parameters R(z) and w(z) are changed. To obtain the relationship between the input parameters before the lens and the output parameters after the lens, the task of a spherical wave modification by an ideal lens has to be discussed (Fig. 2.6.2).

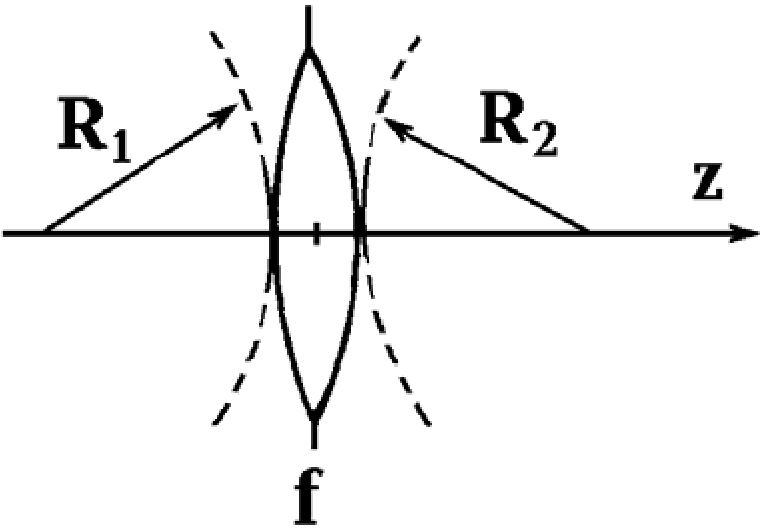

FIG. 2.6.2: Modification of the wave front by a lens.

The spherical wave of the radius R_1 on one side of the lens correlates with the spherical wave of the radius R_2 on the other side of the lens according to the formula:

$$\frac{1}{R_2} = \frac{1}{R_1} - \frac{1}{f} \tag{2.6.11}$$

The curvature radius is assumed to be positive, if the wave front is convex relative to the point z→∞. The wave front of any mode of the beam is converted by a lens in the same way. If the lens is thin and radii of the beams from side of the lens are equal, the relationship between the complex parameters of the input and output beams can be written by analogy with (2.6.11):

$$\frac{1}{q_2} = \frac{1}{q_1} - \frac{1}{f} \tag{2.6.12}$$

2.6.2 Diffraction of the laser beam

The orthogonal properties of free-space modes give the possibility to calculate the field of the diffraction, using an approach based on the decomposition of field of diffracted beam in the free-space modes. This approach in many cases is easier than the approach, which uses the scalar theory of the diffraction. It is especially effective in case of the weak diffraction of the laser beam, discussed in the chapter 6. The smooth profile of the change of laser beam amplitude in the plane of decomposition allows to exclude from the analysis the modes with the high index.

The laser wave arrives on an arbitrary form hole in a non-transparent screen. The cross distribution of the field amplitude is defined by the function $U(r,\varphi)$. The field of the diffracted wave can be presented as a superposition of the Laguerre-Gaussian free-space modes. The cross distribution of the field of these modes is defined by the orthogonal functions Ψ_{pl}. Than the amplitude of the light field on the distance z from the hole can be presented:

$$u_D(r,\varphi,z) = \sum_{p,l}^{\infty} C_{pl} \Psi_{pl}(r,\varphi,z) \tag{2.6.13}$$

Z-axis coincides with the direction of Laguerre-Gaussian modes propagation (plane of the hole z=0). The coefficients of the decomposition can be found according to the expression

$$C_{pl} = \int u(r,\varphi) \Psi_{pl}(r,\varphi) dS \tag{2.6.14}$$

where the integration is performed over the area of the hole S.

As an example of such approach the particular case of the arrival of the ground mode of the laser on the circular diaphragm with radius r_0 and with the center situated on the Z-axis. This particular case is important for the discussion in the chapter 6.

The light field on the hole is described by the function

$$u_A(r) = \frac{1}{\bar{w}}\sqrt{\frac{2}{\pi}}exp\left(-\frac{r^2}{\bar{w}^2}\right) \tag{2.6.15}$$

where $\bar{w}$ – radius of the beam in the plane of hole. Because of the axial symmetry of the task only the coefficient with the index l=0 (C_{p0}=C_p) are nonzero. Introducing the dimensionless parameters $\kappa = \frac{z}{\bar{w}}$ and $\chi = \frac{\lambda}{\bar{w}}$ the cross distribution of the intensity of the wave on the distance z from the diaphragm can written in the form

$$I(x) = u_D u_D^* = \sum_{p,q} C_p C_q L_p(2x^2) L_q(2x^2) exp(-2x^2)\cos(\theta_{pq})\frac{2}{\pi w^2(z)} \tag{2.6.16}$$

$$x = \frac{r}{w} \tag{2.6.16a}$$

$$\theta_{pq} = 2(p-q)arctg\left(\frac{\kappa\chi}{\pi}\right) \tag{2.6.16b}$$

$$w(z) = w_0\sqrt{1+\left(\frac{\kappa\chi}{\pi}\right)^2} \tag{2.6.16c}$$

To guarantee the convergence of series (2.6.16) it is efficient to make the decomposition using the modes with the minimal beam radius w_0, equal to r_0, if $\alpha < 1$ and w_0=$\bar{w}$, if $\alpha \geq 1$, where $\alpha = \frac{r_0}{\bar{w}}$ is a parameter of beam limitation.

2.7 Statistical methods in the study of photodissociation

The processes of photodissociation differ in the distribution of final states because of the different dynamics. In case of the absence of any dynamical constraints one is limited to analyze only the product energy distribution (PED). The only simple model for treating these PED is the statistical one; however, there is a considerable diversity in its applications.

2.7.1 Phase space

Before the discussion of the application, used in the current dissertation, it is important to describe some basic aspects of general statistical theory. The general statistical theory was in details described by Landau and Lifshitz [14]. For the analysis performed in the chapter 3 the basics of phase space are only necessary.

The concept of phase space was developed in the late 19th century by Ludwig Boltzman, Henri Poincare, and Willard Gibbs [15]. In physics and mathematics it is used to describe the array of all possible states of the system. The state of any system of arbitrary complex is presented by one unique point in the phase space, and the evolution of the system by the motion of this point.

In a phase space, every degree of freedom or parameter of the system is represented as an axis of a multidimensional space; a one dimensional system is called phase line, while a two-dimensional system is called a phase plane. In case of the mechanical system the phase space has an even numbered dimensionality with spatial coordinates of the particles of the system and their linear momenta as the coordinates of the phase space. For example the phase space of the system, which includes only one free material point, has 6 dimensions, three of which are the normal coordinates, and three other – the components of the linear momentum.

2.7.2 Prior distributions

The statistical theory for product energy distributions is based on the phase space theory, originally developed by Light and co-workers (Pechukas ans Light, 1965; Light, 1964; Light and Lin, 1965) and applied to unimolecular reactions by Nikitin (1965, 1974) and Klots(1971, 1972, 1976). It assumes that all product states are populated with equal probability and has been applied to product energy distribution at several levels of complexity.

In the chapter 3 the energy distribution of the products of photodissociation after the absorption of a single photon will be discussed. For such analysis is only important the simplest modification of phase space theory called “prior distribution”, which in case of medium and large molecules gives the result close to that of more complex approaches.

To obtain the product energy distribution one need first of all to write the energy conservation law:

$$h\upsilon - D_0 = E_R \tag{2.7.1}$$

The energy release E_R is distributed among the internal energy of the products and their kinetic energy. To simplify the analysis the assumption that only one fragment can be internally excited is done. The formula for the energy release can be written in the next form:

$$E_R = E_K + E_I \tag{2.7.2}$$

Here E_I the internal energy of only one fragment, while E_K is the total kinetic energy of both fragments:

$$E_K = \frac{m_1 v_1^2}{2} + \frac{m_2 v_2^2}{2} = \frac{\mu V^2}{2} \tag{2.7.3}$$

Here μ is a reduced mass and V is a speed of relative motion.

In the statistical model the system of the fragments can be considered as the unique point, characterized by the coordinates in space (x, y, z) and by linear momentum components (p_x, p_y, p_z). As a result the system is described by the six-dimensional phase space, which contains all the translational states of the material point. Since the system is not dependent on the spatial coordinates the total number of the possible states is:

$$N = V \int \frac{dp_x dp_y dp_z}{h^3} \tag{2.7.4}$$

Here V is the volume of the spatial subspace. One can see that $\frac{dp_x dp_y dp_z}{h^3}$ is the density of translational states (per unit volume). The independence of the system on the spatial coordinates allows to analyze only three-dimensional linear momenta subspace. In this subspace the expression of the density of translational states gives the number of states in the small volume limited by dp_x, dp_y and dp_z. In passing from the subspace of Cartesian components of linear momentum to the subspace of the linear momenta in spherical coordinate the density of translational states is modified to:

$$\frac{p^2 dp\ sin\theta d\theta d\varphi}{h^3} \tag{2.7.5}$$

Because of the equal probability of all the orientation of the linear momentum, the expression (2.7.5) can be integrated over the total solid angle:

$$\frac{4\pi p^2 dp}{h^3}, \tag{2.7.6}$$

or in passing from the linear momentum to the energy scale:

$$\frac{4\pi (2m)^{\frac{3}{2}} \sqrt{E_K} dE_K}{h^3}. \tag{2.7.7}$$

Finally the expression $A_K \sqrt{E_K}$ shows the density of translational states per unit volume, unit solid angle and unit energy. The constant A_K collects all the constants of the expression (2.7.7). It disappears after one normalizes a prior distribution.

In terms of the internal energy the density of translational states is $A_K\sqrt{E-E_I}$. Taking into account the possible degeneracy of the internal states *g(n)* one can obtain the density of the excited states of one of the fragments with the energy E_{In}:

$$\rho(n;E)=A_K g(n)\sqrt{E-E_{In}} \tag{2.7.8}$$

n – is a set of all quantum numbers, which characterize the degenerated state.

The total density of states at the energy *E* is the sum over all the quantum numbers:

$$\rho(E)=A_k\sum_n g(n)\sqrt{E-E_{In}} \tag{2.7.9}$$

The (normalized) prior distributions are therefore

$$P^0(n;E)=\frac{\rho(n;E)}{\rho(E)} \tag{2.7.10}$$

$$P^0(E_K;E)=\frac{\rho(E_K;E)}{\rho(E)} \tag{2.7.11}$$

Explicit expressions for the prior distribution require the expressions for the energies of the excited states.

In the chapter 3 the prior distribution are applied to analyze the process of borazine molecule photodissociation. The exact expressions of the energy of rovibrational states are presented as well. The set of the quantum numbers *n* contains the vibrational quantum number *v* and the rotational quantum numbers *j* and *k*.

References

---

[1] R. Schinke, *Photodissociation Dynamics*, Cambridge Monographs on Atoms, Molecular and Chemical Physics 1 (Cambridge University Press, 1993).

[2] J. M. Hayes, Chem. Rev. **87**, 745 (1987).

[3] R. Campargue, J. Chem. Phys. **88**, 4466 (1984).

[4] G. Herzberg, Spectra of Diatomic Molecules, Second edition, Van Nostrand Reinhold ISBN: 0-442-03365-0 (1950).

[5] G. Herzberg, Electronic Spectra and Electronic Structure of Polyatomic Molecules, Van Nostrand Reinhold ISBN: 0-442-03387-7 (1966).

[6] A.I. Chichinin, C. Maul, and K.-H. Gericke, J. Chem. Phys. **124** ,224324 (2006).

[7] C. Maul, A.I. Chichinin, and K.-H. Gericke, J. At. Mol. Opt. Phys. 410108 (2011).

[8] A. D. Pradhan, K. P. Kirby, and A. Dalgarno, J. Chem. Phys. **95**, 9009 (1991).

[9] S. Kauczok, N. Goedecke, A. I. Chichinin, M. Veckenstedt, C. Maul, and K.-H. Gericke, Rev. Sci. Instr. **80**, 083301 (2009).

[10] R. N. Zare, Mol. Photochem. **4**, 1 (1972).

---

[11] M. N. R. Ashfold, I. R. Lambert, D. H. Mordaunt, G. P. Morley, and C. M. Western, J. Phys. Chem. **96**, 2938 (1992).

[12] C. Jonah, J. Chem. Phys. **55**, 1915 (1971).

[13] G. E. Busch, and K. R. Wilson, J. Chem. Phys. **56**, 3638 (1972).

[14] L.D. Landau, and E.M. Lifshitz, *Statistical Physics. Vol. 5 (3rd ed.)*, Butterworth-Heinemann (1980).

[15] D. D. Nolte, Physics Today **63**, 33 (2010).

3 3D Velocity Map Imaging study of the 193 nm photodissociation of borazine

Abstract: The photodissociation of the borazine molecule at 193 nm was studied by 3D Imaging of the ejected hydrogen atom. A speed distribution with a maximum at 8250 m/s and a half width 3700 m/s as well as an anisotropy β-parameter of the velocity vector distribution were determined. The β-parameter is speed dependent, indicating the presence of two different dissociation processes. The ejected hydrogen products at lower speeds are the result of predissociation of the electronically excited state of borazine molecule, while the hydrogen atoms at higher speeds emerge from direct dissociation of borazine. Ab initio and phase space calculations suggest that in case of predissociation the borazinyl radical is vibrationally and rotationally excited. The excited vibrational modes of the radical correspond to the υ4 and υ10 modes of borazine molecule, activated in the vibronic transition resulting by the absorption of 193 nm radiation. In case of direct dissociation the β-parameter, being equal to 0.5±0.08, shows the relative orientation of the transition dipole moment and the recoil velocity. The contribution of B-H and N-H bonds in the processes of predissociation and direct dissociation is discussed.

3.1 Introduction

Borazine is an interesting molecule from a fundamental point of view owing to its structural similarity to benzene. On the other hand it has only recently become a popular precursor molecule for the production of BN ceramics and nanoparticles.

Borazine $B_3N_3H_6$ was synthesized the first time in 1926 by Stock and Pohland [1]. With electron diffraction the ring structure of borazine and its similarity with benzene was proven in 1938 by Bauer [2] and confirmed by Wiberg in 1940 [3]. In 1961 borazine polymers were synthesized [4] and in 1994 different borazine polymers were described by Paine [5]. BN ceramics are interesting because of their high temperature stability, corrosion and oxidation resistance. They are used in metallization, cosmetics and automotive industry [6,7]. Newer research has made it possible to create BN layers with low temperature by using borazine and an electron beam [8]. Also in 2013 the surface clustering of borazine-based supramolecules has been investigated [9].

The spectroscopic analyses of borazine started in 1939 with a Raman spectrum and an infrared absorption spectrum which were compared with benzene spectra by Crawford [10]. Subsequently, substituted borazine molecules were investigated in the infrared region by Porter in 1968 [11]. Further infrared spectra were measured by Niedenzu, Kartha and Silberman [12,13,14] and high resolution FTIR investigations were performed in 2001 [15].From these investigations the existence of 4A'$_1$, 3A'$_2$, 3A"$_2$, 7E' and 3E" vibrational modes was concluded. The A'$_1$, E' and E" vibrations are Raman active and the A"$_2$ and E' are infrared active vibrations, while the A'$_2$ vibration is inactive in both cases [12,13,14]. In 1947 an absorption spectrum of borazine was measured in the vacuum ultraviolet wavelength range by Platt [16]. In addition, substituted borazine molecules were investigated by absorption spectra in the ultraviolet region in 1949 [17] and compared with benzene and mesitylene. Ultraviolet measurements were further done by Kaldor [18] and Bernstein [19]. No absorption of borazine was found in the region 460-200 nm. Three electronic transitions were found in the region of 150 nm to 200 nm. The strongest one is the allowed 1E' − 3A'$_1$ transition. The other two are the forbidden 1A'$_2$ − 1A'$_1$ and 1A'$_1$ − 1A'$_1$ transitions [18]. The orbital structure was reviewed in 1971 [20].Further investigations focused on the π-electron interactions by comparing borazine with benzene and cyclohexane from which it is known that borazine has a planar structure with a D_{3h} symmetry and a delocalized system of π electrons [2,10,21].

Later works adressed also the two-photon absorption spectrum of borazine [22] and the photochemical exchange of H-Atoms with deuterium [23]. By photoelectron spectrometry the vertical ionization potential for borazine was determined to be 10.09 eV [24] and several substituted borazines were studied by the same technique [25]. The photochemistry was studied in 1972 where borazine produces H_2 after photolysis [26].

Only one investigation has been made on the photodissociation of borazine by Weiner and coworkers. They photolyzed borazine at 193 nm and detected the B3N3H5 and HBNH fragments by resonance enhanced multiphoton ionization (REMPI) and time-of-flight mass spectrometry (TOFMS). However, neither the H atom nor the three dimensional product speed distribution was observed [27].

So borazine plays an important role in synthesis and it is an interesting molecule for research. The present work investigates for the first time the photodissociation of borazine by state selective ionization of nascent atomic H fragments and analyzes the spatial and kinetic energy distribution by three-dimensional velocity map imaging. Results are interpreted by statistical analysis and ab initio calculations. Both N-H and B-H bonds have been found to break upon irradiation of the parent molecule with ultraviolet light, and the borazinyl fragment has been found to be moderately vibrationally excited.

3.2 Experimental

3.2.1 Set-up

The experimental set-up has been described in details in the previous publications [28,29,30]. Here we will only briefly present this set-up with an emphasis on the most important aspects for the present work.

The main part of the 3D velocity map imaging apparatus is a homebuilt TOF spectrometer mounted to a commercial 3D imaging detector consisting of a two stage micro channel plate (MCP) and a delay line anode (DL) (RoentDek) [31,32]. The TOF spectrometer consist of a pulsed nozzle (General Valve, Series 9, five ring electrodes, which define the acceleration region of approximately 5 cm length (depending on the laser path), a cylindrical field free drift region with the 10 cm length and two meshes separating the acceleration region from the drift region and the drift region from the detector. The acceleration potentials and the potential of the Einzel-lens (third electrode) were supplied by two voltage supplies (Stanford Research System, Model PS350).

The spectrometer and the detector are installed in a stainless steel vacuum vessel, evacuated by two turbo molecular pumps (TMPs, Pfeiffer TMU 260 P, 220 1/s) forepumped by a rotary vane pump filled with oil. Without any gas flow, the background pressure is approximately 10^{-7} mbar. When the nozzle is operating, the integral pressure is on the order of 10^{-5} mbar.

Borazine was purchased from ChemicalPoint and used without further treatment. A metal container with pure liquid borazine was placed in a cryostat at a temperature of -10°C. Argon at a pressure of 1-3 bar was flowed through the container such that on the exit line of the container a flow of a borazine-argon mixture was obtained. The percent content of borazine in the flow was not monitored. The mixture with a stagnation pressure of approximately 400 mbar is expanded through the pulsed nozzle in the spectrometer, forming a supersonic molecular beam.

On the spectrometer symmetry axis the molecular beam was intersected at a right angle by two counter propagating laser beams. The first beam (dissociation radiation) with the wavelength 193 nm was produced by an ArF excimer laser (Optex 3, Lambda Physik). The second beam (hydrogen detection radiation) was the result of frequency doubling of the output of a dye laser (Scanmate 2, Coherent) by a beta-barium borate (BBO) crystal. The dye laser was pumped by a Nd:YAG laser and delivery the tunable wavelength, which was scanned over the hydrogen [2+1] REMPI (2S,2s 2S,1s) transition at a wavelength of 243.12 nm. The detection beam was focused by an f = 0.3 m lens into the center of the molecular beam, while the 193 nm laser radiation was focused by an f = 0.45 m CaF2 lens. The lens was mounted on a combination of two motorized translation stages (Owis, LTM 80) making it possible to position the dissociation laser path very accurately relative to the dye laser.

The pulses coming from the ends of the DL were differentially amplified (KSU EDL DLA800), recorded by a four channel oscilloscope (Waverunner 6050, Quad 5Gs/s) and fitted by a Gaussian pulse shape in order to obtain the center of the peaks.

3.2.2 Laser system calibration

In case of two colors studies the problem of overlapping the laser beams in space and time has to be considered. To solve this problem the HBr photodissociation, which occurs at the same wavelength 193 nm, is used:

$$HBr + h\nu \rightarrow H + Br(\,^2P_J) \tag{3.2.1}$$

In a one color experiment HBr is photolyzed at a wavelength of 243.12 nm, which is also used for [2+1]-REMPI of resulting H-atoms. The distribution of the velocity vector of H atoms emerging from photodissociation of HBr is presented by two concentric spheres, which correspond to two channels of measured H atoms formation due to the two spin orbit states of the bromine partner fragment, $Br(^2P_{3/2})$ and $Br(^2P_{1/2})$.

In a two color experiment the fact that HBr can be photolyzed both at the REMPI detection wavelength 243.12 nm and at 193 nm (produced by an ArF excimer laser) is used. The H atoms produced by both wavelengths are subsequently ionized only by 243.12 nm radiation. As a result two new channels of H+ are observed in the H atoms velocity distribution by new spheres, sensitive to the position of the excimer laser beam. By displacing the mobile CaF2 lens the position of the excimer laser focus was adjusted until the spheres of the velocity vector distribution appearing in the two color experiment were concentric with the spheres in the one color experiment. In this case the best spatial overlap of both laser beams was reached.

3.3 Theory

3.3.1 Ab initio calculation

All calculations were performed using the Gaussian09 program package [33]. The geometries for Borazine molecule and Borazinyl radicals were optimized by Density Functional Theory (DFT) was used to optimize the geometries of Borazine molecule and Borazinyl radicals and to calculate their vibrational modes.

3.3.2 Phase space theory calculation

The coordinates of the phase space discussed in this work are the energies (or quantum numbers) of the internal degrees of freedom of the system. The calculations are used to define a probability density function, which shows the energy and speed distribution among the degrees of freedom. The main principle is the definition of a surface in phase space that separates the arrangements before and after dissociation. On this surface, placed in the region of asymptotic products, all energetically allowed states are assumed to be equally probable.

The probability density function that a system with N = n + k atoms splitting in two fragments with n and k atoms to be found in quantum states a_n and a_k is represented in the general form:

$$P^0(a_n, a_k; E) = \frac{g(a_n,a_k)\sqrt{E-\epsilon(a_n,a_k)}}{\sum_{a_n,a_k} g(a_n,a_k)\sqrt{E-\epsilon(a_n,a_k)}} \tag{3.3.1}$$

Here $g(a_n,a_k)$ is the degeneracy, which depends on the quantum number sets a_n and a_k, E is the total available energy and $\epsilon(a_n, a_k)$ is the internal energy of both products. The calculations were carried out for the borazine molecule, fragmenting into a hydrogen atom (n=1) and a borazinyl radical, consisting of 11 atoms (k=11).

Muckerman et al. obtained the probability density functions in case of the dissociation into an atom and a general nonlinear fragment pair [34]. To describe the internal energy they used the models of a harmonic oscillator and of a spherical top.

In this case the vibrational and the rotational energies are

$$E_V = \sum_{i=1}^{S} E_i \tag{3.3.2}$$

$$E_i = \left(v_i + \frac{1}{2}\right)\omega_i \tag{3.3.3}$$

$$E_R(J) = J(J+1)B \tag{3.3.4}$$

Here E_i is the energy of one of the vibrational degrees of freedom, ω_i – the frequency of this vibration, v_i – the vibrational quantum number, S – the number of vibrational degrees of freedom and B is the rotational constant of the spherical top. The degeneracy of the rovibrational state for this model is $(2J+1)^2$. The model of a symmetric oblate top used in the present work gives another formula of the rotational energy

$$E_R(J,K) = J(J+1)B + (C-B)K^2, \tag{3.3.5}$$

where B and C are the rotational constants of the oblate top ($C < B$). K = J, J-1, … 0, -1, … -J is the quantum number of the angular momentum projection onto the symmetry axis of the molecule. In comparison to the case of the spherical top, the K degeneracy of the rotational states of the oblate top is partially reduced. However, the states with $K\neq0$ are still two-fold degenerate, because the energy does not depend on the sign of K. Taking into account the magnetic quantum number degeneracy, the complete degeneracy factor of such states is equal to 2(2J+1). The complete degeneracy factor of the state with K=0 is 2J+1. Therefore the denominator D in Equation (3.3.1) can be written as:

$$D = \sum_{v_1-v_s}\sum_J (2J+1)(E-E_v-E_R)^{\frac{1}{2}} + \sum_{v_1-v_s}\sum_J\sum_{K=1}^{J} 2(2J+1)(E-E_v-E_R)^{\frac{1}{2}} \tag{3.3.6}$$

The second term describes the contribution of the state with $K\neq0$, while the first one describes the contribution of the states with K=0. This expression (3.3.6) can be modified to:

$$D = \sum_{v_1-v_s}\sum_J\sum_{K=0}^{J} 2(2J+1)(E-E_v-E_R)^{\frac{1}{2}} - \sum_{v_1-v_s}\sum_J (2J+1)(E-E_v-E_R)^{\frac{1}{2}} \tag{3.3.7}$$

One can show that the second term is negligible in comparison to the first one. As a result finally the denominator can be approximated by:

$$D = \sum_{v_1-v_s}\sum_J\sum_{K=0}^{J} 2(2J+1)(E-E_v-E_R)^{\frac{1}{2}} \tag{3.3.8}$$

On the next step the summation is replaced by the integration over the energies of all the internal degrees of freedom, which is usually justified when the excess energy is higher than the energy spacing between neighboring quantum states.

$$D = \int_{E_{1=0}}^{E} \dots \int_{E_s}^{E-E_1-\dots-E_s} \int_{E_R=0}^{E-E_V} 2(2J+1)(E-E_V-E_R)^{\frac{1}{2}} dE_R \prod_{i=1}^{S} dE_I \tag{3.3.9}$$

After integration one receives:

$$D = \frac{1}{B\sqrt{B-C}\prod_{i=1}^{S}\omega_i}\frac{\pi}{2}\frac{E^{S+2}}{(S+2)!} \tag{3.3.10}$$

As a result the probability density function of Equation (3.3.1) becomes:

$$\rho^0(E_V, E_R; E) = B\sqrt{B-C}\prod_{i=1}^{S}\omega_i\frac{2}{\pi}\frac{(S+2)!}{E^{S+2}}2(2J+1)(E-E_V-E_R)^{\frac{1}{2}} \quad (3.3.11)$$

To simplify the calculation of the probability density function of the concrete degree of freedom, “redundant” variables are used, $f_{df} = E_{df}/E$. Finally the probability density function of the relative translational energy is:

$$\rho^0(f_T) = \frac{2^{S+2}(S+2)!}{\pi\prod_{k=0}^{S-1}(3+2k)}\sqrt{f_T}(1-f_T)^{S+\frac{1}{2}}, \quad (3.3.12)$$

where $f_T = 1 - f_V - f_R$.

This expression can be rewritten in terms of the speed of the atomic product motion:

$$\rho^0(v) = \frac{2^{S+2}(S+2)!}{\pi\prod_{k=0}^{S-1}(3+2k)}\sqrt{\frac{m}{2E}}\frac{m}{E}v^2\left(1-\frac{m}{2E}v^2\right)^{S+\frac{1}{2}} \quad (3.3.13)$$

Here m is the mass of the atom, v is the speed of the atom.

This approach can be facilitated considering the experimental conditions. The temperature of the molecular beam used in the experiment is low enough to “freeze” the rotational degrees of freedom of a parent borazine molecule. On this basis and because of the total angular momentum conservation the total angular momentum available to the products is limited to values close to zero. On the other side the total angular momentum is the sum of the angular momentum of the borazinyl radical **J** and the angular momentum of the relative motion **L**. Because of zero total angular momentum **J** must be antiparallel and equal in magnitude to **L**, which makes from 2J+1 possible projections of **J** onto **L** only one is allowed. The orbital angular momentum of relative motion **L** is defined by the recoil velocities. These velocities are specified by the polarization vector of the dissociative radiation defining a particular direction in the fixed laboratory frame. This fact eliminates a factor of (2J+1) in the effective degeneracy of the rotational states. Muckerman et al. used these ideas to develop the probability density functions in case of the dissociation into an atom and a spherical top. In our case, i.e. the dissociation into an atom and an oblate symmetric top, one can modify the formula (3.3.8):

$$D = \sum_{v_1-v_s}\sum_J\sum_K 2(E-E_v-E_R)^{\frac{1}{2}} \quad (3.3.14)$$

Then the probability density functions for translational motion are:

$$\rho^0(f_T) = \frac{\prod_{k=0}^{S}(3+2k)}{2^{S+1}S!}\sqrt{f_T}(1-f_T)^S \quad (3.3.15)$$

$$\rho^0(v) = \frac{\prod_{k=0}^{S}(3+2k)}{2^{S+1}S!}\sqrt{\frac{m}{2E}}v^2\frac{m}{E}\left(1-\frac{m}{2E}v^2\right)^S \quad (3.3.16)$$

The obtained formulae are almost universal. Because they do not include the rotational constants of borazinyl radical or any other of its internal characteristics, they can characterize almost any dissociation process with the production of an atom of mass m and of a symmetric top having S vibrational degrees of freedom. The energy E is the only parameter, which describes this particular process of photodissociation.

The modification of the probability density function with the reduction of the number of vibrational degrees of freedom (S) is shown in Fig. 3.3.1. The maximum of the curve moves in the region of higher speeds with the decrease of S and the width of the function increases.

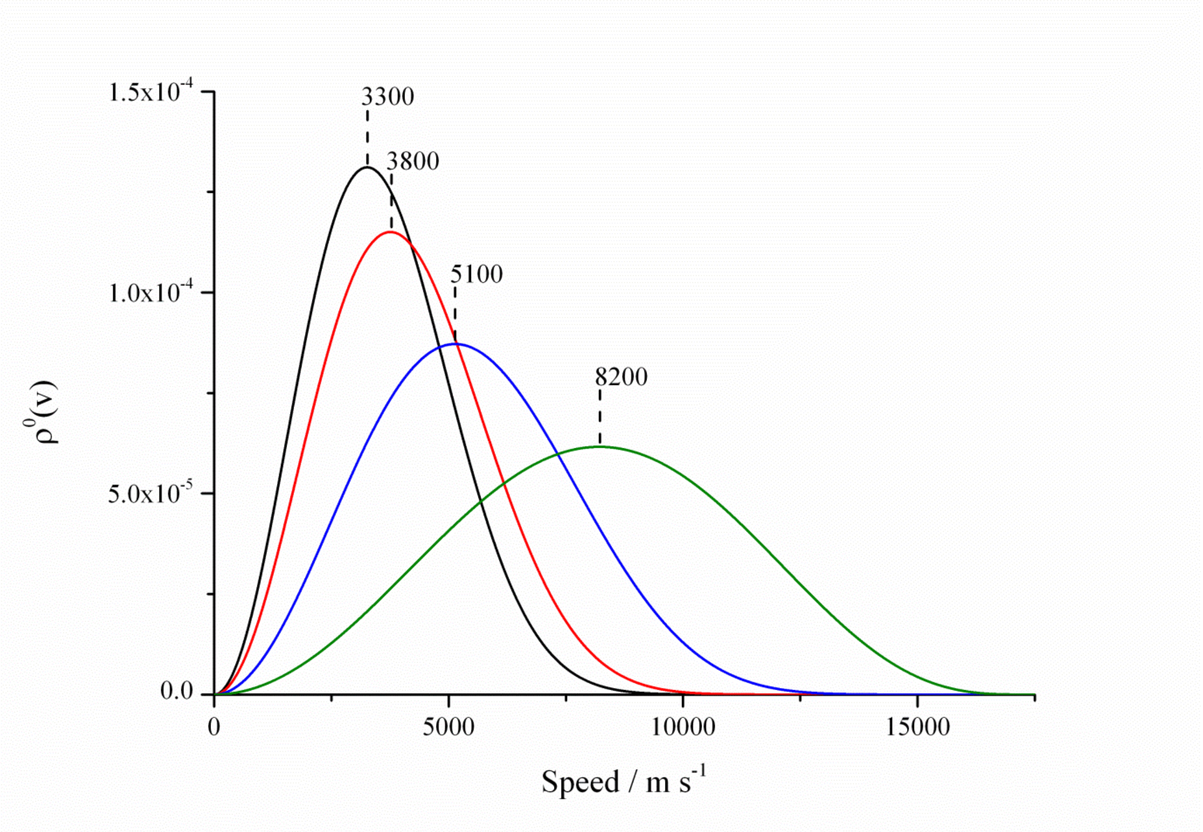

FIG 3.3.1: Probability density function calculated for different number of vibrational degrees of freedom, available in the borazinyl radical after dissociation of borazine molecule:
S = 27 – black curve, S = 20 – red curve, S = 10 – blue curve, S = 3 – green curve.

The influence of the total angular momentum conservation approach on the probability density function for the atomic speed is presented in Fig. 3.3.2.

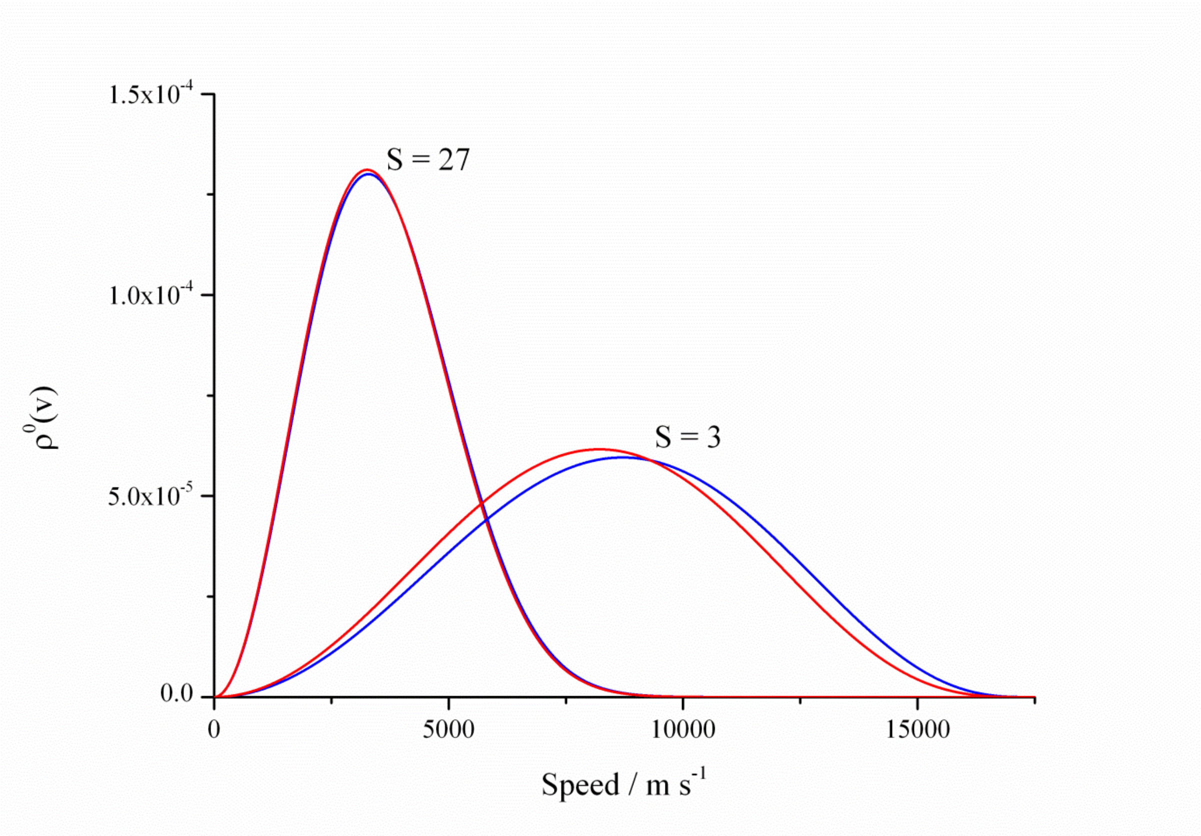

FIG. 3.3.2: Representation of the influence of the total angular momentum approach on the probability density function calculated for two numbers of vibrational degrees of freedom, available in the borazinyl radical after dissociation of borazine molecule (S = 27 or 3). The red curve represents the probability density function calculated without angular momentum conservation (given by Eq. 14), while the blue curve shows the probability density function calculated in the angular momentum conservation approach (given by Eq. 17).

The difference in the functions is negligible for a large numbers of vibrational degrees of freedom, while for small numbers the maximum of the function is shifted towards the higher speed in case of total angular momentum conservation.

3.4 Experimental results

The three-dimensional distribution of the recoil velocity vector of the H atoms is almost isotropic. Its meridian projection [35] as well as the speed distribution are illustrated in Fig. 3.4.1.

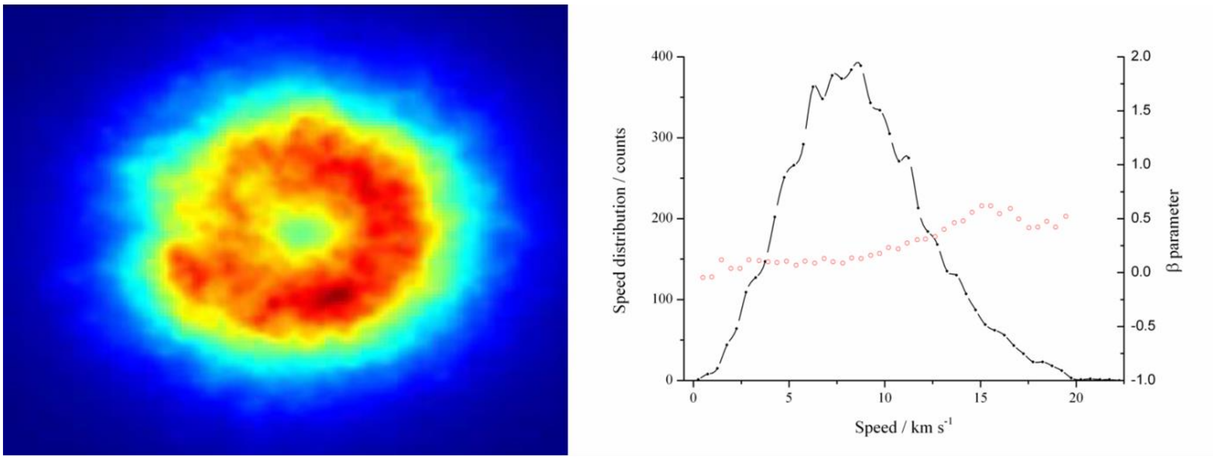

(a) (b)

FIG. 3.4.1: a: Density map of the meridian plot (see ref. 35) of the H^+ ions emerging from the photodissociation of borazine.
b: Speed distribution (black line) of the data shown in **a** and the anisotropy parameter β (red line) of the H^+ ion distribution.

The measured anisotropy parameter β is found to be dependent on the H atom speed. In case of H atoms at lower speed it is close to zero ($\beta=0.10\pm0.07$), i.e. the hydrogen atoms are isotropically distributed whereas for high atomic speeds the β parameter increases to 0.50 ± 0.08.

The speed distribution is very broad with a half width at half maximum of 3700 m/s. This half width is not caused by the apparatus function, which was demonstrated by the speed distribution of hydrogen atom produced in the ion-pair photodissociation of HCl [29]. In this case, where the dissociation results in the formation of monoenergetic H^+ and Cl^- ions, the half width of the speed distribution of the protons is approximately 350 m/s. As the products do not have any internal excitation this half width reflects the apparatus function.

Hydrogen atoms can be produced as a result of the dissociation of a N-H as well as of a B-H bond in the borazine molecule. The energetic difference between the dissociation energies of N-H (1.36 eV) and B-H (1.22 eV) bonds is relatively small according to the results of Weiner. For the dissociative radiation of 193 nm (6.41 eV) the energy available for the dissociation products is 5.05 eV and 5.19 eV. With the assumption, that no internal degrees of freedom of the products are excited, the available energy will entirely be transferred into the kinetic energy of the products (as it was in the case of ion-pair photodissociation of HCl). Since the $B_3N_3H_5$ radical product is much heavier as hydrogen atom, almost the whole available energy will be transferred in the kinetic energy of hydrogen atom, with corresponding speeds of the H atom of 31220 m/s and 31650 m/s for N-H and B-H bond cleavage. However in the experimentally observed speed distribution the number of particles with speeds above 21750 m/s is negligible.

Therefore the maximum hydrogen kinetic energy is 2.45 eV corresponding to a dissociation energy of about 3.96 eV. This experimental value of dissociation energy is significantly larger than the energies calculated by Weiner.

The experimental speed distribution gives the most probable speed equal to about 8250 m/s. This observation demands that internal excitation of radical product has to be considered. The large half-width of the experimental distribution shows that a wide range of internal energy is available for radical. Because of the large number of internal degrees of freedom in the radical, we have to rationalize the experimental information with the theoretical treatment to explain how the internal energy is distributed over the internal degrees of freedom.

3.5 Theoretical results

Ab initio calculations were performed for the borazine molecule as well as for both possible borazinyl radicals emerging from photodissociation. They give planar structure of both radicals with the symmetry D_{2h}. Calculated dissociation energies and rotational constants are summarized in the Table I. The dissociation energies for both radicals are significantly larger than those calculated by Weiner and slightly larger than our experimental values. According to these data the available energy after photodissociation is smaller in comparison to experimental results.

Radical	Dissociation energy, eV		Rotational constants, cm^{-1}		
	Our work	Ref 27	A	B	C
N-borazinyl	5.21	1.36	0.19238	0.16915	0.09001
B-borazinyl	4.86	1.23	0.18856	0.17127	0.08975

TABLE I: Results of ab initio calculations. Calculation method UB97D.

The rotational constants for both radicals demonstrate that the radicals are asymmetric tops. However two constants are close to one another and significantly larger than the third one. Thus, it is justified to apply the model of oblate symmetric top.

These results allow us to build the speed probability density functions in case of borazine fragmentation according to the model described above in Chapter IIIb. The conditions in a molecular beam justify one to use the approach of total angular momentum close to zero. In the formulae (Chapter IIIb) the probability density is a function of relative energies, i.e. the ratio of the energy of a degree of freedom to the energy available after photodissociation. The available energy has to be determined precisely. In this work we find this energy in two ways: experimentally and theoretically.

The probability density function (Eq. 3.3.16) for the hydrogen translational motion with the condition, that all 27 vibrations of borazinyl radical are available, is presented in Fig 3.3.1. The most probable speed is around 3300 m/s. This result does not agree with the experimental data, where the most probable speed of hydrogen atoms was found to be equal to 8250 m/s. Thus, dynamical processes must restrict the distribution of energy

The variation of the number of activated vibrations and as a result the modification of the speed probability density function allows to achieve a significantly improved agreement of this theoretical function (theoretical speed distribution) with the experiment. For two theoretical energies available after photodissociation following from the results of ab initio calculation the agreement is reached for two activated vibrations of N-borazinyl radical and three activated vibrations B-borazinyl radical. The agreement is possible also in the mixed case, where both photodissociation channels are present and in both radicals two vibrations are activated. The corresponding distributions are shown in Fig. 3.5.1.

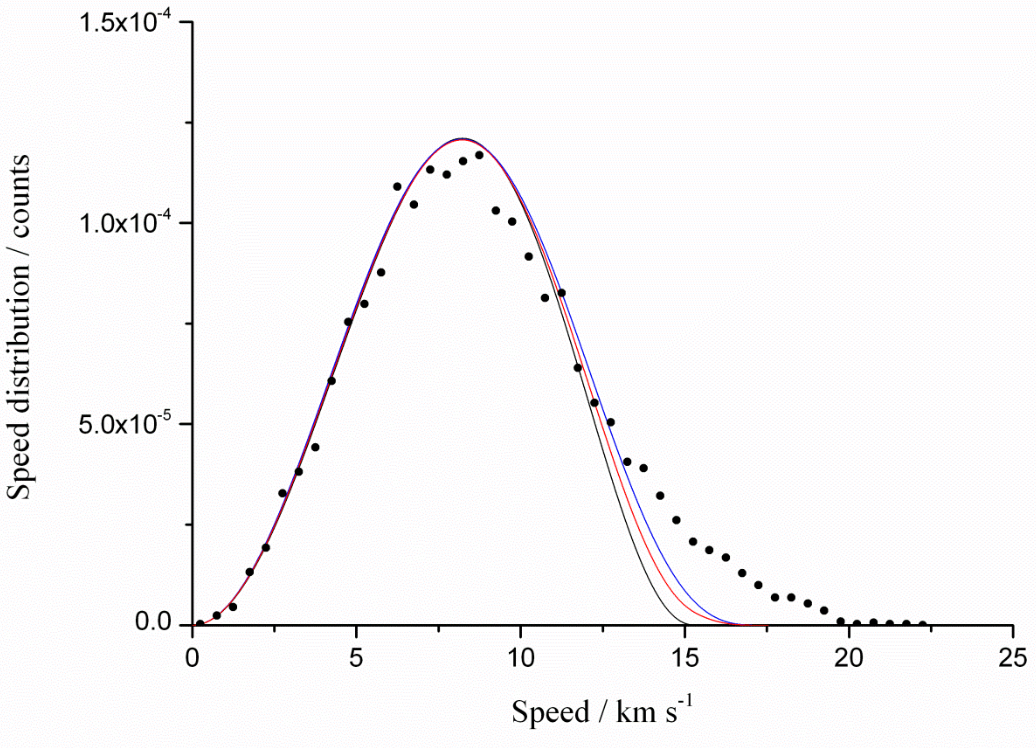

FIG. 3.5.1: Comparison of experimentally measured speed distribution (black dots) with the theoretical probability density functions calculated in case of only N-borazinyl production (black curve), only B-borazinyl production (blue line) or both radical production (red curve).

3.6 Discussion

Previous studies of borazine have shown that its absorption spectrum lies in the spectral region shorter than 200 nm. It can be attributed to at least three allowed electronic transition: $\tilde{C}^1E' \leftarrow \tilde{X}^1A_1'$ (165 nm); $\tilde{B}^1B^1A_1' \leftarrow \tilde{X}^1A_1'$ (188.9 nm); and $\tilde{A}^1A_2' \leftarrow \tilde{X}^1A_1'$ (197.5 nm) [18,19]. 193 nm radiation most likely induces the $\tilde{A}^1A_2' \leftarrow \tilde{X}^1A_1'$ electronic transition. The ground electronic state with the symmetry A_1' is characterized by a wavefunction being symmetric with respect to reflection at the σ_v plane perpendicular to plane σ_h, while the excited electronic state wavefunction, A_2' symmetry, is asymmetric with respect to reflection at the σ_v plane. Both wavefunctions are symmetric with respect to reflection on the σ_h plane. On this basis one can conclude that the transition dipole moment lies in the plane of the borazine molecule and is oriented perpendicular to the B-H or N-H bond (Fig. 3.6.1).

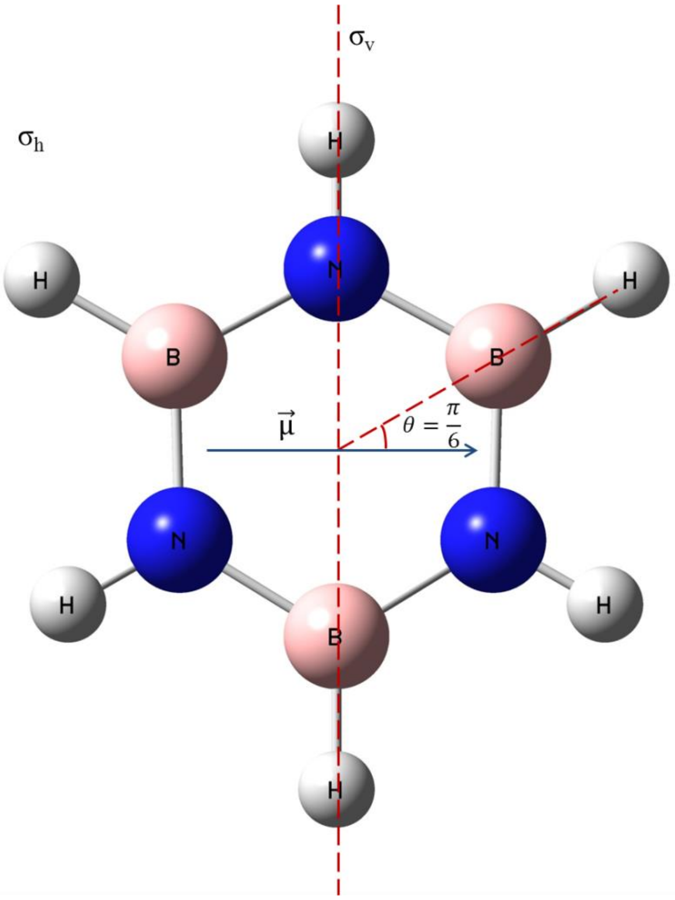

FIG. 3.6.1: The borazine molecule and the dipole moment $\vec{\mu}$ of the transition $\tilde{A}^1A_2' \leftarrow \tilde{X}^1A_1'$. The wavefunctions of the electronic states A_1' and A_2' are symmetric in relation to the reflection at the σ_h plane. The ground state A_1' wavefunction is symmetric in relation to the reflection at the σ_V plane, while the wavefunction of the excited state A_2' is antisymmetric.

The direction of the transition dipole moment in the molecular frame defines the β-parameter of anisotropy according to the formula

$$\beta = 2P_2(\cos(\theta_{\mu v})), \tag{3.6.1}$$

where $\theta_{\mu v}$ denotes the polar angle between the recoil direction of the fragments and the transition dipole moment. $P_2(\cos(\theta_{\mu v}))$ is the second Legendre polynomial.

3.6.1 Slow hydrogen atoms

No hypothetical direct process of photodissociation of N-H or B-H bonds in borazine can result in a β-parameter close to zero (β=0.10±0.07), which was observed at hydrogen product speeds below 10 km/s. However, as it was presented by Busch and Wilson [36], the details of the photodissociation dynamics such as parent molecule internal motion (vibration or rotation) and the lifetime of the parent molecule before breaking apart can make the angular distribution of the products almost isotropic with a β-parameter close to zero. The mentioned aspects are typical for predissociation of molecules. Therefore the observed broad distribution for product atoms below 10 km/s is attributed to a predissociation of the borazine molecule. This result agrees with the conclusions of Weiner et al. who also reported the observation of electronic predissociation, due to coupling between excited electronic states.

The shape of the speed distribution does not allow to discriminate between B-H or N-H bond breaking. However, from the observed shape one can conclude that in case of the presence of both fragmentation channels the energy must be distributed in a similar way among the translational motion of the H atom and the internal degrees of freedom of the borazinyl radical. In view of the small difference between the dissociation energies calculated for B-borazinyl and N-borazinyl formation one arrives at two very similar speed distributions characterizing these channels with widths almost equal to the experimentally measured one. The difference in the most probable speeds of both distributions can be evaluated from the difference in energy release in both cases.

The best agreement of the theoretical speed distribution with the experimental one is achieved when both predissociation channels exist. In this case two vibrational modes are activated in the N-borazinyl radical and three modes in the B-borazinyl radical. Following the assignments of Bernstein and Reilly [19], Weiner et al. concluded that 193 nm radiation (51813 cm^{-1}) of $B_3N_3H_6$ may directly excite the $\tilde{A}^1A_2', 4^1 10^1 \leftarrow \tilde{X}^1A_1', 0^0$ vibronic transition (51840 cm^{-1}). It is highly likely that these two vibrational modes (υ_4 and υ_{10}) will be excited in the radicals as well.

A similarly good agreement between the experimental and theoretical speed distribution can also be achieved for the predissociation with the breaking of only one type of bond. The number of activated modes then depends on the type of the breaking bond. If one assumes the dissociation of the N-H bond, two modes must be activated in the N-borazinyl radical, while in case of B-H dissociation one has to take into account an additional third mode.

To understand which mode of vibration is the most probable one to be activated in the borazinyl radical after photodissociation in addition to the modes activated in the parent molecule, it is sufficient to imagine the motion of atoms in the radical. The velocity of produced hydrogen atoms after photodissociation is preferentially oriented along the symmetry axis of borazinyl radical. When H atom formation is the result of a B-H bond dissociation, it is implied that the motion of the B atom starts in the radical plane. As a result those vibrational degrees of freedom, which contain the motion of the boron atom along the radical axis of symmetry can be excited. In other words it will be the bending vibrations with the deformation of NBN angles. The ab initio calculation of the vibrational motion yielded in both cases five bending vibrations of such kind.

3.6.2 Fast hydrogen atoms

The β-parameter is found to be speed dependent and increases from 0.10±0.07 at slow and intermediate speeds to 0.50±0.08 for large speeds, where the speed corresponds to the total energy release. This can be explained by a direct hydrogen atom recoil from the photoexcited borazine molecule. In case of this direct process the value of β-parameter is not significantly affected by additional motions of the excited parent molecule and represents essentially the relative orientation of the transition dipole moment with respect to the recoil velocity. The transition dipole moment, characterizing the excitation of borazine molecule after the absorption of one photon of 193 nm, is perpendicular to the σ_v plane of symmetry of the molecule. The dissociation of all three B-H or N-H bonds is a priori equally probable. The final speed distribution is an average of the contributions from the dissociation of each bond. It is characterized by an average β-parameter

$$\beta = \frac{1}{3}\left(2P_2\left(\cos\left(\frac{\pi}{2}\right)\right) + 2 \cdot 2P_2\left(\cos\left(\frac{\pi}{6}\right)\right)\right) = 0.5 \qquad (3.6.2)$$

if the dissociation of only one type of bond occurs. The β-parameter when both types of bond contribute to the dissociation it is the result of another averaging process. Because of the symmetry of borazine is described by the same molecule and has the same value 0.5. However, the dissociation energies obtained from ab initio calculations imply that the process of direct B-H bond dissociation is more likely than that of a N-H bond break.

Fig 4 shows that the contribution of direct dissociation is relatively small. Thus the process of direct dissociation is much less effective than the process of predissociation. Therefore, methods less sensitive than Ion Imaging can not detect the direct dissociation process. Most likely this is why this channel has not been described previously.

3.7 Conclusion

In the present study we have applied the 3D velocity map imaging method to study the 193 nm photodissociation of borazine with formation of a hydrogen atom and a borazinyl radical. The 3D velocity vector distribution of H atoms was registered and found to be isotropic for low recoil velocities. However, the anisotropy β-parameter is speed dependent above 10 km/s, starting at 0.1±0.07 and increases to 0.5±0.08 at large speeds. This indicates two channels of hydrogen atom production. These channels correspond to predissociation and direct dissociation of the borazine molecule.

The predissociation is characterized by a very broad speed distribution peaking at 8250 m/s with half width at half maximum of 3700 m/s, which is much less than a complete energy release in translation. The remaining energy is released as internal energy of the borazinyl radical. To understand how this transferred energy is distributed over the internal degrees of freedom of the borazinyl radical, a phase space calculation was performed. Theoretical distributions obtained for both cases of N- and B-borazinyl radical formation agree well with the experimental speed distribution with two (N-borazinyl) and three (B-borazinyl) activated vibrational modes. The formation of only one radical type is possible as well. Two activated modes correspond to the vibrational modes of the borazine parent molecule as a result of vibronic transition $\tilde{A}^1A_2', 4^1 10^1 \leftarrow \tilde{X}^1A_1', 0^0$.

The direct dissociation results in the formation of hydrogen atoms with speeds close to the maximum energy release. The β-parameter equal to 0.5±0.08 demonstrates that the transition dipole moment is situated in σ_h symmetry plane of the molecule and is oriented perpendicular to one of the σ_v plane. This can be achieved in case of a $A_2' \leftarrow A_1'$ dissociative transition. Ab initio calculations show that a B-H bond break is more probable for direct dissociation. The contribution of the direct dissociation in the final speed distribution is significantly smaller than the contribution of predissociation.

3.8 References

---

[1] A. Stock, E. Pohland, Ber. Dtsch. Chem. Ges. **59**, 2215 (1926).

[2] S. H. Bauer, Journ. Amer. Chem. Soc. **60**, 524 (1938).

[3] E. Wiberg, A. Bolz, Ber. Dtsch. Chem. Ges. **73**, 209 (1940).

[4] R. K. Bartlett, W. S. McDonald, H. S. Turner, R. J. Warne, M. A. Young, New Scientist **247**, 355 (1961).

[5] R. T. Paine, L. G. Sneddon, Chemtech **24**, 29 (1994).

[6] F. Cao, Y. Ding, L. Chen, C. Chen, Z. Fang, Materials and Design **54**, 610 (2014).

[7] J. Eichler, C. Lesniak, Journal of the European Ceramic Society **28**, 1105 (2008).

[8] B. Hwang, J. Kwon, M. Lee, S. J. Lim, S. Jeon, S. Kim, U. Ham, Y. J. Song, Y. Kuk, Current Applied Physics **13**, 1365 (2013).

[9] S. Kervyn, N. Kalachnyk, M. Riello, B. Moreton, J. Tasseroul, J. Wouters, T. S. Jones, A. De Vita, G. Constantini, D. Bonifazi, Angew. Chem. Int. Ed. **52**, 7410 (2013).

[10] B. L. Crawford, J. T. Edsall, J. Chem. Phys. **7**, 223 (1939).

[11] R. F. Porter, E. S. Yeung, Inorg. Chem. **7**, 1306 (1968).

[12] K. Niedenzu, W. Sawodny, H. Watanabe, J. W. Dawson, T. Totani, W. Weber, Inorg. Chem. **6**, 1453 (1967).

[13] V. B. Kartha, S. L. N. G. Krishnamachari, C. R. Subramanlam, Journal of Molecular Spectroscopy **23**, 149 (1967).

[14] E. Silberman, Spectrochimica Acta **23A**, 2021 (1967).

[15] J. Huober, M. Pfeffer, A. Ruoff, Z. Anorg, Allg. Chem. **627**, 589 (2001).

[16] L. R. Platt, H. B. Klevens, G. W. Schaeffer, J. Chem. Phys. **15**, 598 (1947).

[17] C. W. Rector, G. W. Schaeffer, J. R. Platt, J. Chem. Phys. **17**, 460 (1949).

[18] A. Kaldor, J. Chem. Phys. **55**, 4641 (1971).

[19] E. R. Bernstein, J. P. Reilly, J. Chem. Phys. **57**, 3960 (1972).

[20] H. Bock, W. Fu, Angew. Chem. **83**, 169 (1971).

[21] J. P. Doering, A. Gedanken, A. P. Hitchcock, P. Fischer, J. Moore, J. K. Olthoff, J. Tossell, K. Raghavachari, M. B. Robin, J. Am. Chem. Soc. **108**, 3603 (1986).

[22] M. B. Robin, N. A. Kuebler, J. Mol. Spec. **70**, 472 (1978).

[23] M. P. Nadler, R. F. Porter, Inorg. Chem. **8**, 599 (1969).

[24] D. C. Frost, F. G. Herring, C. A. McDowell, I. A. Stenhouse, Chemical Physics Letters **5**, 291 (1970).

[25] J. Kroner, D. Proch, W. Fuss, H. Bock, Tetrahedron **28**, 1585 (1972).

[26] M. A. Neiss, R. F. Porter, Journal of the American Chemical Society **94**, 1438 (1972).

[27] D. Huang, A. Hidalgo, V. I. Makarov, G. Morell, B. R. Weiner, Chem. Phys. Lett. **509**, 108 (2011).

[28] A. Chichinin, T. Einfeld, C. Maul, and K.-H. Gericke, Rev. Sci. Instr. **73**, 1856 (2002).

[29] S. Kauczok, N. Gödecke, A. I. Chichinin, M. Veckenstedt, C. Maul, and K.-H. Gericke, Rev. Sci, Instr. **80**, 083301 (2009).

[30] A. I. Chichinin, S. Kauczok, K.-H. Gericke, and C. Maul, Int. Rev. Phys. Chem **28**, 607 (2009).

[31] I. Ali, R Dörner, O. Jagutzki, S. Nüttgens, V. Mergel, L. Spielberger, K. Khayyat, T. Vogt, and H. Bräuning, Nucl. Instrum. Methods Phys. Res. B **149**, 490 (1999).

[32] O. Jagutzki, V. Mergel, K. Ullmann-Pfleger, L. Spielberger, U. Spillmann, R. Dörner, H. Schmidt-Böcking, Nucl. Instrum. Methods Phys. Res. B, **477**, 244 (2002).

[33] Gaussian 09, Revision A.02, M. J. Frisch, G. W. Trucks, H. B. Schlegel, G. E. Scuseria, M. A. Robb, J. R. Cheeseman, G. Scalmani, V. Barone, B. Mennucci, G. A. Petersson, H. Nakatsuji, M. Caricato, X. Li, H. P. Hratchian, A. F. Izmaylov, J. Bloino, G. Zheng, J. L. Sonnenberg, M. Hada, M. Ehara, K. Toyota, R. Fukuda, J. Hasegawa, M. Ishida, T. Nakajima, Y. Honda, O. Kitao, H. Nakai, T. Vreven, J. A. Montgomery, Jr., J. E. Peralta, F. Ogliaro, M. Bearpark, J. J. Heyd, E. Brothers, K. N. Kudin, V. N. Staroverov, R. Kobayashi, J. Normand, K. Raghavachari, A. Rendell, J. C. Burant, S. S. Iyengar, J. Tomasi, M. Cossi, N. Rega, J. M. Millam, M. Klene, J. E. Knox, J. B. Cross, V. Bakken, C. Adamo, J. Jaramillo, R. Gomperts, R. E. Stratmann, O. Yazyev, A. J. Austin, R. Cammi, C. Pomelli, J. W. Ochterski, R. L. Martin, K. Morokuma, V. G. Zakrzewski,

---

G. A. Voth, P. Salvador, J. J. Dannenberg, S. Dapprich, A. D. Daniels, O. Farkas, J. B. Foresman, J. V. Ortiz, J. Cioslowski, and D. J. Fox, Gaussian, Inc., Wallingford CT, 2009.

[34] J. T. Muckerman, J. Phys. Chem. **93**, 179 (1989).

[35] A. I. Chichinin, C. Maul, and K.-H. Gericke, J. Chem. Phys. **124**, 224324 (2006).

[36] G. E. Busch, K. N. Wilson, J. Chem. Phys. **56**, 3638 (1972).

4 Simultaneous imaging of both product ions: Exploring gateway states for HCl as benchmark molecule

Abstract: Simultaneous imaging of both positive and negative product ions is used to exclusively study photoion pair formation free from interference of competing fragmentation channels. Resonance enhanced multi-photon excitation allows us to interrogate potential energy surfaces for vastly differing molecular geometries. 3D imaging provides complete fragment information. We applied the technique to HCl as benchmark and identified the gateway state leading to photoion pairs. The approach can easily be applied to any molecule exhibiting a potential with an attractive part at large internuclear distances.

Complete characterization of elementary chemical processes is a major challenge in reaction dynamics. Ideally, it would require determination of the fully quantum state resolved joint reaction probability for product pairs coincidently formed in the same elementary process. However, true coincidence measurements for chemical reactions are extremely difficult to realize, and lifting the requirement for observed products to result from the same elementary process, the next best strategy is the fully quantum state resolved simultaneous observation of all product species formed in the process under investigation. In this context, ion pair production is particularly interesting. It is one of several competing processes occurring in many molecules and has been studied for ground state geometries by photoexcitation in the vacuum ultraviolet (VUV). Based on these studies, we report a novel technique of resonance enhanced multi-photon excitation relying on readily available UV light in conjunction with three-dimensional (3D) imaging for simultaneously monitoring of both oppositely charged ionic products. Thus we can interrogate a wide range of molecular geometries, exclusively address the photoion pair channel in a complex environment of competing processes, and simultaneously observe both products. 3D fragment momentum vector distributions are determined containing complete photofragment information, subsets of which are conventional quantities as kinetic energy distributions, spatial fragment distributions, and anisotropy parameters. We demonstrate power and potential of our method for HCl fragmentation as prototype because its fragmentation and ionization dynamics have intensively been studied and the energy partitioned onto the ionic fragments is discrete and fixed by conservation of energy and linear momentum. From our data, the existence of a Rydberg gateway state on the route to photoion pair generation in HCl is verified. Experimental approach and excitation scheme are easily applicable to any molecule exhibiting potential energy surfaces with attractive parts at large internuclear distances, paving the way for determining joint reaction probabilities of coincidently formed products.

Photodissociating neutral molecules AB either produces neutral fragments A + B or oppositely charged ionic species $A^+ + B^-$, as was first observed in 1932 [1]. Today over 50 molecules are known to fragment into ionic pairs upon photoabsorption. Numerous studies were performed employing vacuum ultraviolet (VUV) single photon absorption [2,3], nevertheless, the issue of whether the formation mechanism is a direct transition from the ground state into the ion pair state or rather a Rydberg state excitation followed by a non adiabatic transition to the ion pair state is still being discussed controversially [4,5].

Long range Coulomb attraction between oppositely charged ionic fragments is reflected by shallow slopes of ion pair state potential energy surfaces, and noticeable attractive forces act at large inter-nuclear distances. In contrast, potential energy surfaces of valence states correlating to neutral fragments are characterized by steep slopes at small inter-nuclear distances with significant interaction not extending beyond a few hundred picometers. The energetically lowest ion pair states result from excitation within the valence electron shell. Therefore ion pair states represent a sub-class of valence states. However, ion pair states result from "high energy" excitation within the valence shell and often exhibit similar energies as Rydberg states which result from electronic excitation "outside" the valence shell. High energies and long range attractions of ion pair states make result in numerous avoided crossings between ion pair and Rydberg states of identical symmetry, yielding several double minima potential energy surfaces with quite peculiar dissociation and/or ionization dynamics. As an example, we recently reviewed the intriguing dynamics evolving on an (incomplete) set of HCl Rydberg, valence, and ion pair potentials [6].

Shedding light on these complex dynamics is challenging and requires obtaining as much information about a fragmentation process as possible. Ideally, one should monitor all fragments simultaneously or, rather, in coincidence. Also, one should obtain as much information about each single fragment as possible, i.e. one should monitor each fragment's quantum state and three-dimensional momentum vector. Three-dimensional (3D) imaging techniques with the time-resolving delay line anode detector are at hand nowadays that can provide the desired complete data for a single laser shot excitation [7-9] or by superposition of sequentially obtained slices. [10,11] From the experimental observables, common quantities as e.g. kinetic energy distributions, quantum state populations and spatial anisotropies for particle ensembles are easily obtained by suitable averaging and/or projection.

To this end three-dimensional imaging is combined with resonance enhanced multi-photon ionization. Tuning the resonant excitation laser lets one address single quantum levels of an electronic state (IS_1) under investigation while another photon (or several photons) subsequently interrogates the selected state yielding detectable fragments.

$$AB \xrightarrow{n h\nu} AB^*(IS_1) \quad \xrightarrow{h\nu} AB^+ \tag{4.1a}$$

$$\xrightarrow{h\nu} A + B^* \tag{4.1b}$$

$$\xrightarrow{h\nu} A^* + B \tag{4.1c}$$

$$\xrightarrow{h\nu} A^+ + B^- \tag{4.1d}$$

$$\xrightarrow{h\nu} \ldots \tag{4.1e}$$

In conventional VUV photoion pair studies (4.1d) AB is directly transformed into the ionic pair $A^+ + B^-$ by a single photon without passing through an intermediate state IS_1. Necessarily, in such experiments the explorable molecular geometry is limited to Franck-Condon regions. In contrast, for multiphoton experiments the explorable range of internuclear distances is dramatically extended by carefully choosing appropriate target intermediate states IS_1, as the aforementioned double minima states. Owing to the pronounced non-diagonal character of the Franck-Condon factors associated with shallow double minima states, large sets of vibrational quantum numbers can be scanned and relevant portions of the potential energy surfaces are almost selectable at will. Several such studies were performed by monitoring positive fragment ions, yielding a wealth of information on the dynamics evolving on high-energy intermediate electronic states [12-22]. However, often ion pair formation, not being the dominant fragmentation channel, is hidden under much stronger positive ion signals resulting from ionization of initially neutral fragments or from fragmentation of molecular ions. Therefore information about the ion pair channel remained scarce in such experiments. In contrast, simultaneous detection of both positive and negative ionic fragments offers unequivocal evidence of the ion pair channel and provides interference-free information about it.

The scope of this letter is to present simultaneous 3D photoion pair imaging as experimental method for detailed studying of intramolecular excitation dynamics among Rydberg and ion-pair moieties of highly excited electronic states of small molecules with focusing on coincident ion pair formation. Data analysis strategies are presented and implications are discussed for the example of ionization and fragmentation of the HCl molecule following a specific vibrational excitation of its double minimum $B^1\Sigma^+$ state. Experimental approach and data analysis can be transferred to any molecule exhibiting suitable ion pair potential energy. A much wider range of the relevant potential energy surfaces can be examined than with conventional one-photon VUV absorption. Simultaneous detection of both anionic and cationic species in ion pair production makes use of the previously demonstrated analytic power of resonance enhanced multi photon imaging letting oneexplore regions of potential energy surfaces inaccessible for conventional techniques.

The 3D imaging experimental setup has been described in detail elsewhere [8,9]. We modified our setup with a second time-of-flight (TOF) detector such that both positive and negative ions can be observed, both separately and simultaneously. The second detector is currently being upgraded to a full 3D detector. The improved set-up differs from former versions primarily by the presence of two TOF spectrometers, each equipped with its own detector. The two spectrometers share the symmetry axis (see Fig. 4.1) and are the mirror reflection of one another. A pulsed nozzle generated a molecular beam of the precursor substance between the two spectrometers perpendicular to their symmetry axis. For the data presented here the nozzle was operated with pure HCl. The molecular beam was intersected by one laser beam propagating perpendicularly to both the spectrometer symmetry axis and to the molecular beam. Laser radiation at wavelengths around 235 nm was produced by frequency doubling the output of a tunable Nd:YAG laser pumped dye laser and resonantly excited HCl by two-photon absorption at a total energy around 85100 cm^{-1}. A third photon from the same laser fragmented the excited HCl molecule to either neutral or ion pair fragments. For ion pair formation the absorption of a third photon was essential since the ion pair threshold at 1390.9 kJ/mol [23] (or 116255 cm^{-1}). lies far above the two photon energy level. The linear laser polarization could be adjusted between 0° and 90° with respect to the TOF spectrometer axis. Laser beam (X), molecular beam (Y), and spectrometer axis (Z) define the Cartesian coordinate system in the laboratory. Negative ions were registered by a delay line detector (Roentdek DLD-80), after passing one side of the TOF spectrometer. Interference from photoelectrons is avoided by installing permanent magnets providing a homogeneous magnetic field, not influencing the trajectories of heavy chlorine negative ions. Simultaneously, positive ions passed the other side of the spectrometer and were registered by a homebuilt 1D detector (double stage multichannel plate (MCP) assembly + anode). For the time being, three-dimensional images of positive ions were obtained by reversing spectrometer voltages while currently three-dimensionality is being installed in both arms of the spectrometer.

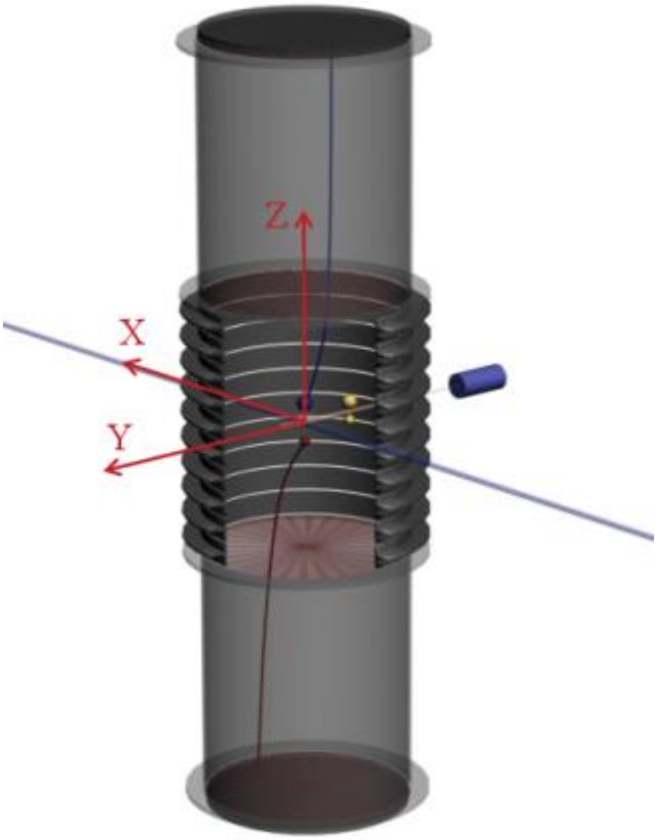

FIG. 4.1: Double arm ion pair three-dimensional (3D) imaging for simultaneous detection of positive and negative photoions.

The complete information about all three components of the velocity vectors of Cl^- and H^+ is directly obtained from the experiment. (Fig. 4.2) Thus, the ion-pair photodissociation channel is directly analyzable from the 3D raw data without need for mathematical reconstruction relying on inversion algorithms as it is necessary for a 2D experiment. However, displaying data in two dimensions requires suitable projection. Here, two kinds of data presentation are used: 1) conventional 2D projection into the XY plane (Fig. 4.2A) corresponding to experimentally observed images in 2D imaging, and 2) meridian projection (Figs. 2B/C) described in detail elsewhere [20]. Mathematical transformations describing the two methods are given in Table I.

	Spherical (r, θ, φ)	Cartesian (x, y, z)
1D TOF	$(r, \theta, \varphi) \rightarrow (r\cos\theta, 0,0)$	$(x, y, z) \rightarrow (0, 0, z)$
2D conventional	$(r, \theta, \varphi) \rightarrow (r\sin\theta, \pi/2, \varphi)$	$(x, y, z) \rightarrow (x, y, 0)$
2D meridian	$(r, \theta, \varphi) \rightarrow (r, \pi/2, \varphi)$	$(x, y, z) \rightarrow (\Gamma x, \Gamma y, 0)$[a]

[a] $\Gamma = \frac{1}{\sin\theta} = \sqrt{\frac{x^2+y^2+z^2}{x^2+y^2}}$

TABLE I: Mathematical representation of projection methods for displaying 3D imaging data, in spherical (r, θ, φ) and Cartesian (x, y, z) coordinates

For comparison, 1D projection onto a single (spectrometer) axis is given corresponding to measured data in TOF spectrometry. Only the r conserving meridian projection copes with the spherical symmetry of the investigated fragmentation process while the other two projection methods rather obey a Cartesian way of thinking unsuited for instructive presentation of experimental 3D imaging data. In any case, one must bear in mind that for a 3D imaging experiment any 2D display projection necessarily goes along with a loss of information, whereas the complete information is always maintained in the original data.

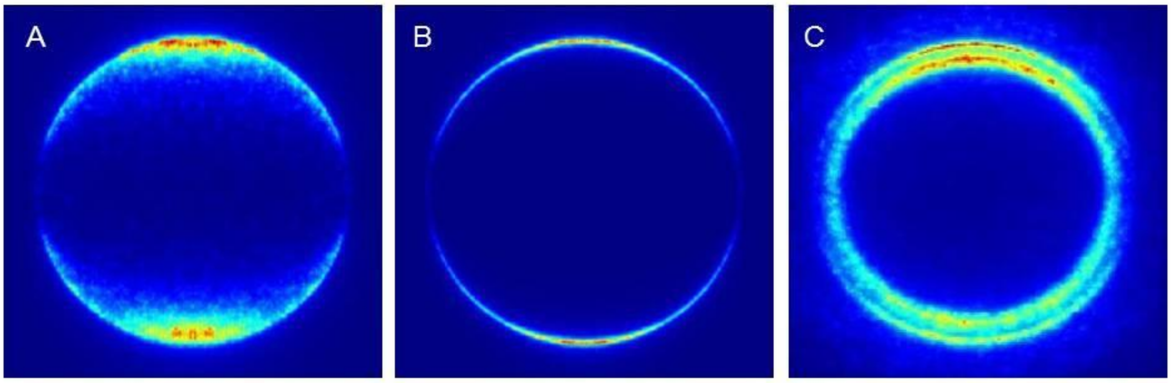

FIG. 4.2: Two-dimensional projections of 3D images for HCl ion pair dissociation via resonant two-photon excitation of the $V^1\Sigma^+$(v=12,J=0) intermediate state. Laser polarization is vertical in all panels.

A Cl^- conventional 2D plot .

B Cl^- meridian 2D plot

C H^+ meridian 2D plot. Only the outer intensive ring results from ion pair dissociation. Other features result from dissociation into neutral, electronically excited fragments which are subsequently photoionized or from photoionization of the parent molecule which is subsequently dissociated.

For informative 2D projections, the plane of projection must contain the electric field vector E. In Fig. 4.2 where $IS_1 = V^1\Sigma^+$(v=12,J=0) the electric field vector E is oriented along the y axis. The full 3D fragment distribution is symmetric about the axis defined by the electric field vector, provided all photons have identical polarization 2D projections of Cl^- (Figs. 4.2A/B) and H^+ ions (Fig. 4.2C) resulting from the multiphoton excitation of HCl demonstrate significant angular anisotropy, with HCl excitation and dissociation being of parallel character, i.e. electric field vector, transition dipole moment of HCl, and fragment recoil direction are all oriented parallel to each other. The parallel mechanism is strictly proved by mathematical analysis of the 3D velocity vector distribution giving a precise result of 2.0 for the β anisotropy parameter in Eq. 4.2:

$$P(\theta_E) \sim 1 + \beta P_2(\cos \theta_E) \tag{4.2}$$

Here, θ_E is the angle between electric field vector of the excitation light and fragment momentum vector and P_2 is the second Legendre polynomial. Speed characteristics of photonegative ions are best obtained from meridian projection [20] of the 3D distribution (Figs. 4.2B/C). For Cl^- meridian projection yields only one ring with a radius corresponding to the most probable speed. In contrast, the H^+ speed distribution exhibits a richer structure resulting from various pathways accessible for production of H^+ upon HCl multi-photon ionization. Only one H^+ ring results from ion pair dissociation, all others are evidence of competing fragmentation channels initially producing neutral, electronically excited fragments subsequently being photoionized or ionized parent molecules subsequently being dissociated. The Cl^- ring is in perfect agreement with the H^+ ion pair ring obtained in this and in previous investigations [6,21], considering linear momentum conservation of an initially resting HCl molecule:

$$p(H^+) + p(Cl^-) = p(HCl) = 0 \tag{4.3}$$

The β parameter for Cl^- in Fig. 4.2B was determined to be 1.92+/-0.12, and the ß parameter for H^+ in the outer intensive ring in Fig. 4.2C is 1.59+/-0.43. Again, both values agree very well with each other within the experimental error. The experimental error in H^+ is slightly larger because 1) the H^+ ion pair signal cannot cleanly be separated from the interfering channels mentioned above, and 2) the fast H^+ ions travel for the most part of their trajectory in the spectrometer far away from the spectrometer axis, such that off-axis inhomogeneities in the electric fields start to become noticeable.

One dimensional representations of both H^+ and Cl^- speed distributions are shown in Fig. 4.3. Speed axes are scaled by the ^{35}Cl to ^{1}H mass ratio of 34.96885/1.00783 [24] accounting for linear momentum conservation. The conservation of linear momentum together with a β parameter of 2 is proof of the ion-pair channel being the only source of negative chlorine ions. This proof is critical because theoretically a different mechanism of negative ion formation were possible: HCl^- decomposition after dissociative photoelectron attachment to HCl [25].

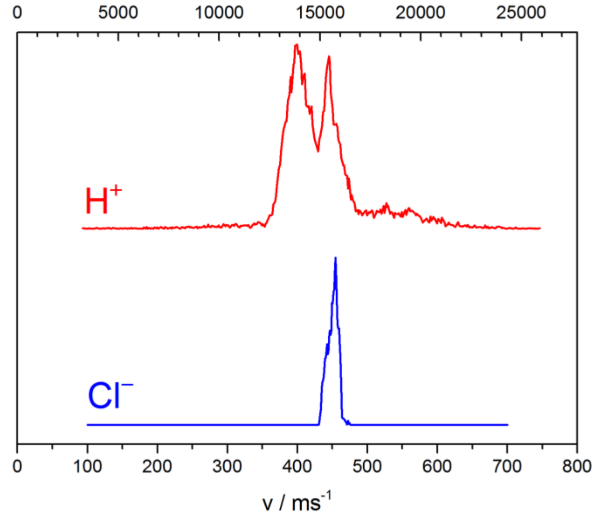

FIG. 4.3: Speed distributions for H^+ and Cl^- photoions obtained after resonant two-photon excitation of the $V^1\Sigma^+$(v=12,J=0) intermediate state of HCl. The horizontal axis is scaled according to fragment masses: Equal positions correspond to equal linear momenta. Only the H^+ peak at 15500 m/s results from ion pair dissociation. Other features result from dissociation into neutral, electronically excited fragments which are subsequently photoionized or from photoionization of the parent molecule which is subsequently dissociated.

The general picture of HCl ion pair formation is as follows. From the Cl^- speed distribution we know, that HCl absorbed exactly 3 photons. The $H^+ + Cl^-$ term is singular and correlates to the $V^1\Sigma^+$ molecular state, i.e. there is no other way to produce $H^+ + Cl^-$ except the $V^1\Sigma^+$ molecular state. These two statements make clear that HCl*($V^1\Sigma^+$) absorbs a third photon and subsequently returns to the V state in a radiationless manner as described in detail below.

An intriguing result proving the outlined mechanism is shown in Fig. 4.4. We observed a pronounced variation of the total Cl^- yield with the vibrational quantum number v'=7-14 of the resonantly excited intermediate state $V^1\Sigma^+$. The largest yield occurs for v' = 12. The yield decreases for adjacent vibrational quantum numbers to zero, whereas a small secondary maximum is observed for v' = 8. While not shown here, we also observed ion pair formation following initial resonant excitation of the $E^1\Sigma^+$ and $g^3\Sigma^-(0^+)$ states. We interpret these features as being due to strongly varying Franck-Condon factors between the initially excited $V^1\Sigma^+$ state and a secondary intermediate Rydberg state IS_2 acting as gateway state to ion pair fragmentation. We modeled this behavior for the strongest transition $X^1\Sigma^+ \rightarrow V^1\Sigma^+(v'=12) \rightarrow IS_2$ by calculating wavefunctions for all involved states of HCl, which have been reproduced from the references.[26,27] We assumed that the intermediate state IS_2 acting as gateway state to photoion pair production is formed from the same potential energy surfaces ($E^1\Sigma^+$ and $V^1\Sigma^+$) that also combine to form the double minimum $B^1\Sigma^+$ state. Then the inner wall of IS_2 will essentially be contributed to by the ion pair state itself, and an adiabatic transition through the avoided crossing with the Rydberg state forming the IS_2 outer part will occur with large probability and result in ion pair dissociation. By tuning the laser, we do not only change the wavelength and the vibrational quantum number v' of IS_1 (the $V^1\Sigma^+$ state), but also the position of the outer turning point of vibrationally excited HCl. The ion pair yield is a most sensitive gauge for the resulting overlap of the $IS_1(V^1\Sigma^+)$ wavefunction with the IS_2 gateway state wavefunction. Calculation results are depicted in Fig. 4.4 for v' = 12. The intermediate state $IS_1(V^1\Sigma^+,v'=12)$ is resonantly ionized by tuning the excitation laser, while the gateway state IS_2 is predominantly accessed from the molecular geometry with maximum overlap of IS_1 and IS_2 wavefunctions. Ion pair fragmentation occurs after a non-adiabatic transition back to the $V^1\Sigma^+$ state. The return of the molecule from the originally excited $V^1\Sigma^+$ state back to the $V^1\Sigma^+$ state via IS_2 is peculiar, but purely incidental because the $V^1\Sigma^+$ state is easily accessible owing to well-characterized and strong transitions from the electronic ground state. It must be noted, however, that the same mechanism occurred for initial excitation of the $E^1\Sigma^+$ and $g^3\Sigma^-$ states as well.

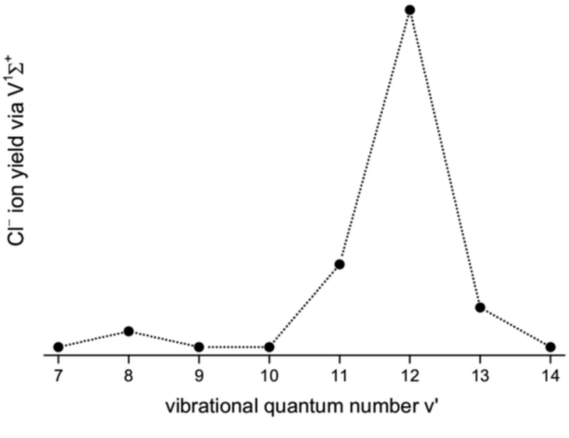

Fig. 4.4: Dependence of the ion yield on the vibrational quantum number v' of the resonantly excited $V^1\Sigma^+(v')$ state.

Several more features of the complex fragmentation mechanism of HCl following resonant multi-photon excitation were observed, most importantly the dependence of the ion pair yield (Fig. 4.5) on laser intensity.

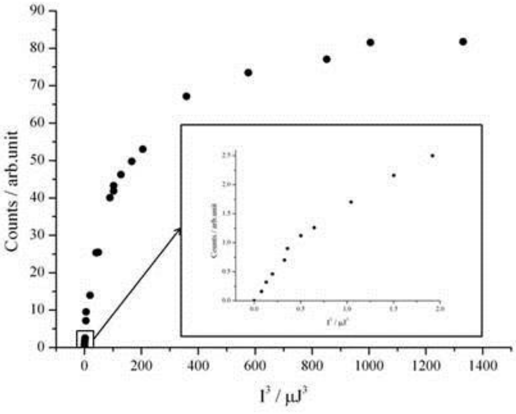

Fig. 4.5: Dependence of Cl^- yield on the third power of the laser intensity measured for $IS_1 = V^1\Sigma^+(v'=12)$. The inset shows the laser intensity range for which a linear dependence of the ion signal on the third power of the laser intensity is experimentally observed. For larger laser intensities saturation effects are responsible for the deviation of the cubic dependence.

This dependence from the third power of laser light intensity is linear only at reduced intensities, reflecting the three photon origin of ion pair formation. At higher intensities the process becomes proportional to lesser powers of the laser intensity owing to saturation. The discussion of the more complicated effects is beyond the scope of this letter. Similar calculations of the nuclear wavefunction overlap integrals as shown in Fig. 4.6 were performed for all experimentally monitored vibrational levels (cf. Table II), and the pronounced intensity variation around v' = 12 as well as the bimodal intensity distribution of Fig. 4.4 are in accordance with the proposed decay mechanism. Moreover, wavefunction calculations predict the outcome of experiments on hitherto unstudied transitions.

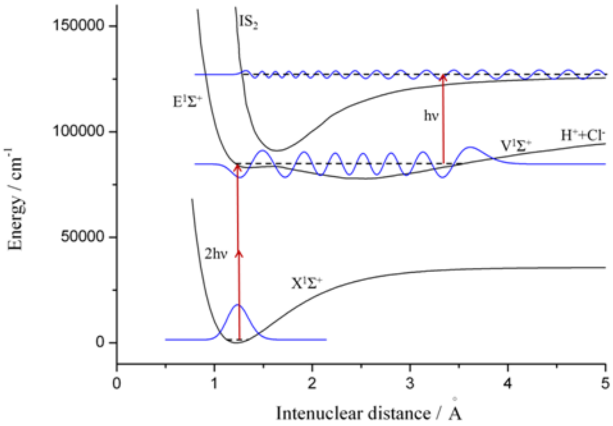

Fig. 4.6: Representation of the photoion pair production process in HCl. The first intermediate state IS_1 is resonantly ionized by tuning the excitation laser through the second intermediate state IS_2 - the gateway state to photoion pair production. The latter is predominantly accessed from the molecular geometry with maximum overlap of IS_1 and IS_2 wavefunctions, shown here for the case $IS_1 = V^1\Sigma^+(v'=12)$. Fragmentation into ion pairs occurs after a non-adiabatic transition back to the $V^1\Sigma^+$ state.

V	7	8	9	10	11	12	13	14
I_V/I_{12}	0.0025	0.2116	0.0576	0.0184	0.5086	1	0.2931	0.0039

TABLE II: Relative value of the product of two overlap integrals, characterizing both steps of ion-pair production process.

As conclusion, investigating ion pair dissociation by studying both positive and negative photoions simultaneously allows one to experimentally select photoion pair production as the reaction of interest among a variety of competing processes generating chemically identical products. Employing resonant multi-photon excitation allows one to enlarge the portions of relevant potential energy surfaces amenable to experimental interrogation. Using 3D imaging provides complete information about fragment quantum states, three-dimensional momentum vector distributions and spatial fragment anisotropies. Thus, simultaneous detection of positive and negative photoions has a very large potential to facilitate the data analysis of ion pair fragmentation processes. Similar studies are feasible for larger molecules, provided similar excitation schemes for intermediate states with large equilibrium internuclear distances exist. More specifically, our results show that intermediate Rydberg gateway states play a decisive role in the formation of photoion pairs in HCl.

References

---

[1] A. Terenin and B. Popov, Phys. Z. Sowjetunion 2299 (1932)

[2] J. Berkowitz, in *VUV and Soft X-Ray Photoionization*, ed. by U. Becker and D.A. Shirley (Plenum Press New York, 1996)

[3] A.G. Suits and J.W. Hepburn, Annu. Rev. Phys. Chem. **57**, 431 (2006).

[4] D.A. Shaw, D.M.P. Holland, and I.C. Walker, J. Phys. B: At. Mol. Opt. Phys. **39**, 3549 (2006).

[5] T. Ridley, J.T. Hennessy, R.J. Donovan, K.P. Lawley, S. Wang, P. Brint, and E. Lane, J. Phys. Chem. **A112**, 7170 (2008).

[6] C. Maul, A.I. Chichinin, and K.-H. Gericke, J. At. Mol. Opt. Phys. 410108 (2011).

[7] A.I. Chichinin, T. Einfeld, C. Maul, and K.-H. Gericke, Rev. Scient. Instrum. **73**, 1856 (2002).

[8] A.I. Chichinin, T. Einfeld, K.-H. Gericke, and C. Maul; in *Imaging in Molecular Dynamics: Technology and Applications*, ed. by. B. Whitaker (Cambridge University Press, Cambridge (2003).

[9] A.I. Chichinin, S. Kauczok, K.-H. Gericke, and C. Maul, Int. Rev. Phys. Chem. **28**, 607 (2009).

[10] C. R. Gebhardt, T. P. Rakitzis, P. C. Samartzis, V. Ladopoulos and T. N. Kitsopoulos, Rev. Sci. Instrum. **72**, 3848 (2001).

[11] D. Townsend, M. P. Minitti and Arthur G. Suits, Rev. Sci. Instrum. **74**, 2530 (2003).

[12] C. Romanescu, S. Manzhos, D. Boldovsky, J. Clarke, and H.-P. Loock, J. Chem. Phys. **120**, 767 (2004).

[13] S. Manzhos, C. Romanescu, H.-P. Loock, and J.G. Underwood, J. Chem. Phys. **121**, 11802 (2004).

[14] C. Romanescu and H.-P. Loock, J. Chem. Phys. **127**, 124304 (2007).

[15] A. Kvaran, H. Wang, K. Matthiasson, A. Bodi, and E. Jonsson, J. Chem. Phys. **129**, 164313 (2008).

[16] K. Matthiasson, H. Wang, and A. Kvaran, J. Mol. Spectrosc. **255**, 1 (2009).

[17] A. Kvaran, K. Matthiasson, and H. Wang, J. Chem. Phys. **131**, 044324 (2009).

[18] K. Matthiasson, J. Long, H. Wang, and A. Kvaran, J. Chem. Phys. **134**, 164302 (2011).

[19] J. Long, H. Wang, and A. Kvaran, J. Chem. Phys. **138**, 044308 (2013).

[20] A.I. Chichinin, C. Maul, and K.-H. Gericke, J. Chem. Phys. **124** ,224324 (2006).

[21] A.I. Chichinin, P.S. Shternin, N. Gödecke, S. Kauczok, C. Maul, O.S. Vasyutinskii, and K.-H. Gericke, J. Chem. Phys. **125**, 034310 (2006).

[22] S. Kauczok, C. Maul, A.I. Chichinin, and K.-H. Gericke, J. Chem. Phys. **133**, 024301 (2010).

[23] NIST-JANAF Thermochemical Tables, ed. by M.W. Chase Jr., 4th ed., J. Phys. Chem. Ref. Data 1998, Monograph No. 9,

[24] G. Audi and A.H. Wapstra, Nucl. Phys. **A595**, 409 (1995).

[25] Q.-B. Lu and L. Sanche, J. Chem. Phys. **115**, 5711 (2001).

[26] P. J. Bruna and S. D. Peyerimhoff, Ab initio Methods in Quantum Chemistry, edited by K. P. Lawley, Wiley, New York, (1987).

[27] H. Lefebvre-Brion, H. P. Liebermann and G. J. Vázquez, J. Chem. Phys. **134**, 204104 (2011).

5 Double arm 3D Ion Imaging apparatus with the function of produced ions loss characterization

Abstract: The double side spectrometer 3D Ion Imaging apparatus was constructed to solve the problem of a full quantitative characterization of multiphoton fragmentation of a small molecule. This characterization requires the determination of the absorption cross sections of the radiating steps of resonance enhanced multiphoton ionization (REMPI) and dissociation channels of the molecule including radical formation as well as ion pair formation. The study of ion-pair channel demands the detection of negative ions simultaneously with the detection of positive ions, used for the analysis of the other channels. Moreover to guarantee the precise experimental determination of the absorption cross section one needs to characterize the loss of produced ions in the spectrometer before detection.

The constructed set-up allows to perform simultaneous measurements of the three dimensional velocity vector distribution of positive and negative fragments. The HCl molecule 2+1 photon fragmentation is used to examine the set-up because of the rich set of fragmentation channels (ion-pair channel among them), taking place simultaneously. The simplicity of the ion-pair in the case of HCl as well as the direct relation of the nature of the excited state with the angular distribution of photofragments make HCl ion-pair photodissociation channel the most convenient one to test the detection of negative ions. By means of negative particle imaging the electron production on the spectrometer grids was observed. This process in combination with a special new set-up configuration, presented in the work, opens the way to perform a spectrometer self-characterization, which describes the loss of photoions in the spectrometer. This is necessary for the precise counting of all fragments produced as a result of photodissociation or photoionization, and not just of unknown portion of detected fragments.

5.1 Introduction

The resonance enhanced multiphoton excitation of a diatomic molecule with subsequent fragmentation (photodissociation or photoionization) has for decades been in the focus of interest of many laboratories as an effective method for studying the structure of high-lying excited states and for monitoring chemical reaction products. The multiphoton fragmentation of diatomic molecules can be described according to the scheme:

$$AB \xrightarrow{n h\nu} AB^*(IS_1) \xrightarrow{h\nu} AB^+ \tag{5.1.1a}$$

$$\xrightarrow{h\nu} A + B^* \tag{5.1.1b}$$

$$\xrightarrow{h\nu} A^* + B \tag{5.1.1c}$$

$$\xrightarrow{h\nu} A^+ + B^- \tag{5.1.1d}$$

$$\xrightarrow{h\nu} \ldots \tag{5.1.1e}$$

Scheme 5.1.1

In the simplest case of multiphoton excitation the molecule absorbs two photons to reach an excited intermediate state IS_1. The theoretical expressions of the two-photon absorption cross-section, characterizing this process, which is the first step of molecular multiphoton fragmentation (Scheme 5.1.1), were presented by Bray and Hochstrasser [1].

To perform an experimental measurement of two-photon absorption cross sections one needs to count how many fragments are .produced as the result of the absorption of a well defined amount of energy per unit time. The method of ion imaging with simultaneous measurement of the laser power allows one to couple the precise number of the ions resulting from molecular fragmentation and the photon number in the laser beam, which starts the ions production. However to use this combination it is necessary to guarantee, that the number of ions detected by means of ion imaging is equal to the number of ions produced after the molecular photodissociation. In other words it is necessary to characterize quantitatively the loss of produced ions before the detection. However this characterization is only one aspect of the task of experimental measurement of two-photon absorption cross-section.

Another aspect is in the monitoring of all the products of molecular fragmentation listed in scheme 5.1.1. For the experimental realization one needs a double side experimental apparatus which can detect simultaneously (or even coincidentally) positive as well as negative products. Such a principle was realized in a set of works to study dissociative photoionization of molecules by means of the photoion-photoelectron coincidence momentum imaging method (PEPICO).[2,3,4,5,6,7,8,9,10,11]

In contrast to those photoionization studies the coincidence imaging method or our simpler method of simultaneous detection (where it is not necessary, that two fragments belong to the same elementary process) of ions with opposite charges was not used to study the formation of ion-pair emerging from molecule photofragmentation channel (Scheme 5.1.1d), which one need to examine to monitor all the products of photofragmentation. The main difference with the PEPICO study of photoionization is, that in the process of the latter one analyzes only the photoionization channel, which is not accompanied by other fragmentation channels. Here only photoelectrons occur as negative particles representing the desired signal, while the broad set of photofragmentation products, obtained after resonance enhanced multiphoton excitation of the molecules upon ionization produce a large number of photoelectrons simultaneously with negative photoions. These electrons might saturate the MCP and affect the detection of negative ions.

In order to solve both aspects of the task of an experimental two-photon absorption cross-section measurement a double spectrometer experimental set-up was constructed which is able to perform a self-characterization of the loss of produced ions before detection as well as to detect positive and negative photoions simultaneously, avoiding the saturation of the system by photoelectrons.

To test the self characterization loss function of this set-up it is possible to use any molecular multiphoton fragmentation, whereas to examine the simultaneous detection function one needs a molecule, which possesses the ion-pair channel of photodissociation. For a set of molecules (F_2, O_2, N_2O, Cl_2, CH_3Cl, CH_3Br) the 2D imaging method was already applied to study the ion-pair channels [12,13,14,15,16,17,18,19,20,21]. Here the photodissociation of the HCl molecule was chosen as a benchmark because in the case of ion-pair product formation the negative ion of chlorine has the simplest partner H^+ possible. Therefore only kinetic recoil energy and no internal energy distribution has to be taken into account. Moreover, in the diatomic HCl molecule, the angular distribution of photofragments reveals the nature of the excited state, whereas for nonlinear polyatomic molecules (for example CH_3Cl [12,13], CH_3Br [21]) other factors may modify the angular distribution as well.

As a result the direct measurement of the 3D velocity distribution of negative chlorine ions in combination with the 3D velocity distribution of its partner can provide the complete description of the ion-pair photodissociation channel, allowing to prove the correct work of the apparatus.

The current paper presents the new experimental set-up fulfilling the described demands. It allows to measure simultaneously the 3D velocity vector distributions of positive and negative ions, avoiding the problem of MCP saturation by the electrons, produced in the double spectrometer in a set of processes: the photoionization (photoelectrons), collisional induced electron emission from the grids of the spectrometer or from MCP. As a benchmark system the 2+1 multiphoton fragmentation of the HCl molecule via the excited state $V^1\Sigma^+(v=12)$ is used.

In addition to double side set-up configuration another special configuration is developed, which organizes a trap for the positive ion in a way that they undergo the periodic motion in one arm of the double spectrometer. The control of periodic collisional induced electron emission from the grids allows to characterize the loss of the ion number occurring during their motion in the spectrometer.

5.2 Experimental set-up

Our ion imaging experimental set-up previously used only for the study positive ions (single spectrometer version) [22,23,24,25,26,27,28,29,30,31] was modified to enable the detection of negative ions as well. The single spectrometer version has previously been described in detail [32,33,34].

The extended set-up differs from the original version by an additional, second TOF spectrometer being the mirror reflection of the first, sharing the symmetry axis and equipped with two independent detectors. A pulsed nozzle (General Valve Series 9) is installed oriented perpendicularly to the spectrometer axis instead of on the axis as before. The nozzle injects a supersonic molecular beam between the two spectrometers, where it is intersected by a laser beam propagating perpendicularly to the molecular beam and to the spectrometer axis likewise. Laser beam (X), molecular beam (Y) and spectrometer axis (Z) define the Cartesian coordinate system of the experimental set-up.

The principal scheme of the double spectrometer set-up is presented in a Fig. 5.2.1.

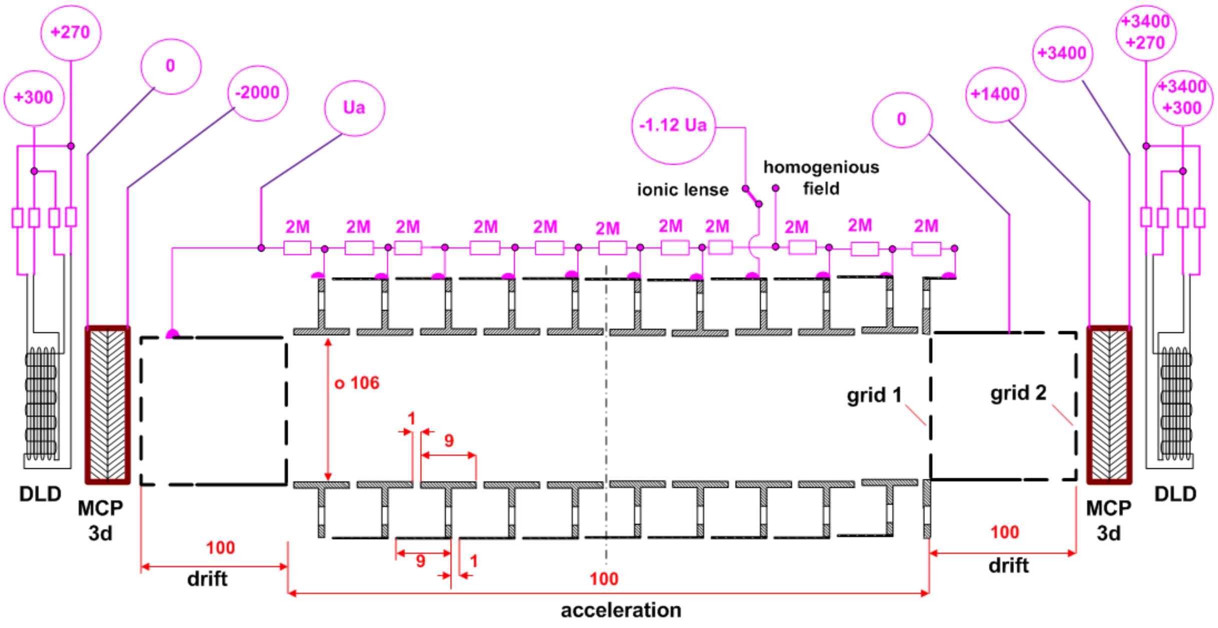

FIG 5.2.1: Electrodes configuration and voltage supply to the double side-spectrometer.

5.2.1 Laser system

For the performance characterization of the modified 3D imaging double spectrometer set-up the photo ion pair dissociation of HCl was employed. Laser irradiation in the region under investigation (234 nm – 240 nm), produced by frequency doubling the output of tunable Nd:YAG-pumped dye laser, is used to excite the HCl molecule. The laser polarization is linear and oriented along the spectrometers axis.

5.2.2 Vacuum system/molecular beam

To guarantee a sufficiently low background pressure (10^{-7} mbar) the vacuum chamber is pumped by two turbomolecular pumps (Pfeiffer TMU 260 and Pfeiffer TMH 521 P). The pumps are forepumped by a rotary vane pump filled with oil. When the nozzle is operating, the integral pressure is on the order of 10^{-5} mbar.

5.2.3 TOF spectrometers

Each spectrometer consists of an acceleration region which separated by a grid (grid 1 in the text) from a field free drift region twice as long as the acceleration region. This geometry for one field spectrometer has several advantages if the field gradient is constant. First, it automatically yields spatial focusing in the spectrometer axis (Z). Second, the relationship between the TOF and z-velocity is linear and third it yields a good energy dispersion dt/dE suitable for 3D Ion Imaging.

The acceleration regions of the spectrometers form one common acceleration region, which consists of ten ring electrodes (five for each spectrometer) with an inner diameter of 106 mm, kept apart by glass rods. They have an inner rim of 9 mm length and the distance between them is 1 mm. Thus, the acceleration region is a closed tube with 1 mm gap every 9 mm. This guarantees optimal shielding of external electrical fields and also makes the field very homogeneous near the electrodes. The laser beam and the molecular beam enter the stack of electrodes at right angle between electrodes 5 and 6 directly in the center of the common acceleration region.

The acceleration voltage (Stanford Research System, Model PS350) is either split by eleven 2 MΩ resistors (Fig. 5.2.1) in order to obtain a homogeneous electric field, or applied to the eighth electrode which is connected to the first electrode by a set of resistor 2.2 MΩ and the remainder split again uniformly (electrode 7 and 9 are connected by two resistors, because the distance is two times longer). In this case the electrodes 7, 8 and 9 serve as Einzel lens and their field is superimposed by a homogeneous field (Velocity Mapping configuration). The electric field in the acceleration region of the left side spectrometer is always homogeneous, even if the Einzel lens is switched on.

5.2.4 Detectors

After having passed the right-side TOF spectrometers, the ions are projected onto commercial 3D Imaging detectors (double stage multichannel plate (MCP) assembly + Delay line (DL), Roentdek)[35,36]. To sufficiently accelerate the ions under investigation to the energy for the production of secondary electrons in the MCP a voltage is applied between grid 2 and the front side of MCP stack. Another voltage is applied between the front and the back side of the MCP stack for the generation and acceleration of the secondary electrons. Voltage in the “old” and the “new” spectrometers can be independently adjusted for the detection of negative or positive ions.

The eight signals from the four lines of the Delay Line and two signals from Single line are decoupled from the high DC voltage, differentially amplified by an eight channel differential amplifier (KSU EDL DLA800), and finally recorded and analyzed by a four channel LeCroy 500 MHz oscilloscope (Waverunner 6050, Quad 5Gs/s). The resulting four individual delay line signals are fit by Gaussians in order to determine the center of the electron cloud emerging from the MCP stack. From the point of impact and the time of flight for every detected ion are extracted.

5.3 Double spectrometer experiment

The double spectrometer set-up configuration (Fig. 5.3.1a, 5.3.1b) allows one to perform the simultaneous detection of negatively and positively charged particles resulting from molecular fragmentation. However the detection of negative ions can be disturbed by electron production inside the spectrometer by a variety of processes. The detector of negative particles is extremely sensitive to the electrons and can easily be saturated by them. The current section is dedicated to the solution of the detector saturation issue by electrons and to monitoring the true ionic signal.

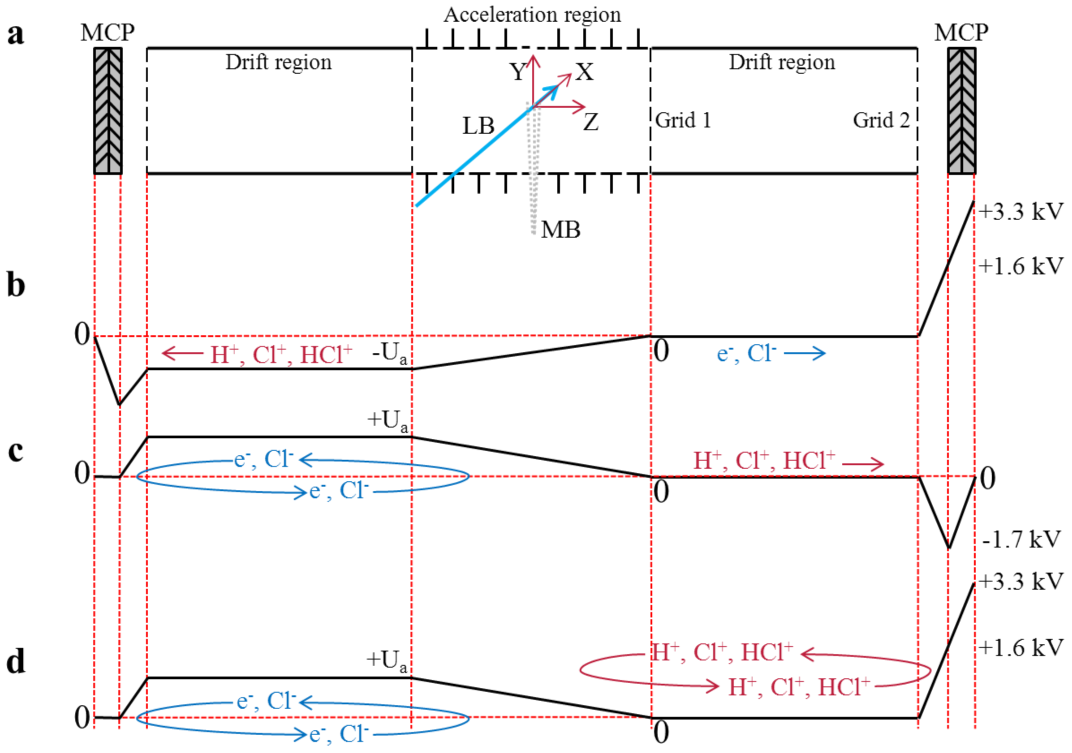

FIG 5.3.1: **(a)** Schematic representation of the double-arm spectrometer. Potential configuration in the case of **(b)** double spectrometer configuration, **(c)** classical configuration and **(d)** special configuration of the experimental set-up.

The negative chlorine ions resulting from the ion-pair channel of photodissociation are obtained according to the mechanism:

$$HCl\ (X^1\Sigma^+) \xrightarrow{2h\nu} HCl^*(IS_1) \xrightarrow{h\nu} HCl^{**}(IS_2) \longrightarrow HCl^{**}(V^1\Sigma^+) \longrightarrow H^+ + Cl^- \quad (5.3.1)$$

The previous investigation of the ion-pair channel performed with positive hydrogen ion imaging yielded the anisotropy β parameter to be close to 2 [37,38]. In the case of laser light polarization parallel to the spectrometer axis this should result in two peaks in the time-of-flight profile shown in Fig. 5.3.2, reflecting produced Cl^- ions with the z-component of the velocity vector oriented towards and away from the negative ion detector. However the detector does not show any signal of such kind (Fig. 3, blue line). This is due to the saturation of the MCP by photoelectrons resulting from HCl photoionization, which is a much more effective process, than Cl^- production.

The disturbing effect of those photoelectrons might be eliminated by the installation of two permanent magnets producing a homogeneous field oriented along X axis in the beginning of the drift region of the right-side spectrometer (Fig. 5.3.1). Because of the much larger mass of the chlorine negative ion, its trajectory is not noticeably affected. The photoelectron number reduction avoids the saturation of the MCP (Fig. 5.3.2, red line), which allows one to detect the negative photoions. However, some noise in the time-of-flight spectrum as well as a sharp peak at about 9.8 μs right after the Cl^- peaks still exists at slightly larger times then negative chlorine ions time. The installation of a second pair of permanent magnets in the end of the drift region almost completely eliminates the electron impact on the right-side spectrometer MCP and effectively removes saturation (Fig. 5.3.2, black line). The experiment shows that the most effective orientation of the second field is perpendicular to the first one. After the installation of the second pair of magnets one can see that the peak at 9.8 μs is accompanied by the broad one at shorter time about 9.65 μs.

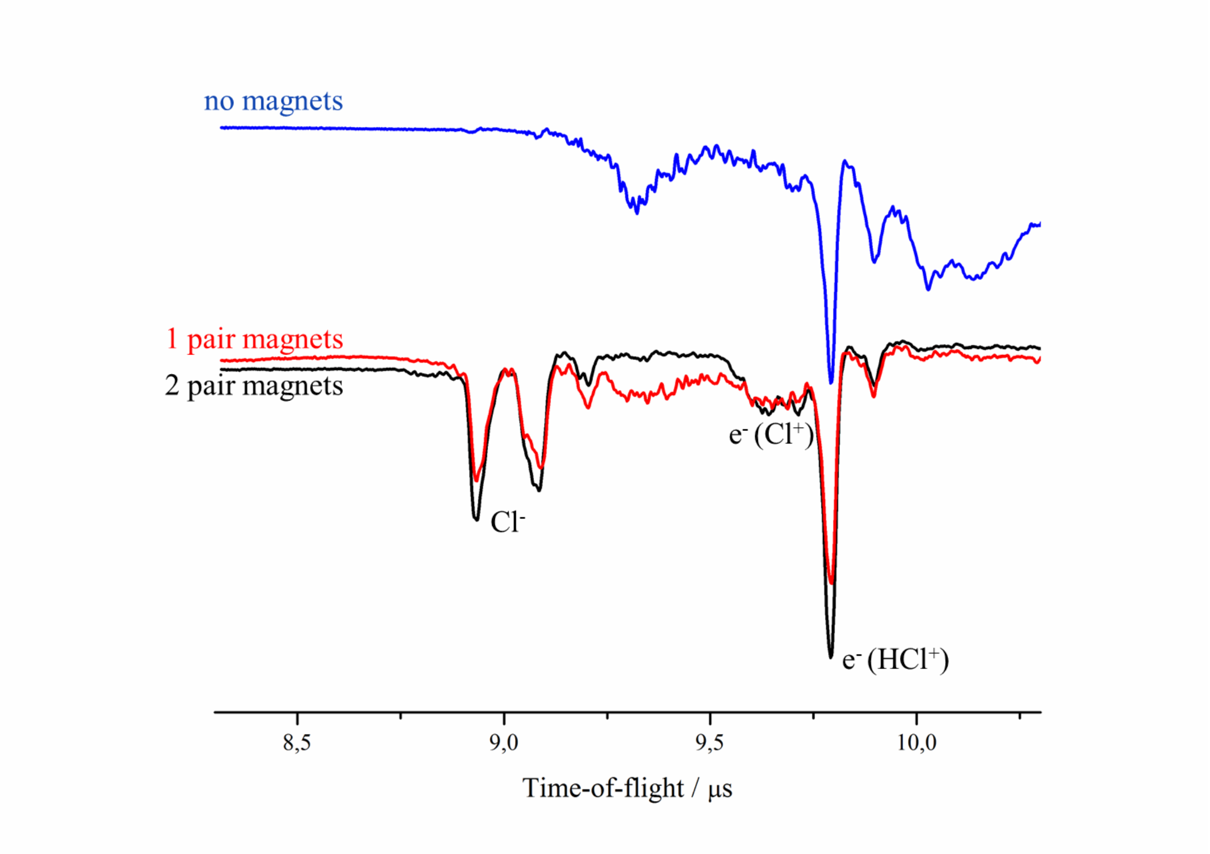

FIG 5.3.2: Representation of the magnets installation in the drift region of one spectrometer influence on the performance of the negative ions detection by the MCP.

The broad and the sharp peaks mimick the time-of-flight profile of Cl and HCl positive ions and disappear, if the left-side spectrometer is switched off. The peaks obviously reflect the ability of the left-side spectrometer MCP to emit electrons after the impact of positive Cl^+ and HCl^+ ions. These electrons are then accelerated in the direction of the right-side spectrometer by the electric potential difference between the front side of the MCP and the grid 2. On the way towards the negative ion detector they are once again accelerated in the acceleration region. Because of the small mass of the electrons in comparison to ions, they cover the distance between the two detectors in a very short time, which can be calculated according to the simple kinematics formulae.

These facts show that in case of the work with the negative ion detector and the analysis of negative photoions all possible channels of electron production have to be taken into account. The processes of photoionization and the emission of electrons from the MCP were shown to be very intense sources of electrons. Also the installed grids can be intense sources of electrons as well.

5.4 Electron production on the grids

The negative chlorine ions produced in ion-pair photodissociation of HCl with an intermediate state $V^1\Sigma^+$(v=12, Q(0)) acquire a relatively high kinetic energy (150 – 750 eV) in the acceleration region of the mass-spectrometer. When the spectrometer is operated in negative ion mode (Fig. 5.3.1b) this energy is enough to start collision induced electron emission from the surfaces of the grids or from the chlorine negative ions with a broad angular distribution. In case of grid 1, separating acceleration and drift regions, most of the produced electrons will therefore be lost upon impact on the walls of the drift region, and only a small portion of them will be detected. In contrast in case of grid 2 separating drift and detector regions those electrons initially oriented towards the MCP will be further accelerated towards the MCP by the MCP supply voltage.

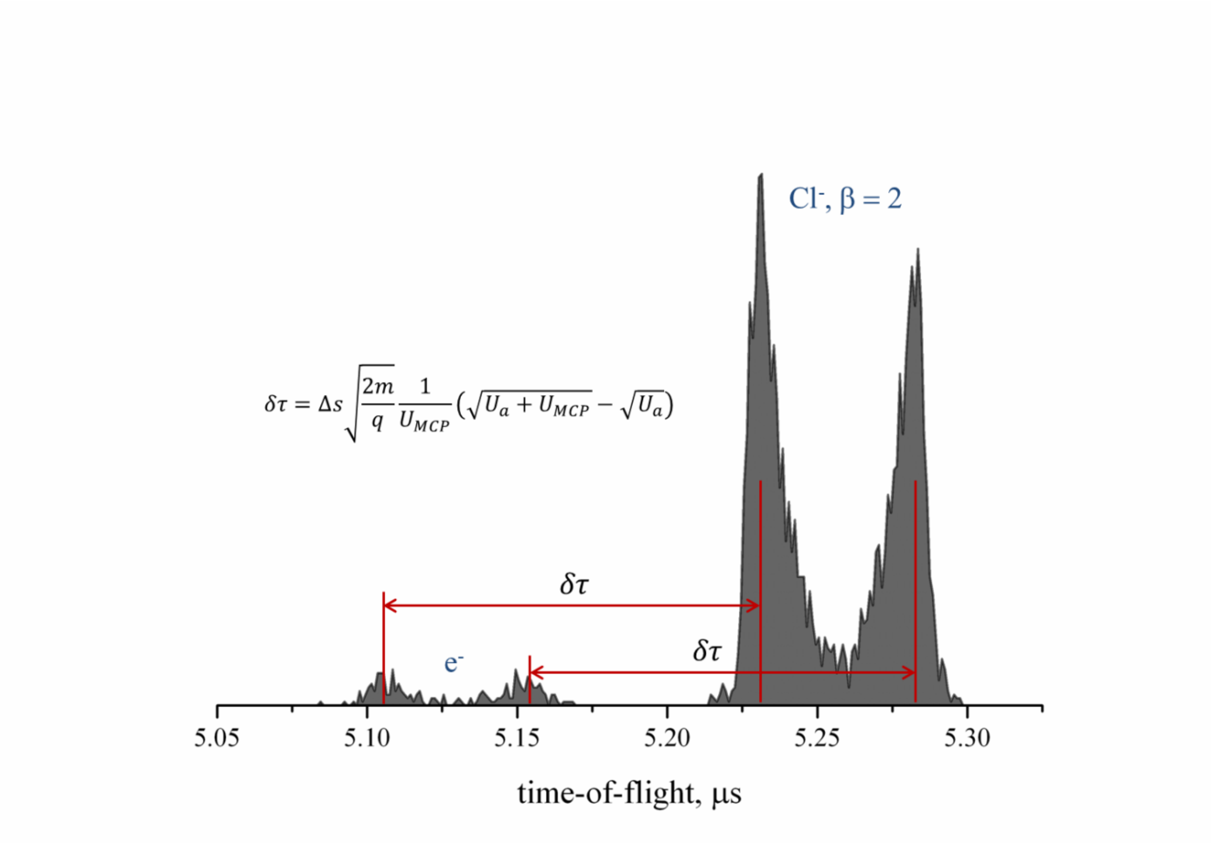

FIG 5.4.1: TOF-profile of the detected negative ions Cl^- produced in the process of HCl ion pair dissociation via resonant two-photon excitation of the $V^1\Sigma^+$(v=12,J=0) intermediate state. Laser polarization is oriented along the spectrometer axis. At shorter time the traces of electrons production on grid 2 are observed.

All of these electrons will impact on the detector with a negligible time delay of less than 1 ns after the ion impact on the grid, given the short distance d = 8 mm between the grid and the MCP surface. This results in additional peaks in the time-of-flight spectrum located at shorter times-of-flight than the peaks of the negative chlorine ions. The time difference between the corresponding peaks of emitted electrons and negative chlorine ions is essentially equal to the time-of-flight of the ion from grid 2 to the MCP.

The efficiency of electron production increases with the acceleration voltage, i.e. with the kinetic energy of the negative chlorine ion, which impacts on grid 2. The dependence summarized in Table I reflects the fact that the incoming chlorine ions with higher energy produce a larger number of electrons on the grid.

E_{kin}, eV	150	300	450	600	750
Efficiency	0.08	0.14	0.18	0.19	0.22

TABLE I: The efficiency of electron production by the negative chlorine ion with different kinetic energies

5.5 Special configuration of the set-up: forward/backward scattered electrons and positive ion recharge

A process of electron emission can be activated by the positive ions as well. For example in case of the classical experimental (Fig. 5.3.1c) set-up configuration positive ions flying towards the detector can produce electrons on both grids. However these electrons will not be detected because of the repulsive electric potential difference between grid 2 and the MCP. As a result the analysis of emitted electrons can not be performed with the classical experimental set-up configuration.

The set-up configuration specialized for this analysis is shown in Fig. 5.3.1d. In the right side spectrometer a trap for positive ions is organized. The acceleration voltage and the voltage on the MCP are applied so that the positive ions (H^+, Cl^+, HCl^+) produced after HCl photoionization or photodissociation fly in the direction of the detector, which can detect only negative ions. Passing through grid 2, part of the positive ions will impact on it. As a result of these impacts the ions produce electrons (forward scattered secondary electrons) on grid 2. These (FSSE) electrons in their turn are accelerated to the MCP. As mentioned above the electrons produced in the process (a) (Fig. 5.5.1) must result in time-of-flight profile peaks located at slightly shorter times then the time-of-flight peaks of the corresponding positive ions detected in the classical experiment (see Section IV, Fig. 5.4.1). Between grid 2 and MCP the repulsive electric potential difference turns the trajectories of positive ions back to the acceleration region. The turned around positive ion impact on grid 2 once again after the time Δt

$$\Delta t = 4\Delta s\sqrt{\frac{m}{2q}}\frac{1}{U_{MCP}}\sqrt{U_a}, \tag{5.5.1}$$

where

Δs – distance between the grid 2 and the MCP,
m – mass of the ion,
q – charge of the ion,
U_a – acceleration electric potential difference,
U_{MCP} – electric potential difference between the grid 2 and MCP.

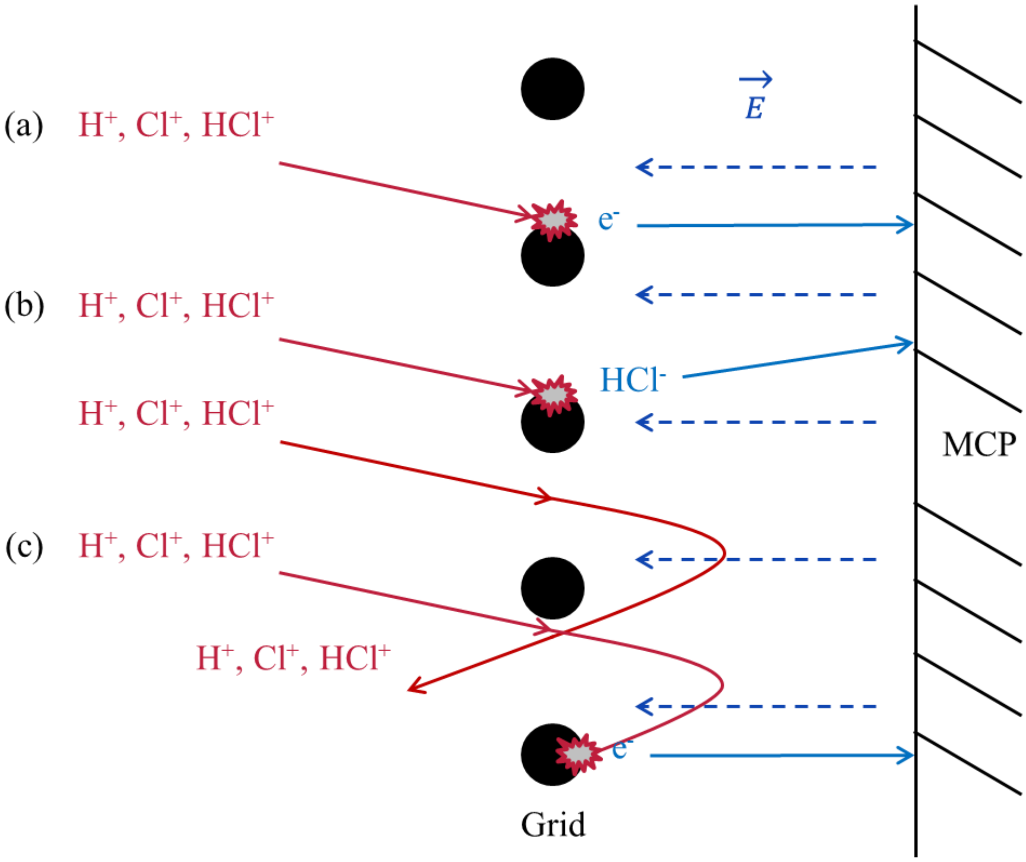

FIG 5.5.1: Schematic representation of the processes occurring on grid 2: (a) forward scattered electron production, (b) HCl^+ ion recharge, (c) backward scattered electron production.

Consequently they produce electrons (Fig. 5.5.1, process (c)), which are immediately detected on the MCP. These electrons are called backward scattered secondary electrons (BSSE).

As a result each type of positive ion (H^+, Cl^+ and HCl^+) should result in an even number of peaks in the time-of-flight profile around their time-of-flight. The exact number of peaks depends on the number of fragmentation channels, which lead to the formation of one kind of positive ion, as well as on the anisotropy β parameter of the velocity vector angular distribution, corresponding to each channel. For example in the simplest case of HCl^+ ions, resulting from only one channel of HCl photoionization with the anisotropy β parameter close to zero [29] we find two peaks. They correspond to the FSSE and BSSE. In the case of positive ion of hydrogen with the angular distribution characterized by β parameter close to 2 (two peaks in TOF profile), one will gave four peaks, corresponding to emitted electrons (2 FSSE, 2 BSSE).

According to formula (5.5.1) and due to the fact that the width of the time-of-flight peak is inversely related to the acceleration voltage:

$$\Delta\tau \sim \frac{1}{U_a}, \tag{5.5.2}$$

it is easy to see, that to resolve all peaks one needs a relatively large acceleration electric potential difference. However in this case the time-of-flight of hydrogen ions is short, and the corresponding time-of-flight peaks are situated in the time range, where the saturation of the MCP by scattered photons is still strong. Therefore it is not possible to use the information about hydrogen in the qualitative characterization of the set-up. To perform a precise characterization one needs to analyze the processes of electron production on the grid by Cl^+ and HCl^+ ions.

The experiment shows, that the time-of-flight profile is even more complicated than from the peaks, which correspond to electron production on grid 2. In the time-of-flight region of Cl and HCl the profile consists of two strong and two relatively weak peaks (Fig. 5.5.2).

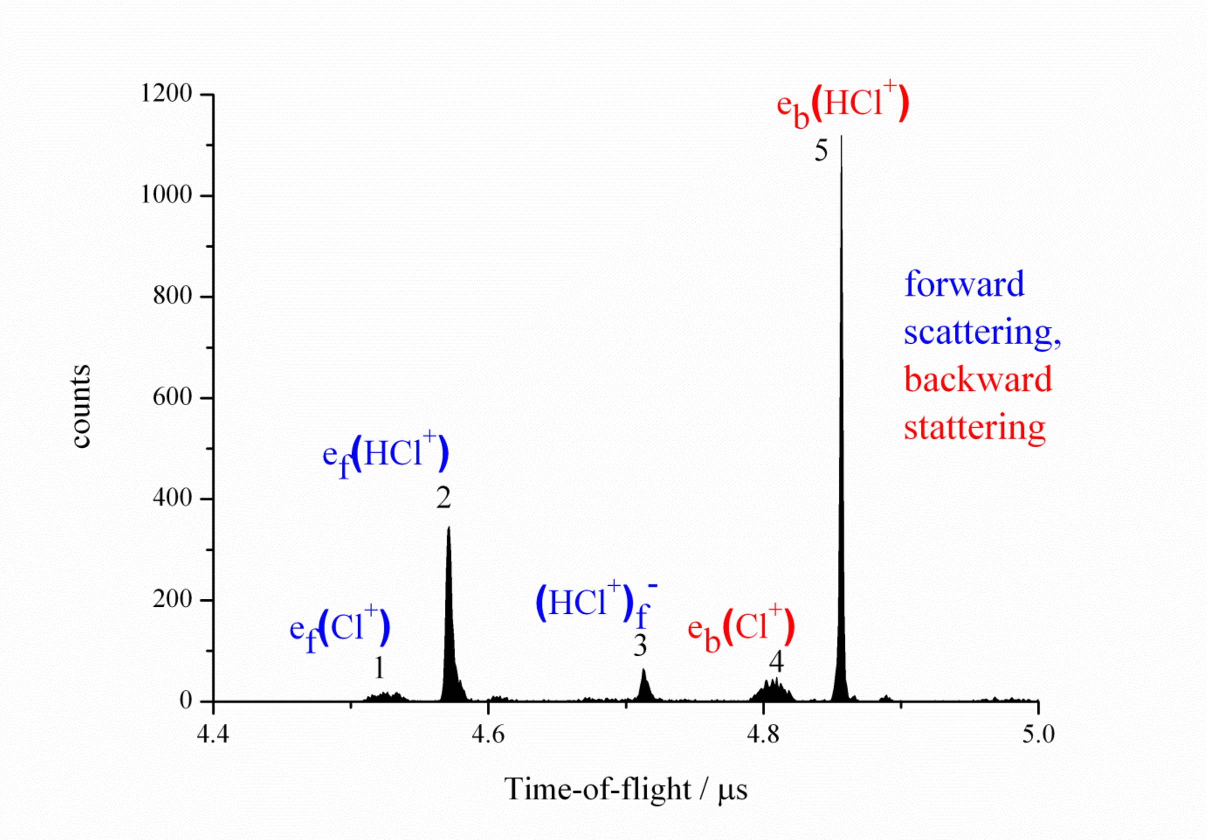

FIG 5.5.2: TOF profile showing the processes occurring on grid 2. Peaks 1 and 2 correspond to the forward scattered secondary electrons, produced in the processes $Cl^{+} + Grid \rightarrow e^{-}$ and $HCl^{+} + Grid \rightarrow e^{-}$, while peaks 4, 5 represent the backward scattered secondary electrons, produced by the ions Cl^{+} and HCl^{+}. The peak 3 reflects the recharge of HCl^{+} ions. The positive ion are obtained from the channels of HCl multiphoton fragmentation via resonant two-photon excitation of the $V^{1}\Sigma^{+}$(v=12,J=0) intermediate state.

From the calculation (see Chapter 5.4, Fig. 5.4.1) one can conclude that peaks **1** and **2** are the result of electrons produced on grid 2 in process **a** of Fig. 5.5.1. In turn according to the calculation (see Chapter 5.5, Eq. 2) peaks **4** and **5** belong to electrons produced in process **c** of Fig. 5.5.1.

Because of the relatively high voltage (1.6 kV) and short distance between grid 2 and MCP the impact on the MCP of electrons produced on the grid is instantaneous and their spatial distribution should mimick the distribution of the ions, detected in the classical configuration experiment (Fig. 5.5.3a). However the experiment shows strong differences in these distributions: in case of forward scattered (Fig. 5.5.3b) as well as in case of backward scattered electrons (Fig. 5.5.3c).

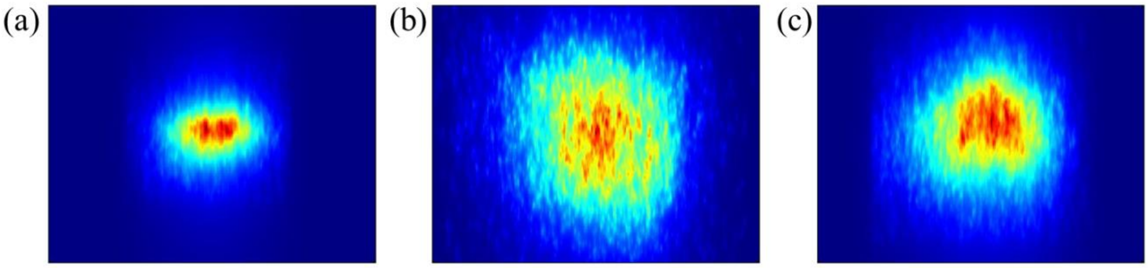

FIG. 5.5.3: Two-dimensional projection of 3D images for (a) positive ions HCl^+, (b) forward scattered electrons produced on the grid after the impacts of HCl^+, (c) backward scattered electrons produced on the grid after the impacts of HCl^+. HCl^+ is produced in a [2+1]-REMPI process via resonant two-photon excitation of the $V^1\Sigma^+(v=12,J=0)$ intermediate state.

Therefore, caution must be applied when using imaging of electrons produced on grid 2 electrons as a non direct method to analyze the positive ion.

The time corresponding to peak **3** in the Fig. 5.5.2 is very close to the time-of-flight of positive HCl^+ ions, measured in the classical experiment. It consists of the time-of-flight in the acceleration and the drift region (τ_1) and of the time in the area between the grid 2 and the MCP (τ_2). The time of peak **3** therefore describes the process, in which the same positive ion flies through acceleration and drift regions (τ_1), becomes negatively charged upon impact on grid 2, and is accelerated towards MCP as negatively charged HCl^-. For both experiments (classical and specially configured) the time τ_1 is equal, because it corresponds to the identical trajectories of the positive ion. The experimental results show that time τ_2 is larger in the specially configured case than in the classical case of HCl+ detection. This can be explained by the fact that the lifetime of the negative ion HCl- seconds [39] is very short in comparison to the time-of-flight from grid 2 to the MCP. After this the negative ion will decay according to:

$$HCl^- \rightarrow HCl + e^- \tag{5.5.3}$$

It is supposed that HCl^- was accelerated enough during its lifetime to be detected by MCP as HCl.

The processes of collision induced electron emission from the grid after the impacts of the ions Cl-, Cl+ and HCl+ (peaks 1,2,4, and 5 in Fig. 5.5.2) is suggested to be the result of the Auger-effect, occurring on the grid surface. In case of positive ions Auger-electron emission is accompanied by the neutralization of the positive ion. The detailed analysis of these processes is very complex and demands a separate discussion which will be done in a future article.

The process which describes the recharge (peak 3 in Fig. 5.5.2) can be written according to the scheme:

$$HCl^{+} + Grid \rightarrow HCl^{-} \qquad (5.5.4)$$

Here the positive HCl+ ion receives two electrons to form the recharged HCl- ion. This process is even more complicated, than the process of positive ions neutralization and will also be discussed in the future article.

5.6 Cycles of ions motion in the spectrometer

As it was mentioned above (Chapter 5.5, special configuration) the trajectories of positive ions, which do not impact on grid 2, are turned back in the direction of the acceleration region by the repulsive electric potential difference between grid 2 and MCP. The ions fly in the opposite direction and produce electrons and recharged ions each time impacting any grid. In the acceleration region the positive ion trajectories are turned once again by 180° and the ions fly for the second time to the negative ion detector of negative ions, starting the second cycle of positive ion motion. The roundtrip time is equal to the positive ion time-of-flight in the classical experiment and does not change for the subsequent cycles of motion. Thus, the period of motion is equal to the doubled positive ion time-of-flight. The scheme of periodic motion as well as the time-of-flight spectrum is shown in Fig. 5.6.1. The corresponding time-of-flight spectrum (Fig. 5.6.1b) confirms the idea that the first signature of electrons and recharged ions takes place at time τ, $\tau+\Delta t$, the second one occurs at time $3\tau+\Delta t$, $3\tau+2\Delta t$, and the third one at the time $5\tau+2\Delta t$, $5\tau+3\Delta t$ (Fig. 5.6.1b). Here τ is a time-of-flight in the acceleration and drift regions, while Δt – is a time of between the production of FSSE and BSSE.

The time-of-flight spectrum (Fig. 5.6.1b) shows also the formation of backward scattered electrons on grid 1 ($1.5\tau+\Delta t$, $3.5\tau+2\Delta t$), produced by positive ions flying in the direction of the acceleration region. There are no corresponding traces of electrons, however produced at times 0.5τ, $2.5\tau+\Delta t$, $4.5\tau+2\Delta t$, because these electrons are accelerated in the direction of the left-side detector.

The number of produced electrons decreases with each new cycle of motion. This results from the decrease of the number of positive ions owing to the impacts on the grid and to the formation of negative ions and neutral atoms on the grid. To characterize the positive ion loss, the probability P of ion loss on the grid, which is not dependant from the flight direction, is introduced. For N positive ions flying to the grid, only (1-P)N positive ions continue their flight after the grid.

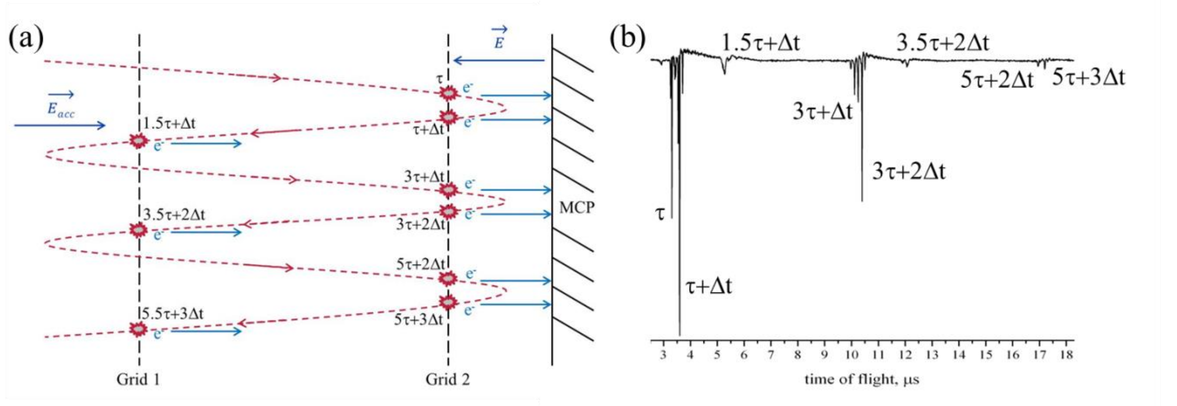

FIG 5.6.1: Representation of the periodic motion of positive ions in one spectrometer in case of its special configuration. **(a)** Scheme of the three cycles of motion. **(b)** TOF spectrum showing the collision induced electron emission from the grid in each cycle.

Before the first cycle of electrons and recharged particles (time gate around τ) **N** ions approach grid 2 from the drift region. Before the second cycle the ions pass the grids four times: two times near the MCP (τ, τ+Δt), one time entering the acceleration region (1.5τ+Δt) and another time exiting it (2.5τ+Δt). Thus the number of the positive ions as well as the number of electrons produced on grid 2 are reduced by the factor $(1-P)^4$. From the intensities of the peaks in the experimental time-of-flight profile, which corresponds to the electrons produced in the first and in the second cycle, one can then calculate the probability of positive ion loss on grid 2.

The probability is measured for Cl^+ and HCl^+ ions with different kinetic energy. It is found to be not dependent on the ion nature or kinetic energy of ion and equal to 19.5±0.05 %.

With the value P it is possible to obtain the exact number of ions, which were produced as a result of HCl photodissociation or ionization, from the number of ions detected in the classical configuration experiment. To do this one needs to divide the number of detected ions by the factor $(1-P)^2$. To obtain the number of ions approaching on grid 2 in the classical experiment configuration, one needs to divide the number of detected ions by the factor (1-P) correspondingly. Combining such a classical measurement with the measurement in the special configuration at the same experimental conditions, it is possible to couple the number of ions, approaching grid 2 with the number of electrons, produced by forward scattering, by backward scattering, and with the number of recharged ions, produced on the grid. In Fig. 5.6.2 we show the dependence of the number of produced negative particles for all three processes on the different kinetic energies of impacting positive ions.

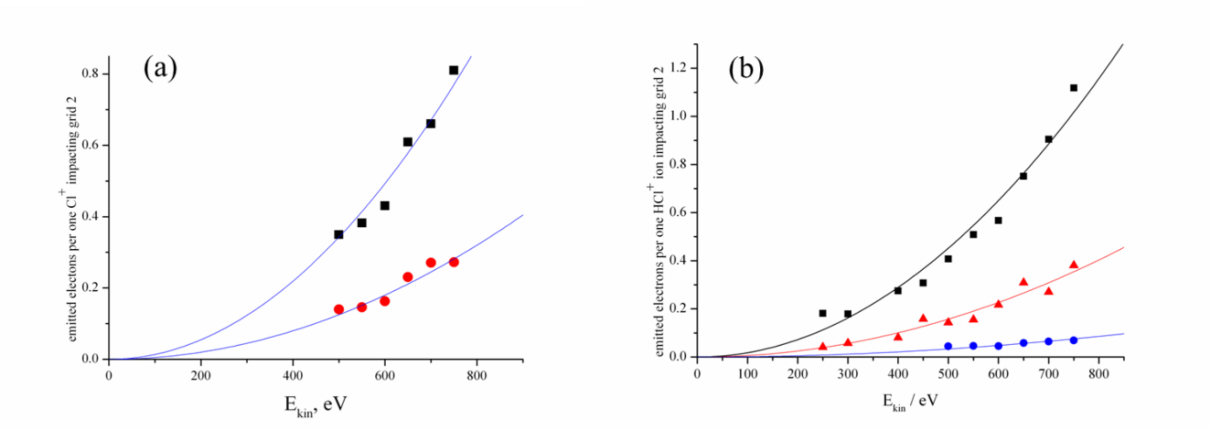

FIG. 5.6.2: The number of emitted forward scattered electron (red dots), backward scattered electrons (black dots) per one Cl^+ **(a)** or HCl^+ **(b)** ion impacting grid 2. This number is plotted against the kinetic energy of impacting ion.

The figures show that the efficiency of the electron emission increases with the increase of the increase of the kinetic energy of impacting ions.

5.7 Conclusion and outlook

In this contribution we report a double spectrometer imaging set-up which can measure the 3D velocity vector distribution of positive as well as negative products of molecular photofragmentation. To test the negative ion imaging performance the ion-pair channel of HCl photodissociation was studied. The study was realized due to the installation of two pairs of permanent magnets, producing a homogeneous field in the negative ion spectrometer avoiding saturation of the detector because of the large number of photoelectrons.

An additional special configuration of the experimental set-up was developed. It organizes the trap for positive ion in one of two spectrometers and allows to find the effect of electrons and recharged ions produced on the grids in the spectrometer after impact of negative and positive ions is observed and characterized. Positive and negative ions resulted from the photodissociation and photoionization of the HCl molecule. The effect of electrons produced on the grid in the trap configuration offers the possibility to characterize the set-up in terms of ion loss during the flight in the spectrometer. It was found, that each grid eliminates about 20 percent of flying ions.

The described method can be used in case of any molecule under investigation. Thus, the method is universal. The ion number reduction characterization allows to perform precise calculations of the number of produced ions from the number of detected ions such that experimental determination of two-photon absorption cross-section become possible.

5.8 References

---

[1] R. G. Bray, and R. M. Hochstrasser, Mol. Phys. **31**, 1199 (1976).

[2] J. H. D. Eland, M. Takahashi, and Y. Hikosaka, Faraday Discuss., **115**, 119 (1999).

[3] M. Takahashi, J. P. Cave, and J. H. D. Eland, Rev. Sci. Instr. **71**, 1337 (2000).

[4] T. Baer, International Journal of Mass Spectrometry **200**, 443 (2000).

[5] T. Baer, and Y. Li, International Journal of Mass Spectrometry **219**, 381 (2002).

[6] Y. Morishita, M. Kato, G. Prümper, X.-J. Liu, T. Lischke, K. Ueda, Y.Tamenori, M. Oura, H. Yamaoka, I. H. Suzuki, N. Saito, Radiation Physics and Chemistry **75**, 1977 (2006).

[7] D. Rolles, Z. D. Pešić, M. Perri, R. C. Bilodeau, G. D. Ackerman, B. S. Rude, A. L. D. Kilcoyne, J. D. Bozek, N. Berrah, Nucl. Instr. and Meth. In Phys. Res. B **261**, 170 (2007).

[8] A. Matsuda, M. Fushitani, A. Hishikawa, Journal of Electron Spectroscopy and Related Phenomena **169**, 97 (2009).

[9] K. Hosaka, R. Itakura, K. Yokoyama, K. Yamanouchi, A. Yokoyama, Chemical Physics Letters **475**, 19 (2009).

[10] A. Bodi, P. Hemberger, T. Gerber, B. Sztáray, Rev. Sci. Instrum. **83**, 083105 (2012).

[11] C. Wu, C. Wu, Y, Yang, Z. Wu, X. Liu, X. Xie, H. Liu, Y. Deng, Y. Liu, H. Jiang, and Q. Gong, Journal of Modern Optics **60**, 1388 (2013).

[12] X. Liu, R. L. Gross, A. G. Suits, Science **294**, 2527 (2001).

[13] M. Ahmed, D. S. Peterka, P. Regan, X. H. Liu, A. G. Suits, Chem. Phys. Lett. **339**, 203 (2001).

[14] Y. Hao, C. Zhou, Y. Mo, J. Phys. Chem. A **109**, 5832 (2005).

[15] Y. Hikosaka, E. Shigemasa, Journal of Electron Spectroscopy and Related Phenomena **148**, 5 (2005).

[16] Y. Hao, C. Zhou, Y. Mo, J. Phys. Chem. A **111**, 10887 (2007).

[17] C. Zhou, Y. Mo, J. Chem. Phys. **129**, 064312 (2008).

[18] A. G. Suits, J. W. Hepburn, Annu. Rev. Phys. Chem. **57**, 431 (2006).

[19] C. Zhou, Y. Hao, Y. Mo, J. Phys. Chem. A, **112**, 8263 (2008).

[20] Y. Hao, C. Zhou, Y. Mo, J. Phys. Chem. A **113**, 2294 (2009).

[21] D. Xu, J. Huang, R. J. Price, W. M. Jackson, J. Phys. Chem. A **108**, 9916 (2004).

[22] T. Einfeld, A. I. Chichinin, C. Maul, and K.-H. Gericke, J. Chem. Phys. **116**, 2803 (2002).

[23] T. Einfeld, A. I. Chichinin, C. Maul, and K.-H. Gericke, J. Chem. Phys. **117**, 1123 (2002).

[24] T. Einfeld, A. I. Chichinin, C. Maul, and K.-H. Gericke, J. Chem. Phys. **117**, 4214 (2002).

[25] A. I. Chichinin, T. Einfeld, C. Maul, and K.-H. Gericke, Chem. Phys. Lett. **390**, 50 (2004).

[26] L. Schäfer, N. Gödecke, O. Ott, C. Maul, K.-H. Gericke, P. S. Shternin, E. V. Orlenko, and O. S. Vasyutinskii, Chem. Phys. **301**, 213 (2004).

[27] A. I. Chichinin, T. Einfeld, K.-H. Gericke, J. Grunenberg, C. Maul, and L. Schäfer, Phys. Chem. Chem. Phys. **7**, 301 (2005).

[28] A. I. Chichinin, T. Einfeld, C. Maul, and K.-H. Gericke, Dokl. Phys. Chem. **402**, 96 (2005).

[29] A. I. Chichinin, C. Maul, and K.-H. Gericke, J. Chem. Phys. **124**, 224324 (2006).

[30] A. I. Chichinin, P. S. Shternin, N. Gödecke, S. Kauczok, C. Maul, O. S. Vasyutinskii, and K.-H. Gericke J. Chem. Phys. **125**, 034310 (2006).

[31] C. Maul, S. Kauczok, N. Gödecke, K.-H. Gericke, and R. Delmdahl, Physik Journal **6**, 2 (2007).

[32] A. Chichinin, T. Einfeld, C. Maul, and K.-H. Gericke, Rev. Sci. Instr. **73** 1856 (2002).

[33] S. Kauczok, N. Gödecke, A. I. Chichinin, M. Veckenstedt, C. Maul, and K.-H. Gericke, Rev. Sci, Instr. **80** 083301 (2009).

[34] A. I. Chichinin, S. Kauczok, K.-H. Gericke, and C. Maul, Int. Rev. Phys. Chem **28** 607 (2009).

[35] I. Ali, R Dörner, O. Jagutzki, S. Nüttgens, V. Mergel, L. Spielberger, K. Khayyat, T. Vogt, and H. Bräuning, Nucl. Instrum. Methods Phys. Res. B **149**, 490 (1999).

---

[36] O. Jagutzki, V. Mergel, K. Ullmann-Pfleger, L. Spielberger, U. Spillmann, R. Dörner, H. Schmidt-Böcking, Nucl. Instrum. Methods Phys. Res. B, **477**, 244 (2002).

[37] C. Romanescu, and H.-P. Loock, *J. Chem. Phys.* **127**, 124304-1 (2007).

[38] M. Poretskiy, A. I. Chichinin, C. Maul, and K.-H. Gericke, *PCCP*. **16**, 19741 (2014).

[39] J. E. Turner, *Phys. Rev.* **141**, 21 (1966).

6 Two- and three-photon absorption cross section measurement in case of ion-pair photodissociation of HCl by means of 3D Ion Imaging

Abstract: The process of photodissociation of HCl into an ion pair occurs after the absorption of three photons in the range 230 – 243 nm according to the REMPI scheme [2+1]. In order to quantitatively characterize the whole process as well as each radiating step the values of total three-photon absorption cross section, of the two-photon absorption cross section of the initial excitation step and the cross section of the third photon absorption leading to dissociation were measured in case of different vibronic states $V^1\Sigma^+$(v=8,9,10,11,12,13,14,15) or $E^1\Sigma^+$(v=0,1) excited after the absorption of two photons. For the measurements a new method based on three-dimensional (3D) Ion Imaging method was developed. It includes simultaneously counting the number of positive and negative photoions, measurement of the energy of the pulses of exciting radiation and characterization of spatial and temporal shape of these pulses. The theoretical part of the method demands the solution of the system of kinetics equations in order to link the absorption cross sections to the number of produced ions and to the number of photons in the radiation pulse. The results show a resonance-like behavior of the cross sections of each kind. The dependences of the two-photon cross section and the cross section of the third photon absorption on the excited vibronic state are «out-of-phase», demonstrating the maxima in case of $E^1\Sigma^+$(v=0) and $V^1\Sigma^+$(v=12) respectively. Finally the maximum of the total three-photon absorption cross section occurs in case of $V^1\Sigma^+$(v=12), showing that the step of the absorption of the third photon mainly defines the intensity of the process of ion pair production. Thus, one can control quantitatively the ion pair yield in the photodissociation of HCl molecule. The method of the cross sections measurement is shown to be almost universal. It can be applied to the characterization of multiphoton photodissociation of any molecule.

6.1 Introduction

The earliest studies of photodissociation were done already in the 30s of the 20th century [1,2,3,4,5]. The investigations of this time focused mainly on the identification of the primary products. For example Terenin and Popov in their work [1] observed the oppositely charged products. It was the first observation of the ion-pair channel of photodissociation. The first ideas about the mechanism of photodissociation process were formulated in the same time [6,7,8,9]. Later the characteristic electronic states of many molecules were assigned using the developed spectroscopic methods. Basing on the detailed knowledge of the states of parent species, the dynamics of photodissociation can be explained.

In a particular case of HCl the states involved in the photodissociation process have been monitored experimentally using photoelectron spectroscopy [10,11,12,13,14] and resonance enhanced multiphoton ionization (REMPI) technique [15,16,17,18,19,20,21,22,23,24]. The second electronically excited state $B^1\Sigma^+$ with two minima studied as well [16,17,18,23,24] results from an avoided crossing of the $E^1\Sigma^+$ Rydberg and the $V^1\Sigma^+$ state – the latter being itself the result of an avoided crossing of a valence state and the ion pair state asymptotically correlated with H^+ and Cl^- [25,26,27]. The investigation of HCl REMPI gave the information about the vibrational [19,20,21,23,24] and electron [18,28,29] spectroscopic feature of $B^1\Sigma^+$ state. As it has been observed the $B^1\Sigma^+$ state can be reached after the two-photon absorption at the wavelength in the region 230 – 243 nm.

$$\mathrm{HCl}(X^1\Sigma^+, v'') \xrightarrow{2h\nu} \mathrm{HCl}^*(B^1\Sigma^+, v') \qquad (6.1.1)$$

The subsequent absorption of third photon leads to the competing production of ionized HCl molecule or atoms. The ionized atomic products have been originally monitored by Spiglanin et al [17], and later by other groups [18,19,20,21]. Romanescu et al. [28,30] and Chichinin et al. [31,32] applied photoelectron and photoion imaging methods to identify the channels of HCl direct ionization with the production of vibrationally excited HCl^+:

$$\mathrm{HCl}^*(B^1\Sigma^+, v') \xrightarrow{h\nu} \mathrm{HCl}^+(X^2\Pi, v^+)+e^- \qquad (6.1.2)$$

After the absorption of an additional photon the molecular ion HCl^+ dissociates

$$\mathrm{HCl}^+(X^2\Pi, v^+) \xrightarrow{h\nu} \mathrm{H}^+ + \mathrm{Cl}(^2P) \qquad (6.1.3a)$$

$$\mathrm{HCl}^+(X^2\Pi, v^+) \xrightarrow{h\nu} \mathrm{H}(^2S) + \mathrm{Cl}^+ \qquad (6.1.3b)$$

A competing process of HCl fragmentation to neutral products occurs after the radiating transition from the state $B^1\Sigma^+$ to a superexcited state, from which the molecule undergoes the dissociation:

$$\mathrm{HCl}^*(B^1\Sigma^+, v') \xrightarrow{h\nu} \mathrm{HCl}^{**} \qquad (6.1.4a)$$

$$\mathrm{HCl}^{**} \longrightarrow \mathrm{Cl}+\mathrm{H}^* \qquad (6.1.4b)$$

$$\mathrm{HCl}^{**} \longrightarrow \mathrm{H}+\mathrm{Cl}^* \qquad (6.1.4c)$$

The photodissociation process with the formation of ion-pair was first found by Yencha et al. [33] as a result of the absorption of one photon with the energy 14.4-16.4 eV. They suggested, that after the excitation the molecule reaches the $^1\Sigma^+$ state, from which the system undergoes the non adiabatic transition to ion pair state $V^1\Sigma^+$ and finally dissociates. Hepburn et al. [34,35] obtained similar results using threshold ion pair production spectroscopy near 14.4 eV photon energy.

In case of the multiphoton process via $B^1\Sigma^+$ state, the ion pair production in HCl occurs also as a result of the absorption of the third photon, which populates the superexcited state, predissociating to the ion pair:

$$HCl^*(B^1\Sigma^+) \xrightarrow{h\nu} HCl^{**} \longrightarrow HCl^{**}(V^1\Sigma^+) \longrightarrow H^+ + Cl^- \tag{6.1.5}$$

C. Romanescu and H.-P. Loock [30] obtained the β parameter of the photoelectron distribution in case of ion pair photodissociation with the rotationless intermediate states equal to 2. This fact results in the Ω=0 symmetry of the superexcited state. The authors concluded, that the most probable states for the ion-pair dissociation channels are the $[A(^2\Sigma^+)\cdot\cdot 5s\sigma, 4d\sigma, \text{or } 5p\sigma]\ ^1\Sigma^+$ bound superexcited states.

As it was reviewed by Chichinin et al.[36], the number of systems, for which the dynamics of multiphoton photoprocesses was explained by means of imaging methods, is enormous. The absolute intensities of the two-photon process were obtained in some works [37,38,39,40,41,42,43,44,45,46,47]. However, it is the first step of the multiphoton processes under consideration. In turn the following steps with the photon absorption were not quantitatively characterized. Herein the values of the absorption cross sections of the following steps are necessary to perform the quantitative characterization of the multiphoton photodissociation and develop the investigation of their dynamics.

The processes in HCl and many other molecules include a two-photon step. The general theory of two-photon absorption was initially established by Göppert-Mayer in 1931 [48], while the first experimental information was given by Shiga and Imamura [49] in case of two-photon photoelectric emission from Cs_3Sb photocathode under irradiation of photons at 1.17 eV. Later basing on the second order perturbation theory the two-photon absorption cross section was theoretically evaluated in case of multiphoton ionization processes in H_2, CO, N_2, I_2, N_2O molecules and Kr, Xe, O atoms [37,38,43]. In contrast the experimental determination of two-photon absorption cross section observes certain difficulties of its realization. At first the attenuation of the laser beam because of the two-photon absorption is too weak to be measured directly. To solve this problem the population in the excited state has to be measured in an alternative way. The strong nonlinearity of the transition rate in the intensity introduces the second difficulty. One has to determine carefully spatial and temporal profile of the laser pulse in order to measure precisely the excitation cross section. The task of the determination of spatial profile in the area of its interaction with the molecules is complicated by the installation of the focusing lens. Due to the application of fluorescence depletion methods the first problem was solved and the measurement of the absolute values of two-photon excitation cross-section was done in case of H_2 molecule [39] as well as in case of Xe, Ba, O, N and F atoms [40,41,42,44,45,46,47].

In the current work the *quantitative* characterization of the process of the photodissociation of HCl molecule with the formation of ion pair is demonstrated. The process is monitored in case of a set of intermediate excited states $V^1\Sigma^+$(v=8,9,10,11,12,13,14,15) or $E^1\Sigma^+$(v=0,1) reached after the absorption of two photons. The values of three- and two-photon absorption cross section as well as the cross section of the third photon absorption, quantitatively describing the process of ion pair production, are measured by means of the method, discussed in detail below.

6.2 Experimental

6.2.1 The construction of the set-up

The double-arm imaging set-up used in the current work has been specially constructed for simultaneous detection of negative and positive ions, resulting from the photodissociation of molecules. It has been described in detail in recent publications [50,51]. Therefore the experimental set-up will be outlined only briefly, underlining the aspects important for the current discussion.

The set-up consists of two coaxial TOF spectrometers mounted together as a mirror reflection of each other. The acceleration regions (5cm) of both spectrometers consist of five electrodes each forming a common acceleration region of the double arm spectrometer. The acceleration regions are followed by the field drift regions (10cm). On both sides of the double-arm spectrometer commercial 3D imaging detectors are placed, consisting of the combination of a two stage microchannel plate (MCP) with a delay line anode (DL) (RoentDek) [52,53]. The acceleration region, the drift regions, and the detectors are separated from each other by grids. In a previous publication [51] it has been shown, that each grid reduces the number of ions flying through them by 20%. The processes on the grids leading to this reduction such as electron production or positive ion recharge are discussed elsewhere [51]. A pulsed nozzle (General Valve, Series 9 Pulsed Valve) introduces the molecular beam between the fifth and sixth electrodes of the common acceleration region at a right angle to the spectrometer axis. The whole set-up is placed inside a stainless steel vacuum chamber pumped by two turbomolecular pumps (Pfeiffer TMU 260 and Pfeiffer TMH 521 P), which are forepumped by a rotary vane pump filled with PFPE oil. The pressure in the vacuum chamber in case of a closed nozzle is 10^{-7} mbar, while it increases to 10^{-5} mbar when the nozzle is operating.

In the experiment pure HCl has been used in order to obtain a sufficiently large signal of negative chlorine ions even in case of low intensity channels of ion-pair photodissociation. HCl with a stagnation pressure of approximately 1 bar is expanded through the 400 μm orifice of the pulsed nozzle. The molecular beam is intersected by the laser beam perpendicular to it and to the spectrometer axis. UV laser radiation is the result of the dye laser (Nd:YAG pumped Scanmate 2, Coherent) output frequency doubled by a BBO crystal. Before entering the vacuum chamber the laser beam can be limited by a circular diaphragm, if a reduction of the laser energy is necessary. Under this condition the diaphragm will slightly diffract the beam. After the diaphragm the beam is focused by an f=0.3 m focus lens in order to obtain large enough photons concentration in the middle of the molecular beam. An UV light power meter measures the energy of the laser pulse E after the beam has passed the apparatus.

6.2.2 The time shape of the laser pulse

The time profile of the laser pulse is measured by means a fast detector. In Fig. 6.2.1 one can see that the fitting of the profile with the Gaussian does not give satisfying agreement. In contrast the fitting with the function

$$f(t) = A * exp\left(-\exp\left(-\frac{t-t_0}{\Delta t}\right) - \frac{t-t_0}{\Delta t} + 1\right) \tag{6.2.1}$$

results in significantly better agreement with the experimental time profile of the laser pulse.

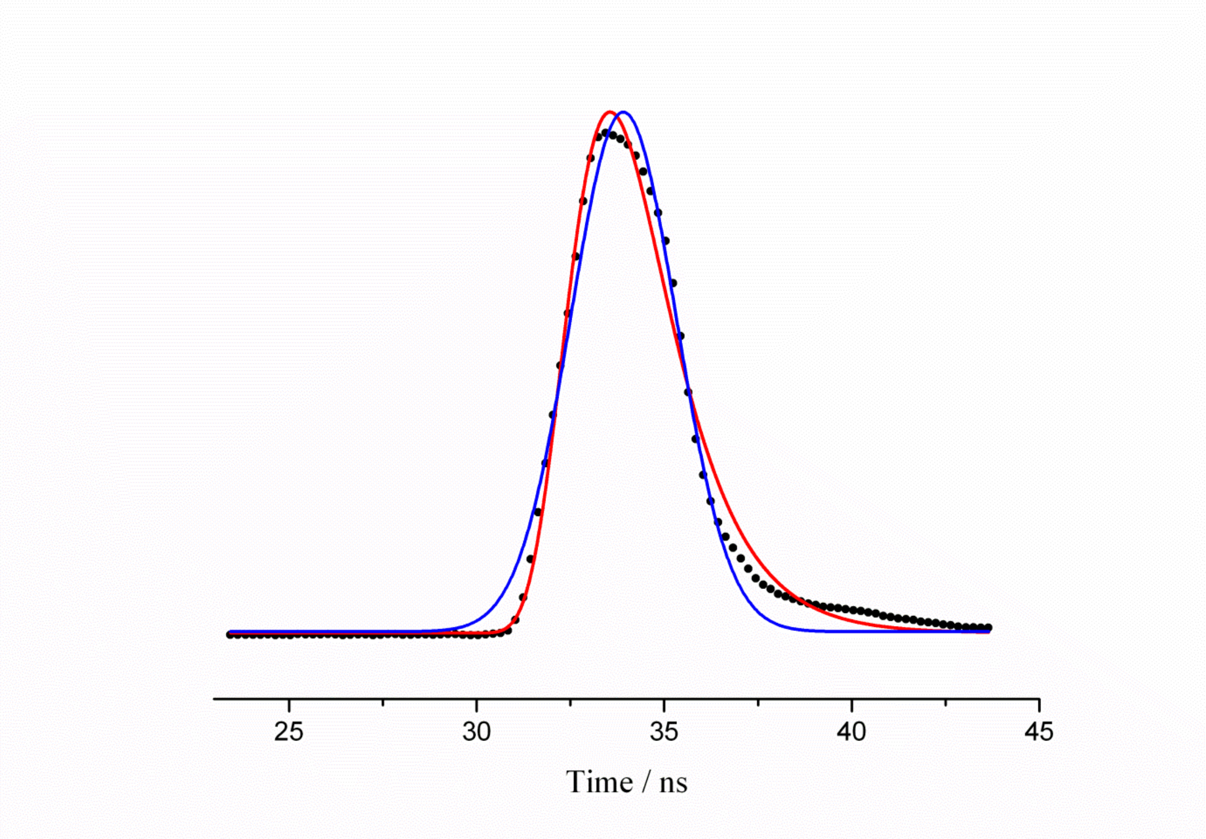

Fig. 6.2.1: The measured time profile of the laser pulse (black dots), its fitting by a Gaussian function (blue curve) and by the function (6.2.1) (red curve).

The function (6.2.1) has no physical meaning. Nevertheless the almost ideal reproduction of the experimental time profile as well as the convenient form of the dependence on *t* for the further formal treatment (Chapter 6.3), makes this function a sufficiently good representation of the time profile.

6.2.3 Principle of the ion number measurement

The positive and negative ions, produced from photodissociation and photoionization of HCl, fly in opposite directions and are projected onto the 3D Imaging detectors after passing the acceleration and drift region of the corresponding arm of the spectrometer. The eight signals from the four lines of the Delay Line are decoupled from the high DC voltage, differentially amplified by an eight channel differential amplifier (KSU EDL DLA800), recorded by a LeCroy 500 MHz oscilloscope (Waverunner 6050, Quad 5Gs/s) and finally analyzed by a special procedure of individual ion identification. This procedure and its limitations are in detail described in previous work [54]. Here only the initial steps are reported. The signals of the individual ion on the four lines are fitted by Gaussians in order to obtain peak centers and areas.

At reduced laser energies, when the number of ions projected on the detector per laser pulse does not significantly exceed 1 (experimental limit of individual ion identification procedure), the Imaging measurement gives its statistics, demonstrating the mean number of ions detected pro one laser pulse. Although theoretically the upper limit of the ion identification procedure by means of 3D Imaging is two ions per laser pulse, a number larger than one already introduces errors in the procedure. At moderate or high laser energies the number of ions projected on the detector per laser pulse significantly exceeds 1. As a result, the procedure of individual ion identification does not work properly and the measured mean number of ions detected per laser pulse is not a reliable value any more. Nevertheless, the ion number can be measured in another way by-passing the procedure of individual ion identification. The total peak area under the four signals of the Delay Line can be divided by the mean peak area under the signal of the individual ion obtained at reduced laser energy. As a result the number of ions detected per laser pulse is measured.

The detected number of ions is smaller than the number of initially produced ions because each grid in the spectrometer reduces the number of flying ions by 20%. In order to correctly obtain the number of produced ions per laser pulse the obtained number has to be corrected by a factor of 1.5625.

6.3 Theoretical basis

As it was mentioned above (section I) the mechanism of the three-photon photodissociation of HCl with the formation of the ion pair H^+ and Cl^- is:

$$\mathrm{HCl}\,(X^1\Sigma^+) \xrightarrow{2h\nu} \mathrm{HCl}^*(\,X^1\Sigma^+, v) \xrightarrow{h\nu} \mathrm{HCl}^{**} \longrightarrow \mathrm{HCl}^{**}(V^1\Sigma^+) \longrightarrow H^+ + Cl^-. \quad (6.3.1)$$

Its kinetics can be described in terms of the system of equations (6.3.2):

$$\frac{d}{dt}[X(r,x,t)] = -\widetilde{K}_2[X(r,x,t)], \quad (6.3.2a)$$

$$\frac{d}{dt}[B(r,x,t)] = \widetilde{K}_2[X(r,x,t)] - \widetilde{K}_3[B(r,x,t)], \quad (6.3.2b)$$

$$\frac{d}{dt}[C(r,x,t)] = \widetilde{K}_3[B(r,x,t)], \quad (6.3.2c)$$

This approach takes into account only the radiating step of the process (6.3.1), while the non-radiating steps are ignored. This assumption is justified because the characteristic times of the ignored processes are significantly smaller than the times of the described steps. As a result they occur immediately and can be excluded from the analysis. The system of equations (6.3.2) also assumes that the probability of the third photon absorption is small. That corresponds to experimental conditions where the laser power is small. If the laser power is increasing, the probability of a third photon absorption increases as well. Starting from a particular value, the second step of the process (6.3.1) becomes immediate, and the reaction rate constant K_3 formally can be estimated to be equal to zero.

The reaction rate constants in the system of equations (6.3.2) can be written as:

$$\widetilde{K}_2 = k_2 \Phi^2(r, x, t) \tag{6.3.3a}$$

$$\widetilde{K}_3 = k_3 \Phi(r, x, t) \tag{6.3.3b}$$

where Φ is the photon flux and k_2 and k_3 are two and one photon absorption cross-sections for the first and the second step of 6.3.1. Their dimensions are $\frac{photon}{cm^2 s}$, $\frac{cm^4 s}{photon^2}$ and $\frac{cm}{photon}$ respectively.

The photon flux in cylindrical coordinates with the reference point in the focus of the lens F is given by:

$$\Phi(r, x, t) = N_{h\nu} \frac{f(t)}{\Delta t} \frac{\Phi_0(r,x)}{\pi w^2(x)} \tag{6.3.4}$$

where Δt is the effective duration of the laser pulse, $N_{h\nu}$ represents the number of photons in the laser pulse and $w(x)$ is the effective radius of the laser beam depending on the coordinate x. The dimensionless function $f(t)$ describes the laser pulse time profile and $\Phi_0(r, x)$ represents the laser beam transverse profile.

In order to work with a dimensionless variable t' each equation of the system (6.3.2) can be multiplied by the factor Δt. In the left part this factor forms a new differential $dt' = dt/\Delta t$, while in the right part new dimensionless reaction rate constants can be introduced. The possibility to split the photon flux into time-dependent and spatial parts allows us to finally rewrite the reaction rate constants in the following way:

$$\Delta t \widetilde{K}_2 = K_2 f^2(t') \tag{6.3.5a}$$

$$\Delta t \widetilde{K}_3 = K_3 f(t') \tag{6.3.5b}$$

After this treatment the system (6.3.2) can be presented as:

$$\frac{d}{dt'}[X(r,x,t')] = -K_2 f^2(t')[X(r,x,t')], \tag{6.3.6a}$$

$$\frac{d}{dt'}[B(r,x,t')] = K_2 f^2(t')[X(r,x,t')] - K_3 f(t')[B(r,x,t')], \tag{6.3.6b}$$

$$\frac{d}{dt'}[C(r,x,t')] = K_3 f(t')[B(r,x,t')], \tag{6.3.6c}$$

Under the assumption, that the decrease of the number of molecules in the ground state X is negligible and at the limit $t' \to \infty$ the solution of the system is:

$$[X(r,z,+\infty)] \approx [X_0](1 - K_2/4) \tag{6.3.7a}$$

$$[B(r,z,+\infty)] \approx \frac{K_2[X_0]}{4}\left(1 - K_3\frac{5}{9} + K_3^2\frac{13}{72} + \cdots\right) \tag{6.3.7b}$$

$$[C(r,z,+\infty)] \approx \frac{K_2[X_0]}{4}\left(K_3\frac{5}{9} - K_3^2\frac{13}{72} + \cdots\right) \tag{6.3.7c}$$

It is easy to prove, that the solution satisfies the condition $[X] + [B] + [C] = [X_0]$ where $[X_0]$ is the initial particle density in the interaction volume of molecular and laser beams at *t=0*, i. e. before the laser are fired.

To calculate the number of molecules in the states *C* or *B* one needs to calculate the integrals of the corresponding concentrations over the spatial coordinates:

$$N_C = \int [C(r,x,+\infty)] 2\pi r dr dx = \int \frac{5K_2K_3[X_0]}{36} 2\pi r dr dx \tag{6.3.8a}$$

$$N_B = \int [B(r,x,+\infty)] 2\pi r dr dx = \int \frac{K_2[X_0]}{4} 2\pi r dr dx \tag{6.3.8b}$$

The final formulae, taking into account the exact expression of the dimensionless constants K_2 and K_3, are:

$$N_C = \frac{5\pi k_2 k_3 [X_0] N_{h\nu}^3}{36\Delta t} \int \left[\frac{\Phi_0(r,x)}{\pi w^2(x)}\right]^3 2r dr dx \tag{6.3.9a}$$

$$N_B = \frac{\pi k_2 [X_0] N_{h\nu}^2}{4\Delta t} \int \left[\frac{\Phi_0(r,x)}{\pi w^2(x)}\right]^2 2r dr dx \tag{6.3.9b}$$

The formula (6.3.9a) shows the dependence of the number of particles of one type, produced after the absorption of three photons, on the third power of the number of photons in the laser pulse. Both values N_C and N_B can be measured in the imaging experiment as it has been mentioned in the chapter 6.2. The limits of the imaging method application as well as the demands of the discussed kinetic model require the formula (6.3.9a) to be used in case of reduced laser energy. In this case both radiating steps are important and the value N_C describes the number of produced particles of one type (H^+, Cl^+, Cl^-).

The formula (6.3.9b) in turn specifies the relation between the number of excited molecules in the intermediate state B and the second power of the photons in the laser pulse. It is used to characterize the photodissociation at moderate or high energies, when the second radiating step is ignored. Since the state B is the intermediate step for all the photodissociation channels, one has to count the produced particles of all types to obtain the value N_B. Instead of individual ion counting the direct integration of the signals from the delay line is used (chapter 6.2).

From the measured number of ions and the values N_B or N_C one can calculate the absorption cross-sections k_2 and k_3. To obtain the cross-sections one needs to know the concentration $[X_0]$ and the value of the integral I_n:

$$I_n = \int \left[\frac{\Phi_0(r,x)}{\pi w^2(x)}\right]^n 2rdrdx \qquad , n = 2, 3 \tag{6.3.10}$$

6.4 The measurement of the initial concentration

The necessary value of the concentration $[X_0]$ is included in the expression for the angular distribution of molecular beam intensity $[X(\theta)]$, which in turn defines the gas flow(in amount of substance per unit) through the half-sphere:

$$Q = 2\pi v d^2 \int_0^{\pi/2} [X(\theta)] \sin\theta \, d\theta, \tag{6.4.1}$$

where v is the speed of the molecular beam, d is the distance from the nozzle to the intersection point of the molecular and the laser beams (d is the radius of the half-sphere as well). The flow Q can be measured by means of the well measured volume additionally connected before the nozzle. The final formula to obtain the concentration is:

$$[X_0] = \frac{9n_0}{2\pi v d^2} Q. \tag{6.4.2}$$

Where n_0 is the Loschmidt constant. The obtained value is $[X_0] = 6.1 \cdot 10^{16}\ cm^{-3}$.

6.5 Principles of calculation of the laser radiation density

The formula (6.3.10) gives the integral of the squared or cubed expression, defining the spatial structure of the laser beam, confined by the diaphragm and focused by a lens (Chapter 6.2).

It is assumed that the shape of the laser beam is Gaussian. The installed diaphragm with the radius of aperture r_0 diffracts the passing light. The diffraction theory based on the Huygens–Fresnel principle gives the universal way for the calculation of the field of the diffracted beam. Nevertheless in this work it will be more convenient to use another method by decomposing the diffracted beam into free space modes, using their orthogonality:

$$I(x') = u_D u_D^* = \sum_{p,q} C_p C_q L_p(2x'^2) L_q(2x'^2) exp\left(-2x'^2\right) \cos(\theta_{pq}) \frac{2}{\pi} \frac{r_0^2}{w^2(z)} \qquad (6.5.1)$$

$$x' = \frac{r}{w} \qquad (6.5.1a)$$

$$\theta_{pq} = 2(p-q) arctg\left(\frac{\lambda x}{\pi r_0^2}\right) \qquad (6.5.1b)$$

$$w(x) = r_0 \sqrt{1 + \left(\frac{\lambda x}{\pi r_0^2}\right)^2} \qquad (6.5.1c)$$

Here L_p – is a Laguerre polynomial of order p.

The focusing lens conserves the ground mode of the diffracted beam. The modes of higher order are converted into modes of the same order. The lens modifies the parameters of the modes, namely the radius of curvature *R(x)* and the radius of the beam *w(x)*, placing the waist of the beam (x=0) in the focal plane of the lens. As a result the intensity distribution in the area near the focus, where the photon concentration is sufficient to start the multiphoton process, is given by a formula analogous to the formula (6.5.1) with the corresponding replacement of parameters:

$$\Phi_0(r,x) = \frac{2}{\pi} \frac{r_d^2}{w^2(x)} exp\left(-2\frac{r^2}{w^2(x)}\right) \sum_{p,q} C_p C_q L_p\left(2\frac{r^2}{w^2(x)}\right) L_q\left(2\frac{r^2}{w^2(x)}\right) \cos(\theta_{pq}) \qquad (6.5.2)$$

where r_d is the radius of the waist in the focal plane. In the area of high photons concentration close to the focus $\cos(\theta_{pq})$ can be evaluated to be close to 1. Then the integration in (6.3.10) can be performed over the radius *r*:

$$I_n = A_n \frac{2^{n-1}}{\pi^{2n-1}} \frac{r_d^{2n}}{n} \int_{-\infty}^{+\infty} \frac{dx}{w^{4n-2}(x)}, \qquad n=2,3 \qquad (6.5.3)$$

Factor A_n is given by the integration of the Laguerre polynomial of the expression (6.5.2), or in other words it is defined by the free space modes taken into account to describe the diffraction of the beam. Because of the absence of technical possibility to measure the transverse profile of the beam the presence of different modes and their contribution to the beam can not be characterized. Nevertheless, the factor A_n can be calculated numerically for different upper limits of the indices p and q in the expression (6.5.2). For n=2 the value of A_2 in multi-mode case deviates from the value if only the ground mode is considered by not more than 5%, and for n=3 the difference between the values of A_3 increases to 10%. One can see that the difference in the values of A_n factors is not large and can easily be accounted for in the experimental errors of the determined absorption cross-sections. If only the ground mode is taken into account, all factors A_n are equal to 1.

Substituting (6.5.3) into (6.3.9) one obtains the following formulae to fit the dependence of the number of produced ions on the coordinate x (direction of laser radiation propagation) at a particular energy:

$$N_C(z) = A_C \frac{1}{\left(1+\left(\frac{\lambda x}{\pi r_d^2}\right)^2\right)^5} \tag{6.5.4a}$$

$$N_B(z) = A_B \frac{1}{\left(1+\left(\frac{\lambda x}{\pi r_d^2}\right)^2\right)^3} \tag{6.5.4b}$$

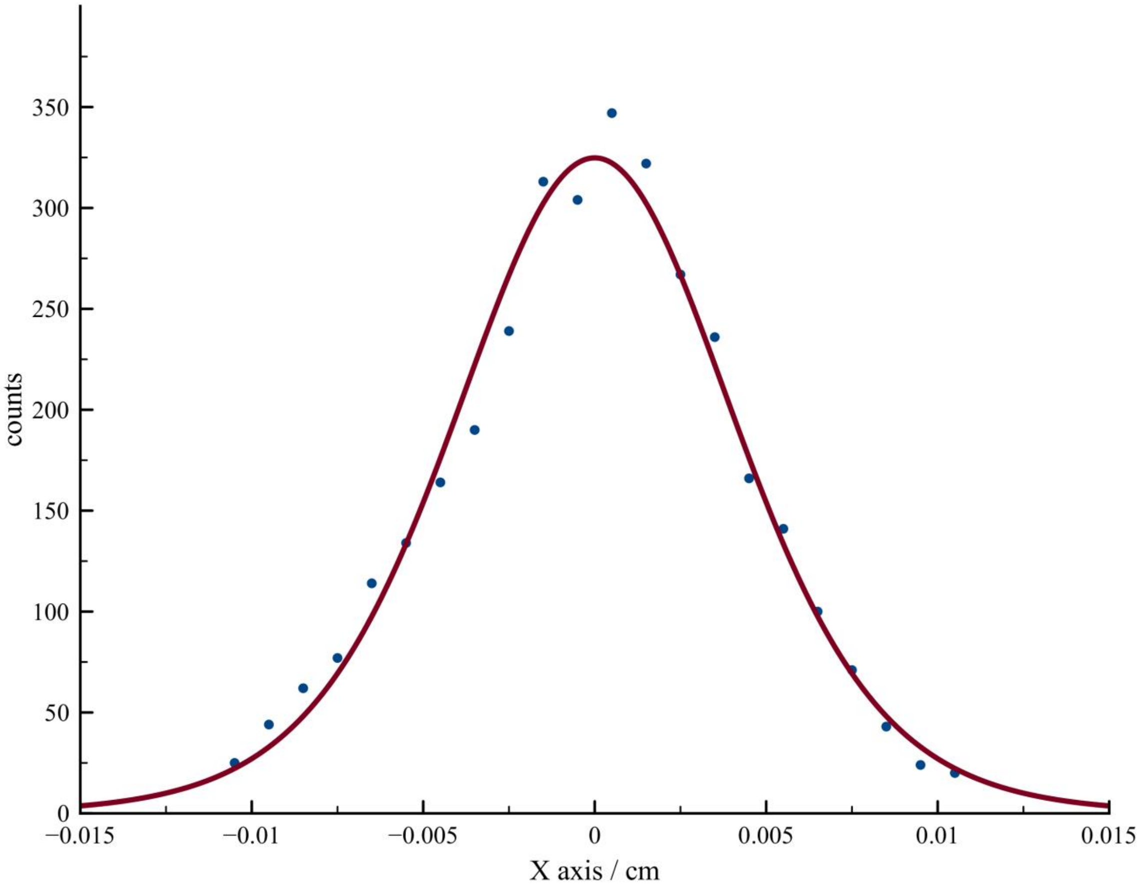

Fig. 6.5.1: The distribution of the number of produced HCl$^+$ ions along the laser beam propagation axis (x axis). The point x=0 corresponds to the focus of the lens. HCl$^+$ ions are the result of [2+1] REMPI of HCl molecule.

The coefficients A_C and A_B are collection of all constants of the corresponding formulae. HCl$^+$, being the product of photoionization, does not have a recoil velocity and impacts on the surface of the position sensitive detector at the same coordinates (x,y) as the ones, where it was produced. As a result the imaging of HCl$^+$ can be used to measure the number of produced ions depending on the *x* coordinate (Fig. 6.5.1):

The obtained dependence can be fitted by means of one of the formulae (6.5.4). As a result the value r_d is obtained as a fit parameter.

In order to reach the final result the integration over *x* in (6.5.3) is done by means of the residue of the complex subintegral function. The final formulae, describing the dependences of the number of produced ions or excited molecules in the state B on the laser energy, are:

$$N_C = \frac{175}{3744\pi^3}\frac{k_2 k_3 [X_0]}{\lambda r_d^2 \Delta t} N_{h\nu}^3 \tag{6.5.5a}$$

$$N_B = \frac{3}{32\pi}\frac{k_2 [X_0]}{\lambda \Delta t} N_{h\nu}^2 \tag{6.5.5b}$$

6.6 Results and discussion

The 3D imaging method allows one to obtain the angular distribution of negative ions of chlorine, produced in the ion-pair channel of photodissociation, and to measure their speed distribution. β anisotropy parameter values equal to 2 as well as most probable speeds equal to 465 m/s were obtained in case of all intermediate states. The β parameter demonstrates that only radiating transitions between states with $^1\Sigma^+$ symmetry are involved in the process of negative ion formation. The value of the most probable speed in turn proves that the ions were produced after the absorption of exactly tree photons.

The imaging results are evidence the ion-pair photodissociation origin of the detected particles. That is important because of many parasitic processes occurring in the double-arm set-up, described in detail before [51]. These processes consist mostly of secondary electron production on the surfaces of double-arm spectrometer parts. The detector, which monitors the negative ions, is extremely sensitive to electrons, which can impact on it at the same time as the chlorine negative photoions. As a result the 3D imaging procedure can be significantly affected if suitable precautions are not taken. The solution to the problem of such parasitic processes and how to obtain correct values of β anisotropy parameters and speeds of negative chlorine ion have been previously described in detail [51].

Ion counting results by means of the imaging method are presented in Fig 6.6.1 for different attenuated values of the energy in the laser pulse.

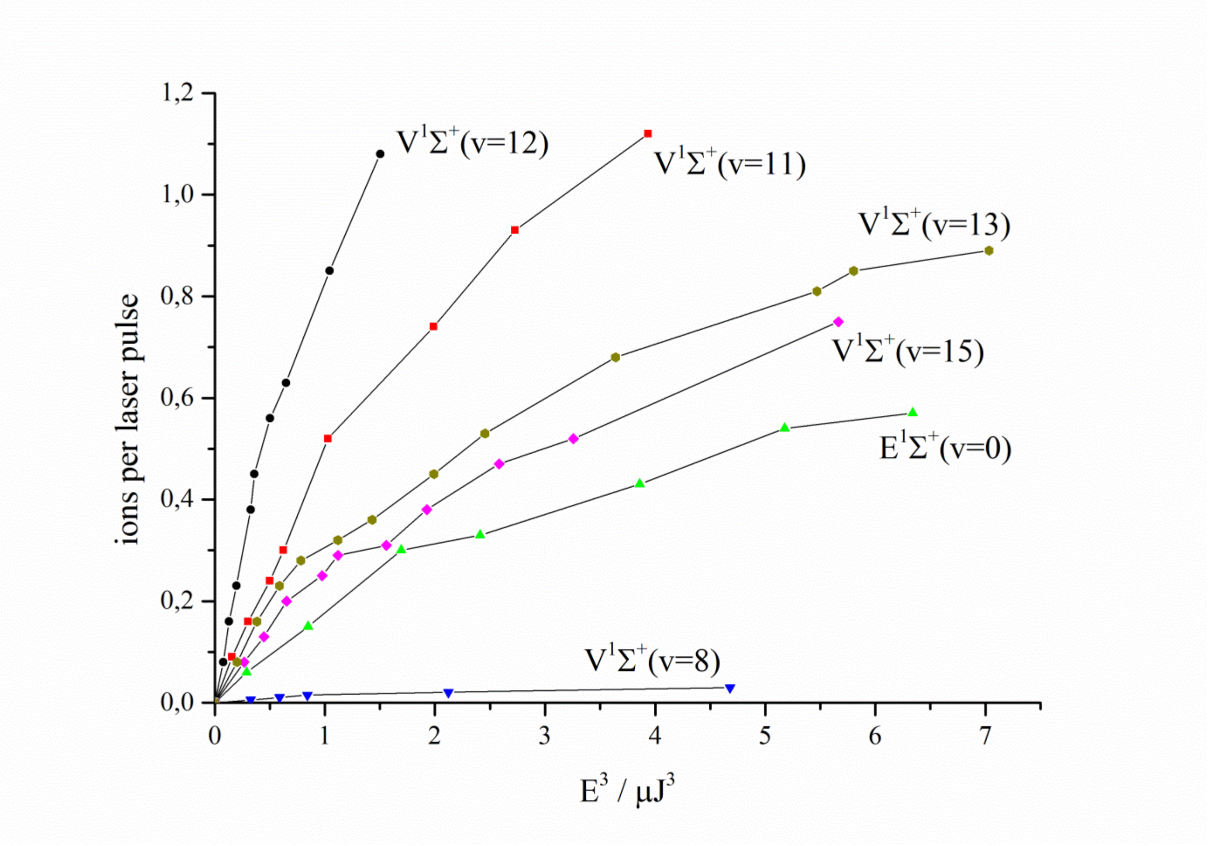

Fig. 6.6.1: Dependences of the number of produced negative ions (Cl^-) on the third power of laser pulse energy obtained in case of different intermediate excited states $V^1\Sigma^+$(v=8,11,12,13,15) and $E^1\Sigma^+$(v=0). The dependences in case of the states $V^1\Sigma^+$(v=9) and $E^1\Sigma^+$(v=0) are not presented. In these cases the numbers of produced ions are small and require a different scale for proper illustration of their power dependence.

The number of produced ions is plotted against the third power of the energy of laser pulse. If both radiating steps of ion-pair photodissociation are significant the dependence has to be linear. For all intermediate states the expected linearity can be observed only in a range of small values from 0 to 1µJ^3 of cubed laser pulse energy. In this range the formula (6.5.5a) can be used to fit the dependence and obtain the absolute value of the total three-photon absorption cross section (k_2k_3).

Its values for different intermediate states are summarized in the Table I. A resonance-like behavior of the cross section is observed. The results are in good agreement with the previous reports on the ion-pair channel of photodissociation [30,50]. The maximum is reached for the excitation of the intermediate state $V^1\Sigma^+$(v=12), while for the intermediate states $V^1\Sigma^+$(v=10,14) two minima are observed where the absorption cross section is equal to zero within experimental error. Less pronounced maxima were obtained in case of the negative ion production via $V^1\Sigma^+$(v=8,15). The absolute value of the three-photon absorption cross section in case of the intermediate state $E^1\Sigma^+$(v=0) agrees with the hypothetical resonant dependence on the vibrational levels of the intermediate electronic state $V^1\Sigma^+$. It confirms, that the $E^1\Sigma^+$(v=0) state is one of the vibrational levels of the electronic state $B^1\Sigma^+$.

	$V^1\Sigma^+$, v=8	$V^1\Sigma^+$, v=9	$E^1\Sigma^+$, v=0	$V^1\Sigma^+$, v=11	$V^1\Sigma^+$, v=12	$V^1\Sigma^+$, v=13	$E^1\Sigma^+$, v=1	$V^1\Sigma^+$, v=15
k_2k_3, $\frac{cm^6 s}{photon^3}$	$(1.26\pm 0.15)*10^{-71}$	$(4.3\pm 0.4)*10^{-72}$	$(3.2\pm 0.4)*10^{-70}$	$(9.1\pm 0.9)*10^{-70}$	$(2.1\pm 0.2)*10^{-69}$	$(6.9\pm 0.8)*10^{-70}$	$(2.0\pm 0.3)*10^{-72}$	$(7.1\pm 0.8)*10^{-70}$
k_2, $\frac{cm^4 s}{photon^2}$	$(1.1\pm 0.1)*10^{-54}$	$(1.48\pm 0.08)*10^{-54}$	$(2.40\pm 0.07)*10^{-53}$	$(1.24\pm 0.05)*10^{-53}$	$(1.03\pm 0.04)*10^{-53}$	$(3.72\pm 0.15)*10^{-54}$	$(5.68\pm 0.01)*10^{-55}$	$(6.1\pm 0.2)*10^{-54}$
k_3, $\frac{cm^2}{photon}$	$(1.08\pm 0.15)*10^{-17}$	$(2.9\pm 0.3)*10^{-18}$	$(1.36\pm 0.15)*10^{-17}$	$(7.4\pm 0.8)*10^{-17}$	$(2.1\pm 0.2)*10^{-16}$	$(1.9\pm 0.2)*10^{-16}$	$(3.6\pm 0.5)*10^{-18}$	$(1.16\pm 0.15)*10^{-16}$

TABLE I: Absolute values of the three-photon absorption cross section (k_2k_3), two-photon absorption cross section (k_2) and of the cross section of the third photon absorption (k_3). The value k_2k_3 characterizes the efficiency of ion-pair production, while the values of k_2 and k_3 characterizes the intensity of two-photon absorption and absorption of the third photon.

At higher pulse energies than approximately 1μJ the dependence of the number of produced ions does not increase with the third power of number of photons, because the third photon absorption step is saturated. The number of produced ions is essentially determined by the initial two-photon absorption step. Since the two-photon absorption step is common for all the channels of photodissociation or photoionization, it is necessary to count the number of all the positive ions in dependence on the energy of the laser pulse in order to measure the two-photon absorption cross-section. This introduces the necessity to monitor all the produced particles, and the use of the 3D Imaging method as described in Chapter 6.2 becomes inappropriate. Moreover the further increase of the laser pulse energy can lead to the number of ions impacting on the surface of detector, which significantly exceeds 1 per pulse. These facts demand the use of another method of ion counting, based on the direct measurement of signals from the Delay Line. Because of the saturation of the third photon absorption step, one can expect a quadratic dependence of the number of produced positive ions on the laser pulse intensity. As a result the ion number is plotted against the squared number of photons in the laser pulse (Fig 6.6.2). As before, no signals were detected in case of the intermediate state $V^1\Sigma^+$(v=10,14). The fitting of the obtained linear dependences gives the absolute values of two-photon absorption cross sections for all the intermediate states (Table I). The dependence of the two-photon cross section is very similar to the case of three-photon absorption cross section measurement. Nevertheless, it differs in the position of the maxima. The values of the two-photon absorption cross section have an absolute maximum for the intermediate state $E^1\Sigma^+(v=0)$. The zero values in case of intermediate states $V^1\Sigma^+(v=10,14)$ are obtained once again. Less pronounced maxima are observed for the states $V^1\Sigma^+(v=9,15)$.

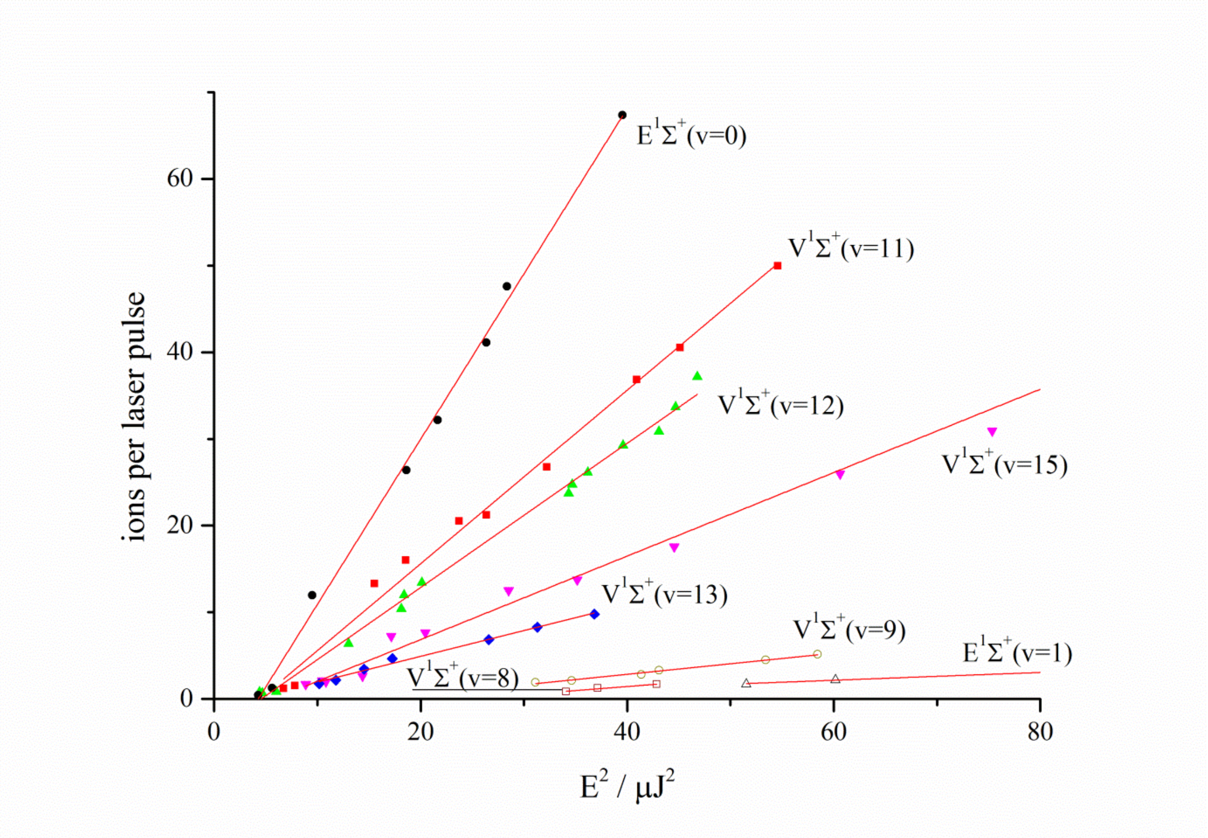

Fig. 6.6.2: Dependences of the number of produced positive ions (H^+, Cl^+ and HCl^+) on the second power of laser pulse energy obtained for different intermediate excited states $V^1\Sigma^+(v=8,9,11,12,13,15)$ and $E^1\Sigma^+(v=0,1)$.

The analysis of the intensity of the ion-pair channel of photodissociation can be done starting from the two-photon absorption step. In the simplest model this step can be discussed in the same way as a one-photon absorption step. Then the intensities of the transition from the ground state $X^1\Sigma^+(v=0)$ to an excited vibronic state $V^1\Sigma^+(v=8,9,10,11,12,13,14,15)$ or $E^1\Sigma^+(v=0,1)$ can be obtained from Franck-Condon factors, i.e. from the overlap between the vibrational wave functions of the initial and final states.

The $X^1\Sigma^+$ ground state is characterized by an equilibrium internuclear distance of r_X=1.275Å. The vibrational wave function corresponding to the vibrational ground state (v''=0) is localized near this value. In contrast the minimum of the outer well of the excited state $B^1\Sigma^+$ lies at an internuclear distance of r_B=2.51Å. As a result the vibrational wavefunctions corresponding to small vibrational quantum numbers v' of the $B^1\Sigma^+$ state are localized exclusively in its outer well and have zero or very weak overlap with the vibrational wavefunction of the ground state. The overlap increases with the vibrational quantum number v' of the excited electronic state. The absolute values of the two-photon cross sections measured in the current work were found for the quantum numbers 8 and 9, i.e. in case of the excitation to the levels $V^1\Sigma^+$(v=8,9). However, in case of the excited state $V^1\Sigma^+$(v=10) the cross section is equal to zero which can not be explained by the Franck-Condon principle. The most probable explanation is that the vibrational wavefunction of the state $V^1\Sigma^+$(v=10) occasionally has a zero overlap with all corresponding wavefunctions of the superexcited states, being a gateway states for the different channel of photodissociation.

According to Green et al. the potential barrier of the double minimum state $B^1\Sigma^+$ occurs just above the level v=10 of the $V^1\Sigma^+$ state. As a result the next level of the state $B^1\Sigma^+$, which is also labeled $E^1\Sigma^+$(v=0), lies above the barrier and is localized in the whole range of internuclear distances of the $B^1\Sigma^+$. Since the energy of this state is very close to the barrier energy its vibrational wavefunction has a slightly unusual form, schematically shown in Fig. 6.6.3.

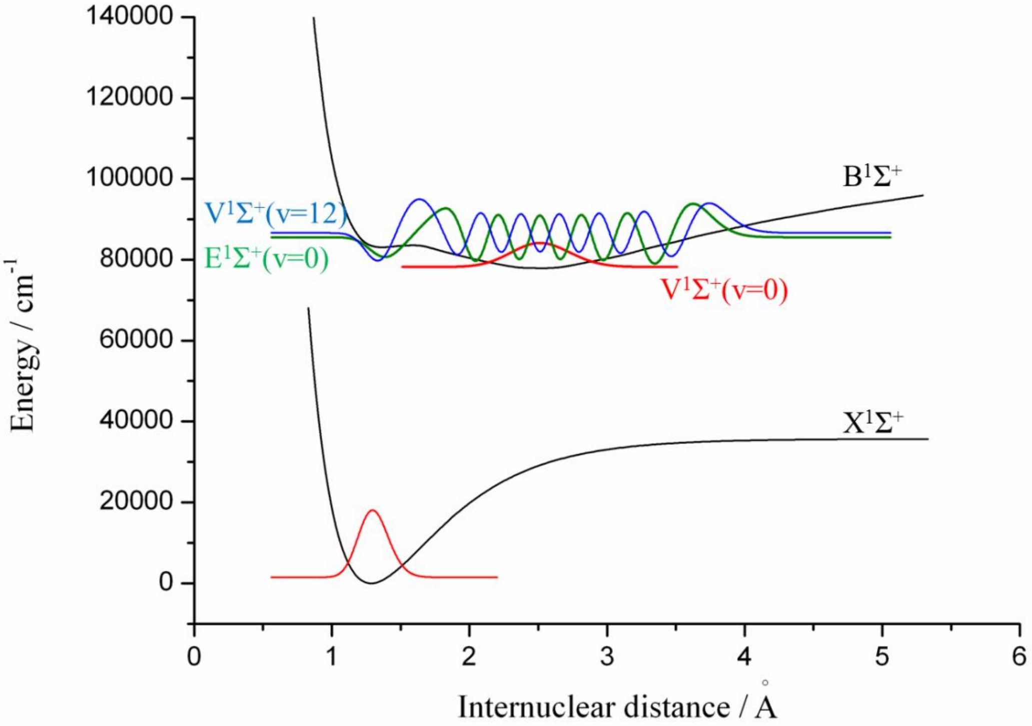

FIG. 6.6.3: Schematic representation of the wavefunction of vibrational levels of $B^1\Sigma^+$ state ($V^1\Sigma^+$(v'=0) – red curve, $V^1\Sigma^+$(v'=12) – blue curve and $E^1\Sigma^+$(v'=0) – green curve) and of the ground state $X^1\Sigma^+$(v''=0).

One can expect that the overlap of such a wavefunction with the wavefunction of the ground state is large. This is confirmed by the maximal measured cross section. The wavefunctions of the next levels of $B^1\Sigma^+$ state, i.e. $V^1\Sigma^+$(v'=11,12,13,14,15) are described by a standard oscillating behavior of the wavefunctions. The decreasing cross sections imply that the overlap of these wavefunctions has to decrease with the increasing vibrational quantum number.

As soon as the first node of the vibrational wavefunction of the upper $V^1\Sigma^+$ state coincides with the equilibrium internuclear distance r_X (the maximum of the vibrational wavefunction) of the $X^1\Sigma^+$ ground state, the contribution in the overlap integral from the internuclear distances smaller than r_X are compensated by the contributions of those internuclear distances larger than r_X, resulting in an overall zero value. The experiment shows that this situation is reached for the upper state $V^1\Sigma^+$(v'=14). In case of the next level v'=15, the value of the cross section increases again.

On the basis of the measured values of three- and two-photon cross section the values of the cross sections of the third photon absorption (Table I) can be obtained for all intermediate states with the exception of $V^1\Sigma^+$(v'=10,14), where the absence of signal of all possible ions inhibits the analysis. A comparison of the cross section of the third photon absorption with the other two cross sections can be performed by comparing the relative values of the cross sections (Fig. 6.6.4). One can see that the shape of the dependence of the absolute value of the third photon absorption cross section on the vibronic state v' is very close to the shape of the dependence of the total three-photon absorption cross section. Nevertheless their behavior significantly differs for $V^1\Sigma^+$(v'=8,13,15) intermediate states: the relative values of the third photon absorption cross section are much larger than the ones for the total three-photon cross section. In contrast the difference with the dependence in case of two-photon absorption cross section is generally quite strong. For example for the intermediate state $E^1\Sigma^+$(v'=0), where the two-photon absorption cross section reaches a maximum, one of the smallest values of the third photon absorption cross section is observed. Although the cross section of the third photon can not be obtained in case of the intermediate state $V^1\Sigma^+$(v'=10), one can expect a vanishing value for this cross section. This partially confirms the hypothesis that the absence of all signals can be explained by the impossibility to reach any superexcited state from $V^1\Sigma^+$(v'=10). At the same time it is difficult to evaluate the cross section for intermediate state $V^1\Sigma^+$(v'=14).

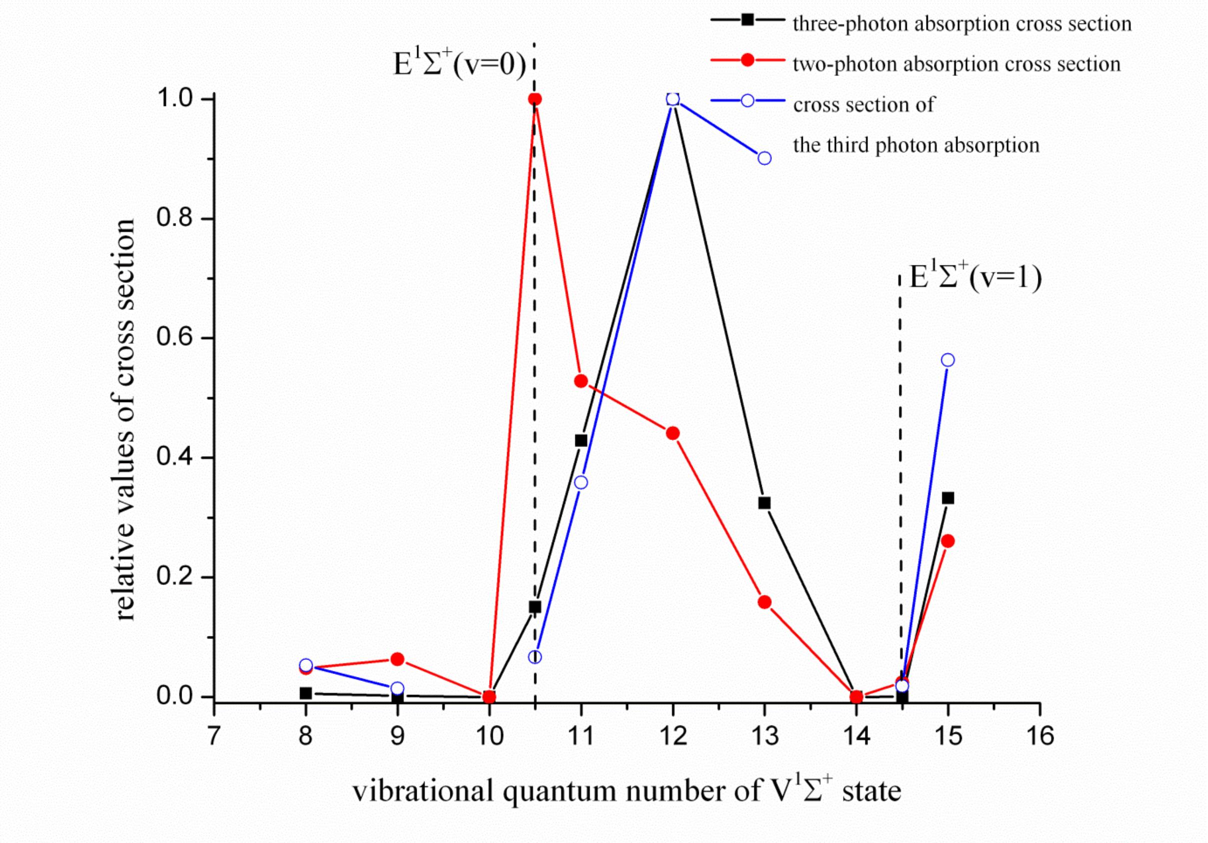

Fig. 6.6.4: Relative values of the three-photon (black dots), two-photon (red dots) absorption cross sections and the cross section of the third photon absorption (blue dots) in case of different intermediate excited states $V^1\Sigma^+$(v'=8,9,10,11,12,13,14,15) and $E^1\Sigma^+$(v'=0,1). The values corresponding to the states $E^1\Sigma^+$(v'=0,1) are presented between the values corresponding to the states $V^1\Sigma^+$(v'=10,11) and $V^1\Sigma^+$(v'=14,15), because of the position of these state on the energy scale.

The «out-of-phase» behavior of the two-photon cross section and the cross section of the third photon absorption shows that the Franck-Condon region of the two-photon transition in the first step does not coincide with that of the one-photon transition in the second step. Romanescu and Loock supposed that the Franck-Condon region of the latter is located in the outer well of the $B^1\Sigma^+$ and centered at 2.2 Å [30].

Our results show that the step of absorption of the third photon is crucial in the process of ion pair production. It limits this channel of photodissociation in case of the intermediate state $E^1\Sigma^+$(v'=0), which is favorable for two-photon excitation, while the ion-pair production via $V^1\Sigma^+$(v'=12,13) reaches the highest intensities although the corresponding two-photon cross section has dropped to about half of its maximum value for $E^1\Sigma^+$(v'=0).

6.7 Conclusion

This article shows that the application of 3D Ion Imaging is not limited to the study the dynamics of photoprocesses. The example of ion-pair photodissociation of HCl demonstrates that the method as well as the apparatus can be used also for quantitative characterization of photoprocesses. The intensities of both transition steps in the HCl molecule (two- and one-photon) involved in the overall three-photon absorption process leading to the formation of an ion pair, were characterized. For this purpose two- and three-photon absorption cross sections were determined utilizing a kinetic model of the photodissociation process. Since this model of a [2+1] photoprocess is almost universal, it can be applied for any system under consideration with the same scheme of photon absorption. A system fragmenting according to another scheme can also be analyzed by the same principles after some modification of the kinetic model.

The absolute values of the three- and two-photon absorption cross sections as well as the cross section of the third photon absorption were measured in case of ion-pair photodissociation via a comprehensive set of intermediate states $V^1\Sigma^+$(v'=8,9,10,11,12,13,14,15) and $E^1\Sigma^+$(v'=0,1). The data on three-photon absorption cross sections confirm the previous observation, showing the channel via $V^1\Sigma^+$(v'=12) to be the most intense one. However, the intermediate state dependencies of the two-photon absorption cross section and of the third photon absorption cross section demonstrate an «out-of-phase» behavior with maxima in case of $E^1\Sigma^+$(v'=0) and $V^1\Sigma^+$(v'=12) respectively. The latter maximum coincides with the maximum of the production of ion pairs. The analysis of the dependences of the cross sections of different kinds on the intermediate state shows that the step of the third photon absorption mainly defines the intensity of the ion-pair channel of photodissociation of HCl. The zero production of ion pairs, observed in case of the states $V^1\Sigma^+$(v'=10,14), are most likely limited by one-photon step in case of $V^1\Sigma^+$(v'=10) and by the two-photon step for $V^1\Sigma^+$(v'=14).

6.8 References

---

[1] A. Terenin and B. Popov, *Phys. Z.* Sowjetunion 2299 (1932).
[2] G. Von Elbe, *J. Am. Chem. Soc.* **55**, 62 (1933).
[3] A. Terenin, H. Neujmin, *Nature* **134**, 255 (1934).
[4] P. K. Sen-Gupta, *Nature* **136**, 513 (1935).
[5] Y. Hukomoto, *J. Chem. Phys.* 3, 164 (1935).
[6] R. G. W. Norrish, *Nature* **141**, 1138 (1938).
[7] E. Bergman, R. Samuel, *Nature* **141**, 832 (1938).
[8] E. Bergman, R. Samuel, *Nature* **142**, 919 (1938).
[9] E. Bergman, R. Samuel, *J. Org. Chem* **6**, 1 (1941).
[10] P. Natalis, P. Pennetreau, L. Longton, and J.E. Collin, *Chem. Phys.* **73**, 191 (1982).

---

[11] S. Svensson, L. Karlsson, P. Baltzer, B. Wannberg, U. Gelius, and M. Y. Adam, *J. Chem. Phys.* **89**, 7193 (1988).

[12] H. Frohlich, P. M. Guyon, and M. Glass-Maujean, *J. Chem. Phys.* **94**, 1102 (1991).

[13] A. J. Yencha, A. J. Cormack, R. J. Donovan, A. Hopkirk, and G. C. King, *Chem. Phys.* **238**, 109 (1998).

[14] D. S. Ginter and M. L. Ginter, *J. Mol. Spectrosc.* **90**, 177 (1981).

[15] S. Arepalli, N. Presser, D. Robie, and R. J. Gordon, *Chem. Phys. Lett.* **118**, 88 (1985).

[16] R. Callaghan, S. Arepalli, and R. J. Gordon, *J. Chem. Phys.* **86**, 5273 (1987).

[17] T. A. Spiglanin, D. W. Chandler, and D. H. Parker, *Chem. Phys. Lett.* **137**, 414 (1987).

[18] E. de Beer, B. G. Koenders, M. P. Koopmans, and C. A. de Lange, *J. Chem. Soc., Faraday Trans.* **86**, 2035 (1990).

[19] D. S. Green, G. A. Bickel, and S. C. Wallace, *J. Mol. Spectrosc.* **150**, 354 (1991).

[20] D. S. Green, G. A. Bickel, and S. C. Wallace, *J. Mol. Spectrosc.* **150**, 388 (1991).

[21] D. S. Green, G. A. Bickel, and S. C. Wallace, *J. Mol. Spectrosc.* **150**, 303 (1991).

[22] Y. Xie, P. T. A. Reilly, S. Chilukuri, and R. J. Gordon, *J. Chem. Phys.* **95**, 854 (1991).

[23] D. S. Green and S. C. Wallace, *J. Chem. Phys.* **96**, 5857 (1992).

[24] A. Kvaran, A. Logadottir, and H. Wang, *J. Chem. Phys.* **109**, 5856 (1998).

[25] M. Bettendorff, S. D. Peyerimhoff, and R. J. Buenker, *Chem. Phys.* **66**, 261 (1982).

[26] E. F. Dishoek, M. C. van Hemert, and A. Dalgarno, *J. Chem. Phys.* **77**, 3693 (1982).

[27] K. P. Lawley, and R. J. Donovan, *J. Chem. Soc. Faraday Trans.* **89**, 1885 (1993).

[28] C. Romanescu, S. Manzhos, D. Boldovsky, J. Clarke, and H.-P. Loock, *J. Chem. Phys.* **120**, 767 (2004).

[29] S. Manzhos, C. Romanescu, H.-P. Loock, and J. G. Underwood, *J. Chem. Phys.* **121**, 11802 (2004).

[30] C. Romanescu, and H.-P. Loock, *J. Chem. Phys.* **127**, 124304-1 (2007).

[31] A. I. Chichinin, C. Maul, and K.-H. Gericke, *J. Chem .Phys.* **124**, 224324 (2006).

[32] A. I. Chichinin, P. S. Shternin, N. Gödecke, S. Kauczok, C. Maul, O. S. Vasyutinskii, and K.-H. Gericke, *J. Chem. Phys.* **125**, 034310 (2006).

[33] A. J. Yencha, D. Kaur, R. J. Donovan, A. Kvaran, A. Hopkirk, H. Lefebre-Brion, and F. Keller, *J. Chem. Phys.* **99** 4986 (1993).

[34] Q. J. Hu, T. C. Melville, and J. W. Hepburn, *J. Chem. Phys.* **119**, 8938 (2003).

[35] A. G. Suits, and J. W. Hepburn, *Annu. Rev. Phys. Chem.* **57**, 431 (2006).

[36] A. I. Chichinin,S. Kauczok, K.-H. Gericke, and C. Maul, *Int. Rev. Phys. Chem.* **28**, 607 (2009).

[37] W. K. Bischel, J. Bokor, D. J. Kligler, and C. K. Rhodes, *IEEE J. Quant. Electr.* **QE15**, 380 (1979).

[38] J. Bokor, J. Zavelovich, and C. K. Rhodes, *Phys. Rev.* **A21**, 1453 (1980).

[39] J. D. Buch, D. C. Robie, A. P. Hichman, D. J. Bamford, and W K Bischel, *Phys. Rev.* **A39**, 3832 (1989).

[40] S. Kroll, and W. K. Bischel, *Phys. Rev.* **A41**, 1340 (1990).

[41] N. A. Cherepkov, A. Yu. Elizarov, *J. Phys. B: At. Mol. Opt. Phys.* **24**, 4169 (1991).

[42] Y. I. Huang, and R. J. Gordon, *J. Chem. Phys.* **97**, 6363 (1992).

[43] R. P. Saxon, and J. Eichler, *Phys. Rev.* **A34**, 199 (1986).

[44] D. J. Bamford, L. E. Jusinski, and W. K. Bischel, *Phys. Rev.* **A34**, 185 (1986).

[45] D. J. Bamford, M. J. Dyer, and W. K. Bischel, *Phys. Rev.* **A36**, 3497 (1987).

[46] D. J. Bamford, R. P. Saxon, L. E. Jusinski, J. D. Buck, and W. K. Bischel, *Phys. Rev.* **A37**, 3259 (1988).

[47] S. F. Adams, and T. A. Miller, *Chem. Phys. Lett.* **295**, 305 (1998).

[48] M. Göppert-Mayer, *Ann. Phys.* **5**, 273 (1931).

[49] F. Shiga, S. Imamura, *Phys. Lett. A*, **25A**, 706 (1967).

[50] M. Poretskiy, A. I. Chichinin, C. Maul, and K.-H. Gericke, *PCCP*. **16**, 19741 (2014).

[51] M. Poretskiy, A. I. Chichinin, C. Maul, and K.-H. Gericke, *to be published*

[52] I. Ali, R Dörner, O. Jagutzki, S. Nüttgens, V. Mergel, L. Spielberger, K. Khayyat, T. Vogt, and H. Bräuning, *Nucl. Instrum. Methods Phys. Res. B* **149**, 490 (1999).

[53] O. Jagutzki, V. Mergel, K. Ullmann-Pfleger, L. Spielberger, U. Spillmann, R. Dörner, H. Schmidt-Böcking, *Nucl. Instrum. Methods Phys. Res. B*, **477**, 244 (2002).

[54] A. I. Chichinin, T. Einfeld, C. Maul, and K.-H. Gericke, *Rev. Sci. Instrum.* **73**, 1856 (2002).

7 **Acknowledgments**

I am very grateful to my mentor Prof. Dr. Karl-Heinz Gericke for the opportunity to do PhD work in the challenge field of Ion Imaging, covering many disciplines of the modern physical and chemical science. His positive inspiration and valuable advice help me to orient in the forest of pure science and find the right way.

I would like to thank Dr. Christof Maul for his participation in the collective mind, searching the answer for the question, what is happening in HCl molecule. You offer me a lot of very useful ideas in all aspects of my work and is a perfect proof reader, teaching the wisdoms of scientific writing. Christof is the only person, who can speak with me German more than 15 minutes, except the students (but they have no choice).

Charly and Christof, I will never forget your help in extremely complicated problems with visa for Maria.

Alexey Chichinin I would like to thank for the very productive collaboration, for many fascinating discussions of the scientific questions. I am very grateful for all the aspects of theoretical knowledge and experimental skills, which I learned from you. I hope that together we became the two “mirrors” of a “laser resonator”, which illuminates the question of ion pair production in HCl.

Frau Simone Lecher I thank for her great help in all complicated administrative problems. She began to help me with the documents even before I came to Braunschweig. Here I almost forgot, how complicated can be working with documents..

Special thanks to Meinhard Schilling and to all IGSM members for the possibility to learn new aspects of science and to discuss my PhD work under new unexpected angles.

To the whole laser chemistry group: to the current members and the former ones. It is impossible to overestimate how important is to be a part of such a friendly group and work everyday with so nice and helpful people.

I wish to thank all the students, who made their Studienarbeit under my control. Explaining all the stuff to you I finally understood what I was explaining. Special “thanks” to Nicole Teschmit. She was my first student and later she shared the first problems of negative ions detection.

Most important, I would like to thank my wife Maria, my son Georgii, my parents Sergei Poretsky and Elena Poretckaia for their support, understanding and patience, while I was too

thoughtful, reflecting about HCl excitation. I would like to thank my brother Alexander, who was anytime my best friend. All you are the sense of my life and my best motivation. I dedicate this thesis to you!

CURRICULUM VITAE

PERSONAL INFORMATION

Name	**MIKHAIL, PORETSKIY**
Address	**38126 ACKERSTR.63, BRAUNSCHWEIG, DEUTSCHLAND**
Telephone	**01515 2040891**
E-mail	**mikhail.poretskiy@gmail.com**
Nationality	Russian
Date of birth	06.03.1986

WORK EXPERIENCE

April 2010 – till now
Research Associate at the Institute of physical and chemical Chemistry, Technical University, Braunschweig
October 2009 – December 2009
Engineer in Saint-Petersburg State University

EDUCATION AND TRAINING

2007 – 2010
Saint-Petersburg State University, Master of Science, Physics

2003 – 2007
Saint-Petersburg State University, Bachelor of Science, Applied Physics and Mathematics

1992 – 2003
392 Language school, Saint-Petersburg

List of publications

Conference publications:

1) Poretskiy, M., Chichinin, A.I., Maul, C. & Gericke, K.-H.: Probabilities for 2-and 3-photon absorption, ion pair channel (H^++Cl^-) in REMPI of HCl, and emission from metal surface of e^-, H^-, and HCl^- ions under the bombardment by H^+, Cl^+, and HCl^+ ions. (Vortrag) 29. STEREODYNAMICS 2014, St. Petersburg (2014).

2) Poretskiy, M., Chichinin, A.I., Maul, C. & Gericke, K.-H.: Two- and three-photon absorption cross section measurement in case of HCl photoionization and photodissociation by means of 3D-imaging method. (Poster) 78. STEREODYNAMICS 2014, St. Petersburg (2014).

3) Poretskiy, M., Chichinin, A.I., Maul, C. & Gericke, K.-H.: Surface scattering of H^- and HCl^- ions, resulting from the recharge of H^+ and HCl^+. (Poster) 78. STEREODYNAMICS 2014, St. Petersburg (2014).

4) Maul, C., Poretskiy, M., Chichinin, A. & Gericke, K.-H.: H^+ + Cl^-: Photoion pair production in HCl studied by bipolar three-dimensional (3D) photoion pair imaging. (Poster) 184. DPG-Frühjahrstagung, Berlin (2014).

5) Poretskiy, M., Chichinin, A., Maul, C. & Gericke, K.-H.: Negative ion imaging resulting from HCl photodissociation. (Poster). DPG-Frühjahrstagung, Hannover (2013).

6) Poretskiy, M., Veckenstedt, M., Maul, C. & Gericke, K.-H.: HBr photodissociation analysis as the calibration of two-color 3D velocity map imaging setup. (Poster) 152. “MOLECULAR PHOTONICS” dedicated to academician A.N. Terenin, Repino (2012).

7) Poretskiy, M., Veckenstedt, M., Maul, C. & Gericke, K.-H.: Experimental calibration of a 3D velocity map imaging setup using HBr photodissociation. (Poster) 24. Summer School of metrology 2012, Burg Warberg (2012).

8) Veckenstedt, M., Poretskiy, M., Maul, C. & Gericke, K.-H.: 3D velocity mapping of the Hydrogen atom formation from the 193 nm photodissociation of borazine via (2+1)-REMPI. (Poster) 139. DPG-Frühjahrstagung, Stuttgart (2012).

9) Poretskiy, M., Veckenstedt, M., Maul, C. & Gericke, K.-H.: Experimental calibration of a 3D Velocity map imaging setup using HBr photodissociation. (Poster) 139. DPG-Frühjahrstagung, Stuttgart (2012).

10) Veckenstedt M., Rakhymzhan, A., Poretskiy, M., Kauczok, S., Chichinin A.I., Goedecke, N., Maul C. & Gericke, K.-H.: 3D Velocity Map Imaging: Apparatus Details and Application. (Poster). ICONIC Training School, Freiburg (2010.)

11) Maul, C., Poretskiy, M. & Rakhymzhan, A.: N_2O van der Waals complex detection on Rydberg Transition in the ultraviolet. (Poster) D32. The 20th International Conference on High Resolution Molecular Spectroscopy, Prague (2008).

12) Oliviero, L., Leclerc, H., Manoilova, O.V., Blasin-Aube, V., Maugé, F., Kondratieva, E.V., Poretsky, M.S. & Tsyganenko, A.A.: Brønsted acidity of MgO induced by adsorption of acids. (Poster). 14th ICC Pre-Symposium, Kyoto (2008).

13) Oliviero, L., Leclerc, H., Manoilova, O.V., Blasin-Aube, V., Maugé, F., Kondratieva, E.V., Poretsky, M.S. & Tsyganenko, A.A.: Brønsted acidity created on MgO by H_2S adsorption. (Poster). Mexican Congress on Chemical Reaction Engineering (MCCRE 2008) Ixtapa-Zihuatanejo, (2008).

14) Rudakova, A. V., Sekushin, V. N., Marinov, I. L., Poretskiy, M. S. & Tsyganenko, A.A.: FTIR study of disperse ice and some processes on it. (Poster) 25. 8th Informal Conf. on Atmospheric and Molecular Science, Helsingor (2007).

15) Poretskiy, M. S. & Tsyganenko, A.A.: FTIR study of methane interaction with surface OH groups of oxide adsorbents. (Poster) 24. XVIIth Intern. conf.:"Horizons in Hydrogen Bond Research", St. Petersburg (2007).

16) Rudakova, A. V., Sekushin, V. N., Marinov, I. L., Poretskiy, M. S. & Tsyganenko, A.A.: FTIR study of processes on disperse ice surface. (Poster) 139. Int. Conf. Molecules in Space and Laboratory, Paris (2007).

Publications:

1) Poretskiy, M., Chichinin, A.I., Maul, C. & Gericke, K.-H. Simultaneous imaging of both product ions: Exploring gateway states for HCl as a benchmark molecule. PCCP 16: 19741-19746 (2014).

2) Rudakova, A. V., Poretskiy, M. S., Marinov, I. L. & Tsyganenko, A.A. IR spectroscopic study of surface properties of amorphous water ice. Optics and Spectroscopy (English translation of Optika i Spektroskopiya) 109: 708-718 (2010).

3) Maul, C., Poretskiy, M. & Rakhymzhan, A. N_2O van der Waals complex detection on Rydberg Transition in the ultraviolet. Journal of Molecular Spectroscopy 256: 80-85 (2009).

4) Oliviero, L., Leclerc, H., Manoilova, O.V., Blasin-Aube, V., Maugé, F., Kondratieva, E.V., Poretsky, M.S., Tsyganenko, A.A.: Brønsted acidity of MgO induced by H_2S adsorption. Industrial and Engineering Chemistry Research 48: 1237-1241 (2009).